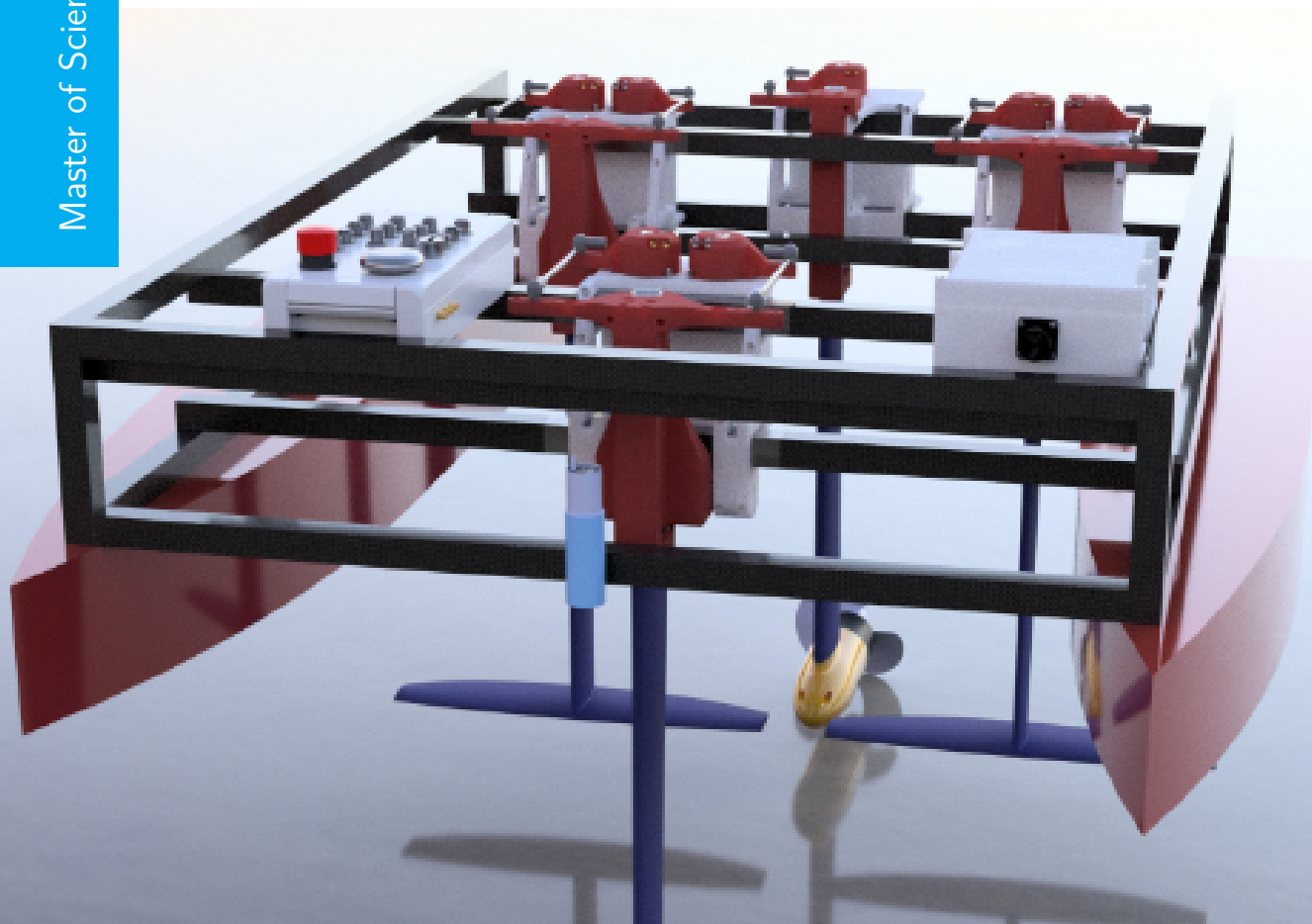


Modelling and Control of Experimental Scale Hydrofoil Craft

Theodoulos Kapnisis

Master of Science Thesis



Modelling and Control of Experimental Scale Hydrofoil Craft

MASTER OF SCIENCE THESIS

For the degree of Master of Science in Systems and Control at Delft
University of Technology

Theodoulos Kapnisis

September 28, 2022

Faculty of Mechanical, Maritime and Materials Engineering (3mE) · Delft University of
Technology



Copyright © Delft Center for Systems and Control (DCSC)
All rights reserved.



DELFT UNIVERSITY OF TECHNOLOGY
DEPARTMENT OF
DELFT CENTER FOR SYSTEMS AND CONTROL (DCSC)

The undersigned hereby certify that they have read and recommend to the Faculty of
Mechanical, Maritime and Materials Engineering (3mE) for acceptance a thesis
entitled

MODELLING AND CONTROL OF EXPERIMENTAL SCALE HYDROFOIL CRAFT

by

THEODOULOS KAPNISIS

in partial fulfillment of the requirements for the degree of
MASTER OF SCIENCE SYSTEMS AND CONTROL

Dated: September 28, 2022

Supervisor(s):

Dr. Dimitris Boskos

Dr. ir. Ido Akkerman

Dr. Omid Nejadseyfi

Reader(s):

Prof. dr. ir. Jan-Willem van Wingerden

Dr. S. Hassan HosseinNia

Abstract

Hydrofoil crafts with fully submerged foils can provide fast and economical waterway transport. However, their operation requires reliable onboard control systems to ensure the safety and comfort of their passengers, especially in rough sea conditions. This thesis project is focused on the dynamical modelling and the design of motion control systems for an experimental scale hydrofoil craft that is available at TU Delft, namely the Hydrofoil Education and Research Platform (HEARP).

The development of the dynamical model of HEARP is done by taking inspiration from the dynamics of marine crafts and aircraft and relying on different assumptions to obtain a simple and low-order model. The resulting model is a linearized state-space model with three degrees of freedom, namely heave, roll, and pitch, and includes the influence of regular waves. Because of inaccurate available data for the mass properties of HEARP, variations of the system parameters due to nonlinearities, and changes in the operating conditions, different uncertainties are assigned to most system parameters.

The use of multivariable feedback control methods for the motion control of hydrofoil crafts is limited, so this work is focused on exploiting such methods to improve the performance and robustness of such systems. The representation of the perturbed system using real parametric uncertainties is proved to be computationally expensive for the control design. Thus, the perturbed system is approximated by complex (dynamic) perturbations. A signal-based \mathcal{H}_∞ optimal controller is designed using the nominal system, and a μ -synthesis optimal robust controller is designed using the approximated perturbed system.

The performance and robustness of the proposed controllers are evaluated in both frequency and time domains through simulations. From the results, it is concluded that both controllers offer high-performance system responses for both reference tracking and disturbance rejection of incident waves. Furthermore, by comparing the two controllers, it is observed that the μ -synthesis controller shows superior robustness for the modelled uncertainty. In contrast, the \mathcal{H}_∞ controller has a slightly better performance when considering the perturbed systems with the real parametric uncertainty. The results of this thesis project can be used in the future to experimentally validate the accuracy of the proposed dynamical model and the performance of the designed controllers.

Table of Contents

Acknowledgements	xi
1 Introduction	1
1-1 General concept of hydrofoil craft	1
1-2 Hydrofoil Education and Research Platform	3
1-2-1 Electromechanical design of HEARP	3
1-2-2 Sensing & Control module	5
1-3 Literature Review	7
1-4 Selection of control design methodology	8
1-5 Thesis Objectives	9
1-6 Thesis Outline	10
2 Dynamic Modelling	11
2-1 Classifications of marine crafts	12
2-2 Motion Equations for Marine Crafts	13
2-3 Kinematics	14
2-3-1 Reference Frames	14
2-3-2 6 DOF Vectorial Notation	16
2-3-3 Euler Angle Transformation between BODY and NED	17
2-4 Rigid-Body Kinetics	17
2-5 Hydrostatics	19
2-6 Hydrodynamics	20
2-6-1 Hydrodynamic Added Mass and Coriolis–Centripetal Forces	20
2-6-2 Damping Forces	20
2-7 Waves	21
2-7-1 Linear wave theory	21
2-7-2 Wave Conditions	23

2-7-3	Encounter Angle and Encounter Frequency	23
2-8	Hydrofoil Lift and Drag Forces	25
2-8-1	Foil Geometry	25
2-8-2	Actuation mechanism	26
2-8-3	Modelling of hydrodynamic forces	28
2-8-4	Lift and Drag coefficients	32
2-8-5	Hydrodynamic Force and Moment vector	34
2-9	Motion Equations for HEARP	35
2-9-1	Assumptions	35
2-9-2	Reduced-order Nonlinear Dynamical Model with 3 DOF	36
3	Linear State-Space Model	39
3-1	Fundamental Properties of Linear Systems	39
3-2	Nonlinear State-Space Model	40
3-3	Derivation of the Linearized State-Space Model	41
3-3-1	Equilibrium Conditions	42
3-3-2	Equations of the Linearized Model	42
3-4	Wave disturbance model	43
3-5	Numerical values for system parameters	44
3-5-1	HEARP Mass Properties	44
3-5-2	Operating conditions of HEARP	45
3-5-3	Hydrofoils Parameters	46
3-5-4	Equilibrium Input	49
4	Control Design	51
4-1	Fundamental Properties of Control Systems	51
4-2	System Representation in the Frequency Domain	53
4-2-1	Poles and Zeros	54
4-2-2	Frequency Response	55
4-2-3	\mathcal{H}_∞ norm	56
4-2-4	Structured Singular Value	56
4-3	Feedback Control	57
4-3-1	Closed-loop Transfer Functions	57
4-3-2	Stability	58
4-3-3	Evaluating closed-loop performance	58
4-4	Signal-based \mathcal{H}_∞ Optimal Control Design	59
4-4-1	Configuration of the Generalized Plant	60
4-4-2	Weight Design	61
4-4-3	Controller synthesis	64
4-5	Characterization of Uncertainties	66

4-5-1	Introduction to Robustness	66
4-5-2	Representing Uncertainties	67
4-5-3	Approximating parametric uncertainty by complex perturbations	68
4-6	Optimal robust control design using μ -synthesis	74
4-6-1	Configuration of the Generalized Plant	74
4-6-2	Controller Synthesis	75
4-6-3	Controller Order-Reduction	78
4-7	Evaluation of Control Designs	79
4-7-1	Stability and Performance Evaluation	80
4-7-2	Comparison of designed controllers using different frequency responses	81
5	Simulation Results	87
5-1	Reference Tracking	87
5-2	Disturbance Rejection	90
6	Conclusions and Recommendations	95
6-1	Conclusions	95
6-2	Recommendations	96
A	Equations of the Linear State-Space Model	99
B	Transfer Function Matrices of the Control Design	103
	Bibliography	105
	Glossary	109
	List of Acronyms	109
	List of Symbols	110

List of Figures

1-1	(a) Diagram of a fully submerged hydrofoil system and (b) an example of a fully-submerged hydrofoil during foilborne operation [24]	2
1-2	Operation modes of a hydrofoil craft [24]	2
1-3	Actuators for variable lift force in hydrofoil crafts [35]	3
1-4	Platforming and contouring operation modes of a hydrofoil craft that foilborne [35]	3
1-5	Full assembly of HEARP [13]	4
1-6	(a) Foil & Strut module and (b) Rudder & Propulsion module	4
1-7	HEARP control architecture provided by Flying Fish	5
2-1	Motion in 6 DOF for a marine craft in body-fixed reference frame [14]	14
2-2	An overview of Reference Frames and the Body-fixed reference points [14]	15
2-3	Regular wave [32]	22
2-4	Frequencies and periods of the vertical motions of the ocean surface [21]	24
2-5	(a) Definition of encounter angle β [14] and (b) Encounter frequency and heading [32]	24
2-6	Foil Geometry [12]	26
2-7	Geometrical analysis of T-foil actuation mechanism [13].	27
2-8	Foil angle of attack vs Servo actuation angle [13]	27
2-9	Geometrical analysis for the determination of the location of CP of the hydrofoil	28
2-10	Free-body diagram of the hydrofoil	29
2-11	Change of inflow velocity due to different motions of the hydrofoil in the presence of incidence waves	31
2-12	Motion of a hydrofoil craft in calm water	32
2-13	Foil lift curves [12]	33
2-14	Linear approximations for the lift and drag coefficients [5]	34

3-1	Location of the origin of CAD model and the CG of system [13]	45
3-2	Lift and drag coefficients as a function of angle of attack based on experimental data from Ship Hydromechanics Group of TU Delft	47
3-3	Error of linear approximation for drag coefficient C_D as function of effective angle of attack α_e	47
3-4	Lift reduction factor versus submergence depth to chord ratio for different AR [8]	48
4-1	Open-loop block diagram of the HEARP system	54
4-2	Block diagram of a negative feedback control system [44]	57
4-3	Block diagram of signal-based \mathcal{H}_∞ optimal control problem for the nominal plant	61
4-4	General control configuration for the case with no model uncertainty [44]	65
4-5	Plant with multiplicative uncertainty [44]	68
4-6	Frequency responses of the relative error between the nominal and the perturbed systems for each channel of G	70
4-7	Frequency responses of the relative error between the nominal and the perturbed systems for each channel of G_d	71
4-8	Frequency response of the relative error between the nominal and the perturbed systems for g_{sm}^i	71
4-9	Singular value plots of the perturbed systems with the real parametric uncertainty and the approximated perturbed systems with the multiplicative input uncertainty	73
4-10	Block diagram of signal-based μ -synthesis optimal control problem for the perturbed plant	74
4-11	General control configuration for the case that includes model uncertainty [44]	76
4-12	(a) Hankel singular values of the balanced realization of the μ -synthesis controller \hat{K}_{bal} and (b) Singular values of the approximation error of the reduced-order controller	80
4-13	NP, RS and RP conditions as a function of frequency for the designed controllers	82
4-14	Singular values of sensitivity S and the inverse of the performance weight W_P for (a) perturbed systems with real parametric uncertainties and (b) approximated perturbed systems with multiplicative input uncertainties	83
4-15	Singular values of complementary sensitivity T	84
4-16	Singular values of SG_d (contribution of disturbance to the error signal)	84
4-17	Singular values of (a) KS and (b) KSG_d and the inverse of the control input weight W_u	85
4-18	Controller Singular Value Plot	86
5-1	System responses for reference tracking	88
5-2	Control signals for reference tracking	89
5-3	Comparison of system responses for reference tracking with the parametric and multiplicative uncertainties for (a) μ -synthesis controller and (b) \mathcal{H}_∞ controller	90
5-4	System responses for disturbance rejection.	92
5-5	Control signals for reference tracking	92
5-6	RMS of the error signals for varying wave frequency and with $\zeta_0 = 0.06$ m.	93
5-7	RMS of the error signals for varying wave amplitude and with $\omega = 4.53$ rad/s	94

List of Tables

1-1	Technical Specifications of HEARP [13]	6
1-2	Control architectures for hydrofoil crafts which are found in the literature	7
2-1	The notation of Society of Naval Architects and Marine Engineers (SNAME) for marine vessels [14]	13
2-2	Classification of motions	19
3-1	Equilibrium position of the CP for each hydrofoil expressed in NED frame	44
3-2	Estimation of mass properties of HEARP from 360 Fusion	45
3-3	Steady-state conditions for the foilborne operation of HEARP and environmental conditions	46
3-4	Design specifications of hydrofoils	46
3-5	Parameters that are related to hydrodynamic forces	49
4-1	Poles and transmission zeros of the transfer function matrices $G(s)$ and $G_d(s)$	55
4-2	Maximum and minimum of absolute values for the encounter frequencies of head and following waves	64
4-3	Characteristics of the signal-based \mathcal{H}_∞ optimal controller	66
4-4	Characteristics of the μ -synthesis optimal robust controller	77
4-5	Stability and performance characteristics of the designed controllers	81

Acknowledgements

Graduating with an MSc in Systems and Control at TU Delft is definitely one of the most challenging experiences that I have ever had in my whole life so far. During this long and difficult journey of reaching the final step of my thesis, I have been taught an important lesson: that hard work pays off if you are patient enough to see it through. It is a fact that I have invested a significant amount of time in studying to reach satisfactory and correct results, obviously after making numerous mistakes. Nevertheless, I am grateful that through this experience, I have expanded my knowledge and have developed skills that will be incredibly useful in my professional career and life.

Of course, I would never have succeeded in reaching this step of graduation without the support and assistance I received along the way. Firstly, I would like to express my sincere gratitude to my primary supervisor Dr. Dimitris Boskos for his continuous assistance, guidance and patience during the writing of my thesis. Subsequently, I wish to thank Dr. Omid Nejadseyfi for his guidance and cooperation in the effort to implement the control system in the experimental setup of HEARP. Furthermore, I also thank Dr. ir. Ido Akkerman and Dr. Alex Ashworth-Briggs for their assistance, especially for the more technical aspects of the project, including the hardware and the software of HEARP.

Finally, I would like to express my deepest gratitude to my parents for their constant financial and emotional support during my studies and for allowing me to pursue my dreams and ambitions. In addition, I was fortunate to have many friends, colleagues and teammates around me during this difficult period of my academic career because each of them, in their own way, helped me achieve my goals. Hence, I would like to thank them all.

Delft, University of Technology
September 28, 2022

Theodoulos Kapnisis

Chapter 1

Introduction

A trustworthy and cost-efficient solution for high-speed waterway transportation is the hydrofoil craft. Nevertheless, it requires sophisticated onboard control systems to ensure comfortability of the passengers, safety and reliability during its operation, especially in severe sea conditions. Such control systems must accurately estimate all the hydrofoil states (positions and velocities) and the stochastic wave environment, and perform quick manoeuvring.

To unlock new insights into the dynamic behaviour of hydrofoil crafts, the Ship Hydromechanics Group (Maritime & Transport Technology) developed the Hydrofoil Education and Research Platform (HEARP), in collaboration with the FlyingFish company. HEARP is a modular craft with a scaled size that can fit different foil configurations and test various control strategies. The initial design of HEARP with a control system in a baseline configuration, was made for Delft University of Technology (TU Delft) by Flying Fish. This configuration is a stable initial set-up and it can be used for educational and research projects.

The general goal of this thesis project is to study all the topics considered relevant for developing a dynamical model and the design of an integrated control system for a hydrofoil craft, such as HEARP. This chapter briefly introduces the fundamental principles of hydrofoil crafts.

1-1 General concept of hydrofoil craft

The fundamental principle of the hydrofoil craft concept is to lift the hull of a ship out of the water and dynamically support it on wing-like lifting surfaces, i.e., hydrofoils [35] (see Figure 1-1). The reduction of submerged surface leads to a significant reduction of water resistance (drag) and a notable decoupling from wave disturbance, consequently improving sea-keeping quality [49]. Subsequently, this leads to a considerable reduction of the power required to attain high speeds.

A hydrofoil craft has submerged hydrofoils mounted on struts on the bottom of its hull. It generates lift force in the same principle as an aircraft wing and lifts the vessel's hull out of

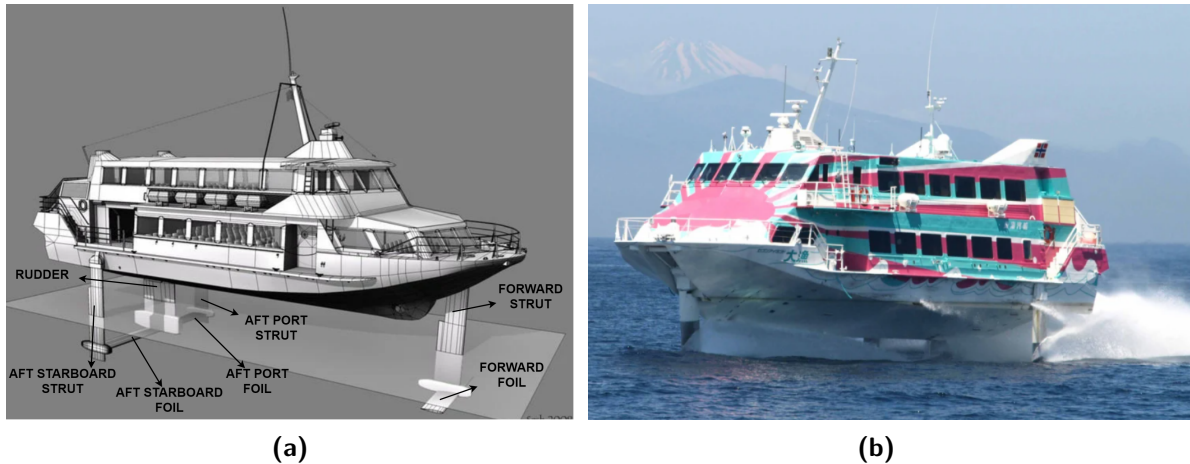


Figure 1-1: (a) Diagram of a fully submerged hydrofoil system and (b) an example of a fully-submerged hydrofoil during foilborne operation [24]

the water, as shown in Figure 1-1b. Nevertheless, since water density is substantially higher than air (about 800 times higher), the size of hydrofoils is much smaller than aircraft wings [49].

The operation of the hydrofoils vessels is mainly divided into 2 separate modes [12] (see Figure 1-2) :

- Hullborne when the vessel is fully supported by its hull (buoyancy forces) like conventional ships.
- Foilborne after the take-off, the vessel is fully supported by its hydrofoils (lift forces).



Figure 1-2: Operation modes of a hydrofoil craft [24]

The hydrofoils of the fully-submerged system are designed to operate continuously under the water surface, and they commonly have an inverted T-shape. In this configuration, the hydrofoil system is not self-stabilizing. Thus, the effective angle of attack of the hydrofoils or part of them should vary to control the lifting force in response to changing ship speed, weight and sea conditions. Hydrofoil variable lift force can be obtained by either trailing edge flaps or variable incidence of the entire foil as illustrated in Figure 1-3. It is worth noting that the motion of a fully-submerged hydrofoil craft is decoupled significantly from the effect of waves. Hence, a relatively small fully-submerged hydrofoil craft can operate foilborne at high speed in open sea conditions while maintaining a comfortable motion environment for the crew and passengers [35].

A hydrofoil craft that is foilborne may operate in two different modes, namely platforming and



Figure 1-3: Actuators for variable lift force in hydrofoil crafts [35]

contouring, as illustrated by Figure 1-4. The platforming mode is generally used in waves with high frequency and relatively small amplitude and aims to minimize vertical accelerations. However, the operation of this mode is limited by the wave amplitude and the strut length. Thus, the control system has to switch to contouring mode when the craft can no longer operate in platform mode. This aims to minimize relative vertical motion between the craft and the waves by keeping the distance from the water surface constant and ensuring the avoidance of ventilation and broaching of the foils [12], [35].

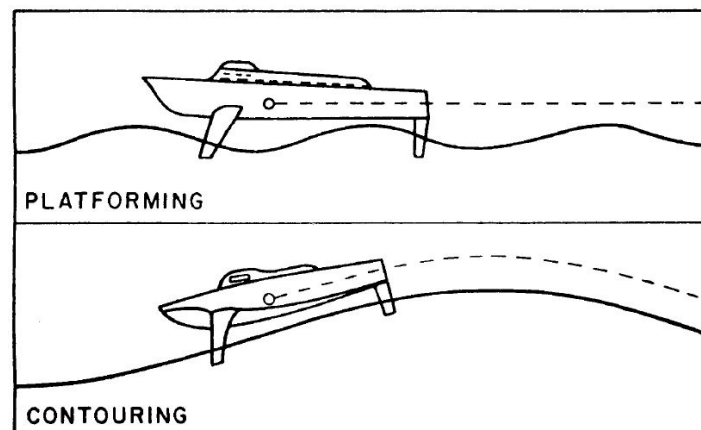


Figure 1-4: Platforming and contouring operation modes of a hydrofoil craft that foilborne [35]

1-2 Hydrofoil Education and Research Platform

In this section, the major characteristics of the HEARP system are presented. The content of this section is written by taking inspiration from the provided documentation by Flying Fish [13]. HEARP is a fully-submerged hydrofoil craft that is remotely controllable and self-propelled, designed for sailing on outside water (lake, canal) and in the towing tank facility at the TU Delft. An illustration of the HEARP is given by Figure 1-5.

1-2-1 Electromechanical design of HEARP

HEARP is kept afloat by two identical hulls placed on each side of the craft symmetrically. This design is known in the marine industry as a catamaran. Its base is constructed out of carbon fibre square tubing and has an open frame structure.

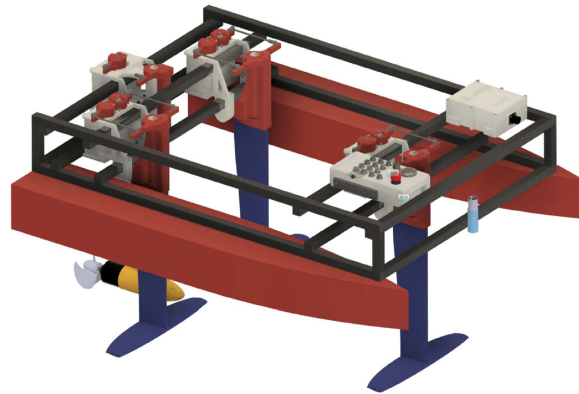


Figure 1-5: Full assembly of HEARP [13]

The baseline configuration of HEARP includes three identical T-foils, one attached at the bow side of the craft and two near the stern (canard configuration). The T-foils combine foil pitch actuation with the functionality of yawing the strut. This actuation is achieved by utilising two servo motors (red arrows in Figure 1-6a) and associated motor controllers, which are placed in an enclosure box. Asymmetric deflection of the servo motors controls the pitch of the hydrofoil, while an asymmetric deflection of the servo motors controls the yaw. However, for simplicity, only the symmetric deflection of the servo motors is considered in this study. Thus the investigation of the potential to use the asymmetric deflection for controlling HEARP motions is left for future studies. This module is shown in Figure 1-6a.

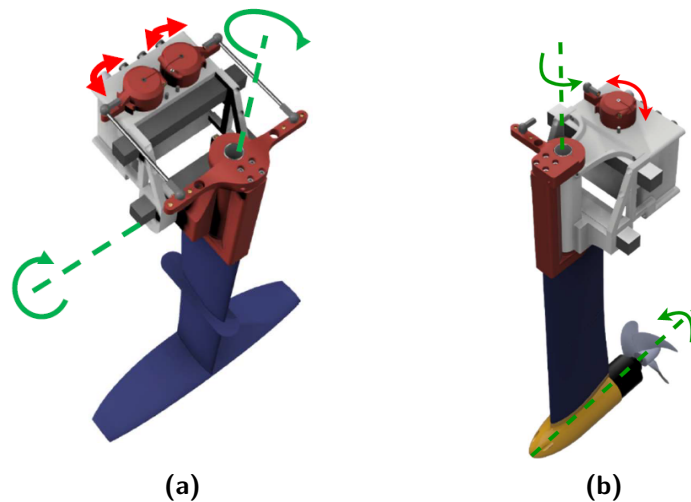


Figure 1-6: (a) Foil & Strut module and (b) Rudder & Propulsion module

In the HEARP baseline configuration, thrust is generated by an electric podded propeller mounted at the tip of the rudder surface. The rudder surface can deflect, allowing a varying lift vector used to control the boat around its yaw axis. The actuation of the rudder surface is done by a single servo motor (red arrow in Figure 1-6b), whose arm and the translating foil arm are connected by an actuation rod. The servo motor and associated motor controller are placed in an enclosure box. This module is shown in Figure 1-6b.

1-2-2 Sensing & Control module

HEARP is a semi-autonomous vehicle, which means that the operator has control over several degrees of freedom (DOF) while the control system automatically controls others. An overview of the initial setup of HEARP control architecture provided by Flying Fish is presented by Figure 1-7. Firstly, the operator via remote control, generates the setpoints for the throttle of the podded propeller and the yaw deflection of the rudder in a feed-forward scheme. Next, these setpoints are transformed into pulse-width modulation (PWM) signals, which are used as inputs to an electronic speed controller (ESC), a commercial method to regulate the motion of DC motors.

A feedback control scheme is used to regulate the motion of the three hydrofoils. Fixed setpoints for the heave, roll and pitch motions are used as external reference signals to the system. The closed-loop system includes three single-input single-output (SISO) Proportional-Integral-Derivative (PID) controllers (height, pitch, roll) that are designed by a trial and error procedure because there is no mathematical model available. The input of these controllers is the error signal between the reference signals and the current state of the system, while their the output are the commanded angles of the servo motors. These outputs are transformed to PWM signals which are used as inputs to ESC that are responsible for regulating the motion of the servo motors.

Finally, after applying the action of actuators to the system, the raw measurements of different sensors are used as inputs to an observer (state estimator). The PX4 software, through the Estimation and Control Library (ECL), uses an Extended Kalman Filter (EKF) algorithm to process sensor measurements and estimate the state of the system. Then these states are fed back to the loop to calculate the error signal. Like all estimators, most performance comes from tuning to match sensor characteristics, such as biases and noise variances. However, it is a fact that the tuning is a compromise between accuracy and robustness. Therefore, depending on the application, different tuning changes are required [41].

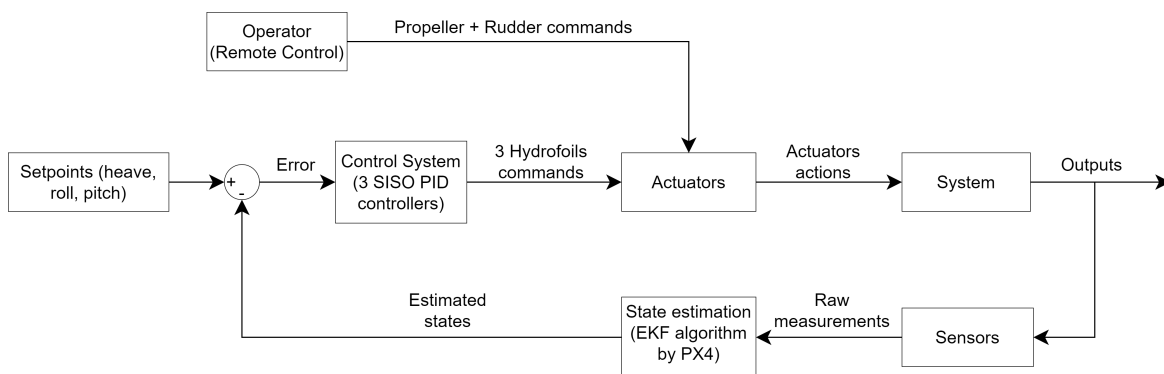


Figure 1-7: HEARP control architecture provided by Flying Fish

The following sensors are used for measuring the appropriate variables for the generation of a filtered state of HEARP:

- Inertial measurement unit (IMU) + magnetometer used for attitude determination
 - $\dot{p}, \dot{q}, \dot{r}, \ddot{x}, \ddot{y}, \ddot{z}$ (linear & angular accelerations)
 - Gravity reference vector

- Heading (magnetic compass)
- Global positioning system (GPS) used for position determination
 - x, y, z (inertial position)
- Ultrasonic height sensor used for ride height determination
 - h (ride height)

Software and Control Algorithm

The software framework for the entire control system is based on PX4 software. It is an open-source autopilot software used for unmanned vehicles, including helicopters, quad-copters, fixed-wing aircraft and submarines. This software platform offers a lot of useful tools and a modular architecture with the flexibility to implement custom functions that can be fitted to any application. A Pixhawk 4 onboard computer is used to run the PX4 software. Pixhawk 4 is a commercially available flight computer designed to run the PX4 software. The Pixhawk 4 has been selected because of the standardised inputs-outputs, and its compatibility with a large variety of sensors, actuators, protocols and ground-control software. Pixhawk runs different codes that transform sensor data and setpoints into control commands [41].

The key technical specifications of the delivered baseline configuration by Flying Fish, based on the final design and final experimental tests are summarized in Table 1-1.

Table 1-1: Technical Specifications of HEARP [13]

Description	Value
Length	1.5 m
Width	1.0m
Height	0.8m
Take-off cruise speed	≈ 3 m/s
Cruise speed during stable flight	3.5-6 m/s
Maximum cruise speed with stable flight	6 m/s
Nominal submergence of hydrofoils	≈ 0.2 m

Concluding, this section presents the essential aspects of HEARP, aiming to give a brief overview of the whole system, and investigate which topics are most crucial for the further development of the system. After different tests with the current setup of the control system delivered by Flying Fish, it is observed that the response of the system is very sensitive to the control skills of the operator and the wave disturbances. Therefore, it is deduced that the poor performance perhaps originates from the absence of incorporation of an accurate mathematical model in the control design procedure. Using a mathematical model, one would design a more advanced control architecture. Consequently, the literature review focused on the dynamic modelling of the system and the algorithms/methods used for the control design for hydrofoil crafts. A summary of the findings of the literature review is presented in the next section.

1-3 Literature Review

The literature review is devoted to understanding the dynamics and design of control systems for hydrofoil crafts, such as the HEARP, by examining various published articles and books. More precisely, it includes three main topics: the dynamical modelling of hydrofoil crafts, the motion control systems for hydrofoils crafts and an introduction to the selected control design methodology. The main findings in the literature for the first two topics are introduced briefly in this section, while the last topic is covered later in more detail in Chapter 4.

Considerable research has been done regarding hydrofoil modelling and control by considering different dynamical models. An overview of the research done so far regarding the control of hydrofoil crafts is given in Table 1-2, where the main characteristics of each study are reported.

Table 1-2: Control architectures for hydrofoil crafts which are found in the literature

Article	L/NL ¹	DOF	Obj ²	Control methods	E ³	W ⁴
Lee et al., 2002 [28]	L	2 DOF(z, θ)	D-R ⁵	LQR ⁶	✓	✓
Kim et al., 2004 [27]	L	2 DOF(z, θ)	D-R	LQR	✓	✓
Kim et al., 2004 [26]	L	2 DOF(z, θ)	T-T ⁷	Preview Control	×	✓
Ren et al., 2004 [42]	L	2 DOF(z, θ)	D-R	Fuzzy Control	×	✓
Cruz et al., 2004 [9]	L	2 DOF(z, θ)	D-R	PID ⁸	✓	✓
Hatzakis et al., 2006 [20]	L	2 DOF(z, θ)	D-R	LQR	×	✓
Bai et al., 2010 [4]	L	2 DOF(z, θ)	D-R	PID, LQR, SMC ⁹	×	✓
Kim et al., 2011 [25]	L	2 DOF(ϕ, θ)	D-R	PID, LQG ¹⁰	✓	✓
Wang et al., 2014 [48]	NL	3 DOF(y, ϕ, ψ)	T-T	Lyapunov, Fuzzy	×	×
Hassani et al., 2014 [18]	L	3 DOF(z, ϕ, θ)	D-R	\mathcal{H}_2 Control	✓	✓
Liu et al., 2016 [30]	NL	2 DOF(ϕ, ψ)	T-T	SMC with EDO ¹¹	×	✓
Liu et al., 2017 [31]	NL	4 DOF(x, y, ϕ, ψ)	P-F ¹²	HRCS ¹³	×	✓
Piene, 2018 [40]	L	3 DOF(z, ϕ, θ)	D-R	\mathcal{H}_2 Control	×	✓
Liu et al., 2019 [29]	NL	2 DOF(z, θ)	D-R	SMC with DO ¹⁴	×	✓
Bencatel et al., 2021 [6]	L	3 DOF(x, z, θ)	D-R	LQR	✓	✓

¹Linear or nonlinear dynamical model respectively

²Objective of the control system

³Denotes if the study includes experimental results

⁴Denotes if the excitation forces due to incident waves are included in the model

⁵Disturbance Rejection

⁶Linear Quadratic Regulator

⁷Trajectory Tracking

⁸Proportional Integral Derivative

⁹Sliding Mode Control

¹⁰Linear Quadratic Gaussian

¹¹Extended Disturbance Observer

¹²Path Following

¹³Hierarchical Robust Control Strategy

¹⁴Disturbance Observer

Based on the findings in the literature, it is deduced that researchers have shown a significant

interest in the topic of modelling and control of hydrofoil crafts over the past two decades. From the results of Table 1-2, it is seen that all studies were focused on reduced-order models, so none of the articles had studied the control design for a hydrofoil craft in 6 DOF. This choice can lead to a simpler control design. However, it is only possible when the coupling between different motions of the system is negligible. Hence, it is concluded that the dynamics of hydrofoils indeed can be decoupled to some extent, as the majority of the researchers were focused on designing controllers for reduced-order models. It is worth noting that while older studies relied on linear dynamical models and control methods, the most recent ones include nonlinear control strategies.

In addition, it is observed that the control of the longitudinal dynamics (x, z, θ) with disturbance rejection of the incident wave excitation forces attracted the interest of the researchers significantly, especially for studies before 2010. Nevertheless, it is deduced that in the last decade, the research shifted its focus on the control of lateral dynamics (y, ϕ, ψ) or even a combination of longitudinal and lateral dynamics, which are more complex and challenging from the perspective of control design. An important observation is that the greater number of the articles include the excitation forces of the incident waves. Furthermore, the experimental validation of the proposed controllers was found in almost half of the articles. Thus, it is concluded that the experiments are crucial for evaluating a proposed control system for hydrofoil crafts.

Considering all the above, this study focuses on developing a reduced-order model for HEARP and designing a control system for this model. This decision is made by taking into account the size of the problem and complexity, but also because various researchers followed a similar approach. More precisely, the modelling includes the motions that are regulated by the three hydrofoils, namely the heave (z), roll (ϕ) and pitch (θ) motions. More details about the developed dynamical model for the HEARP system are presented in Chapter 2.

1-4 Selection of control design methodology

From the findings in the literature (see Table 1-2), it is concluded that the majority of the researchers were focused on state-space methods for the design of controllers and, more precisely, the use of optimal control theory. Various researchers observed that different physical phenomena affect the accuracy of the dynamical models of hydrofoil crafts. Thus, some of these observations are summarized below:

- The hydrodynamic coefficients of a hydrofoil craft operating in irregular sea waves are frequency-dependent [28].
- When a hydrofoil craft operates in waves, there exists a significant variation of the lift forces of the hydrofoils due to the orbital motion of the waves, which is extremely difficult to model in irregular waves with random frequencies and encounter angles [26].
- Hydrodynamic memory effects should be considered in the dynamics of the system, which may be treated as a small-amplitude disturbance [20].
- The existence of free surface phenomena causes a variation in the lift coefficients of the hydrofoils [4]. Additionally, possible variations of lift coefficients due to the influence on the aft hydrofoils by the trailing vortices of the fore hydrofoils [34], are not taken into account in any article.

- In the study of [4] it was proven that the simulation results differ from experimental results due to the neglecting of complex phenomena of waves such as diffraction forces, viscous effects, and non-linear effects.

Hence, it is concluded that it is quite challenging to describe accurately the complex and highly non-linear dynamics of a hydrofoil craft sailing in foilborne mode. This is because there exist variations of system coefficients due to nonlinearities and changes in the operating conditions (cruise speed and orbital waves). Additionally, neglected and unmodelled dynamics (simplified models are usually used) may deteriorate the accuracy of the dynamical model.

It is a fact that these issues may be treated efficiently using multivariable feedback control methods. These methods can take into account parametric and dynamic uncertainties, as well as neglected and unmodelled dynamics, to design controllers that can ensure robust performance and stability. Based on the findings in the literature, one can deduce the absence of extensive research on the use of multivariable feedback control methods for the motion control of hydrofoil crafts. Hence, this thesis project is focused on the potential of using these methods aiming to improve the performance and robustness of the control systems for hydrofoil crafts.

1-5 Thesis Objectives

The initial objective of this thesis project was to include the experimental validation of the proposed control design through experiments with HEARP in the towing tank. To achieve this goal, it was necessary to configure the hardware and the software of the experimental setup of the HEARP system. The procedure to perform the desired experiments includes the following steps:

1. Get familiar with the hardware and software.
2. Calibration the sensors and the actuators.
3. Development of the necessary software for implementing the designed control systems using PX4 codes.
4. Test the developed software for the control system of HEARP inside the towing tank through straight foilborne flights and modify it if needed.
5. Tune the designed controllers iteratively through different experiments.
6. Validate the performance of the proposed control designs via experiments using different reference signals and waves with different characteristics.

A considerable amount of time was spent to complete all the steps mentioned above. Nevertheless, it was not possible mainly because of various technical problems with the electrical and mechanical parts of HEARP and some difficulties in implementing the designed control systems using PX4 codes. Within the available time, we were able to reach up to step 4 with testing the developed software. So the proposed controllers presented in this study were designed and tuned using only simulation results. By taking into consideration all the above, the main objectives of the thesis project are finally defined as:

Development of a dynamical model for an experimental scale hydrofoil craft with 3 DOF (heave, roll and pitch motions) that operates in the presence of regular waves and control system design using multivariable feedback control theory.

1-6 Thesis Outline

The structure of the thesis project is such that it methodically introduces to the reader all the relevant theories and results essential to accomplish the aforementioned main objectives. Therefore, the process of reaching this goal is divided into sub-problems covered by the different chapters of this report. The thesis project is organized as follows:

Chapter 2: Development of a reduced-order nonlinear dynamical model in 3 DOF (heave, roll and pitch motions) for a hydrofoil craft that includes three identical T-foils and the influence of the incident regular waves.

Chapter 3: Linearization of the nonlinear dynamical model about the expected cruise conditions of the hydrofoil craft and defining the nominal values and the uncertainties of all the parameters of the system.

Chapter 4: Design of a \mathcal{H}_∞ optimal controller and a μ -synthesis robust optimal controller. The design of the controllers includes the selection of the appropriate weighting transfer functions for the specifications of the control system, and the approximation of the parametric uncertainties of the system by dynamic uncertainties. The robustness and the performance of the designed controllers are evaluated using different frequency responses.

Chapter 5: Simulation results for the validation of the performance of the proposed control designs, considering the reference tracking and disturbance rejection problems.

Chapter 6: Makes conclusions and proposing some recommendations that can be used as an inspiration for future research.

It is essential to mention that the length of this report is justified by the need to cover the fundamental theory from both the maritime/mechanical engineering and the control engineering perspectives.

Chapter 2

Dynamic Modelling

This chapter presents all the relevant topics needed to derive a nonlinear dynamical model for the HEARP system. Dynamical models may be obtained from physical modelling, analyzing input-output data (system identification) or combining these two approaches [44]. The primary goal of Chapter 2 is to develop a reduced-order nonlinear dynamical model in 3 DOF (heave, roll and pitch) for the HEARP system using physical modelling. Firstly, we introduce the relevant topics for deriving the dynamical model for a hydrofoil craft. The greatest portion of these topics is obtained from marine craft hydrodynamics that are found in [14] [15]. Subsequently, we derive the reduced-order nonlinear dynamical model in 3 DOF using all the associated assumptions.

Flying Fish has delivered a baseline configuration of the control system of HEARP, with which the propulsion system and steering are controlled via remote control. After various experiments, it is concluded that it cannot provide repetitive responses because the results depend on the control skills of the operator. Hence, the necessity to design automatic control algorithms for the propulsion system (propeller) and the steering (rudder) is identified here. These controllers will be responsible for tracking a specific path with constant cruise speed (such as a straight line for tests in the towing tank). As an initial simple solution, these two individual control algorithms can be designed using feedback PID controllers, which will attempt to regulate the cruise speed and the yaw of the HEARP. Assuming that these SISO controllers for the propeller and the rudder can achieve high-performance reference tracking, the sway motion can also be regulated to zero indirectly because the hydrofoil craft will foilborne in a straight line.

However, as aforementioned, this study is focused only on the modelling and control design of a reduced-order model of HEARP in 3DOF (heave, roll and pitch). Therefore the modelling of the surge, sway and yaw motions and the designing of controllers for the propeller and rudder are left for future studies. The objectives of the control design (see Chapter 4) are the reference tracking and the disturbance rejection for the reduced-order model using multivariable feedback controllers.

2-1 Classifications of marine crafts

The term marine craft can include ships, high-speed craft, semi-submersibles, submarines and remotely operated underwater vehicles. From a hydrodynamic point of view, one can classify marine crafts according to their maximum operating speed [14]. For this purpose, it is common to use the Froude number:

$$F_n = \frac{U}{\sqrt{gL}}$$

where U is the craft speed, L is the overall submerged length of the craft, and g is the acceleration of gravity.

The pressure that carries the craft can be divided into hydrostatic and hydrodynamic pressure, with their corresponding forces summarised below:

- Buoyancy force due to the hydrostatic pressure, which is proportional to the displacement of the ship.
- Hydrodynamic force due to the hydrodynamic pressure, which is approximately proportional to the square of the relative speed of the water.

Depending on the Froude number of a marine craft sailing at constant cruise speed U , the following rough classifications can be made:

- **Displacement Vessels ($F_n < 0.4$):** The buoyancy force (restoring terms) dominates relative to the hydrodynamic forces (added mass and damping).
- **Semi-displacement Vessel ($0.4 - 0.5 < F_n < 1.0 - 1.2$):** The buoyancy force is not dominant at the maximum operating speed for a high-speed submerged hull-supported vessel.
- **Planing Vessel ($F_n > 1.0 - 1.2$):** The hydrodynamic forces mainly carries the weight, thus the lift and drag forces are dominant.

In our case, a catamaran craft with fully-submerged hydrofoils (like HEARP) during hullborne may be considered a displacement ship due to the low speed and the high overall submerged length. However, after take-off, during foilborne, the hydrodynamic forces mainly carry the weight, while the buoyancy force (restoring terms) is negligible. Therefore, in this case, the dominant hydrodynamic lift and drag forces must be considered.

The equations of motion (EOM) for this system are hybrid because they should incorporate the principal operation modes of the hydrofoil craft, namely the hullborne and the foilborne (see Figure 1-2). One may consider additional operation modes of the craft during take-off and landing, so the EOM that describe the craft's motion can be a combination of hullborne and foilborne modes. The incorporation of the dynamic behaviour of the system for these operation modes during the control design is crucial to ensure a safe and smooth transition between the two principal operation modes. Nevertheless, in this study, the focus is limited to the derivation of EOM for the foilborne mode, which is the primary operating mode of a hydrofoil craft.

The EOM of the system with 6 DOF when the craft is hullborne can be obtained from [14], which can describe the dynamic behaviour of the system very accurately, as the craft is considered as a displacement vessel. Nonetheless, for the case of foilborne mode, the EOM presented in [14], has to be appropriately modified to include the hydrodynamic forces of lift and drag

forces, which originated from the variable incidence T-foils. To do so, some inspiration is taken from the aircraft dynamics for modelling these forces, as they are comparable to some extent with the dynamics of a hydrofoil craft.

2-2 Motion Equations for Marine Crafts

For a marine craft, the DOF are the independent displacements and rotations that completely specify the displaced position and orientation of the craft. A craft that can move freely in 3-D space has a maximum of 6 DOF. The first three coordinates and their time derivatives correspond to the position and translational motion along the x , y and z axes. On the other hand, the last three coordinates and their time derivatives describe orientation and rotational motion. The six different motion coordinates of a marine craft are defined as surge, sway, heave, roll (heel), pitch (trim) and yaw (see Table 2-1 and Figure 2-1). In Table 2-1, the subscripts b and n denotes the BODY and NED reference frames respectively, which are introduced later in Section 2-3 [14].

Table 2-1: The notation of Society of Naval Architects and Marine Engineers (SNAME) for marine vessels [14]

BODY				NED
DOF		Forces and moments	Linear and angular velocities	Positions and Euler angles
1	Motions in the x_b -direction (surge)	X	u	x_n
2	Motions in the y_b -direction (sway)	Y	v	y_n
3	Motions in the z_b -direction (heave)	Z	w	z_n
4	Rotation about the x_b axis (roll)	K	p	ϕ
5	Rotation about the y_b axis (pitch)	M	q	θ
6	Rotation about the z_b axis (yaw)	N	r	ψ

The 6 DOF EOM for a hydrofoil craft can be derived by taking inspiration from the general 6 DOF EOM for marine crafts, which are written in a vectorial setting as follows:

$$\underbrace{M_{RB}\dot{\nu} + C_{RB}(\nu)\nu}_{\text{rigid-body forces}} + \underbrace{M_A\dot{\nu} + C_A(\nu)\nu + D(\nu)\nu}_{\text{hydrodynamic forces}} + \underbrace{g(\eta)}_{\text{hydrostatic forces}} = \underbrace{\tau_c}_{\text{control inputs}} + \underbrace{\tau_{wave}}_{\text{disturbances}} \quad (2-1)$$

where ν and η are the generalized velocities and positions used to describe motions in 6 DOF [14]. Note that the system states η and ν are a function of time; however, to simplify notation, the (t) is usually omitted. The definitions of all the components in Eq. (2-1) are summarized below by:

- $\eta = [x_n, y_n, z_n, \phi, \theta, \psi]^T$: Positions and angles expressed in NED reference frame
- $\nu = [u, v, w, p, q, r]^T$: Linear and angular velocities expressed in BODY reference frame
- M_{RB} : Rigid-body inertia matrix
- $C_{RB}(\nu)$: Rigid-body Coriolis-centripetal matrix
- M_A : Hydrodynamic added mass matrix
- $C_A(\nu)$: Hydrodynamic Coriolis-centripetal matrix
- $D(\nu)$: Damping matrix

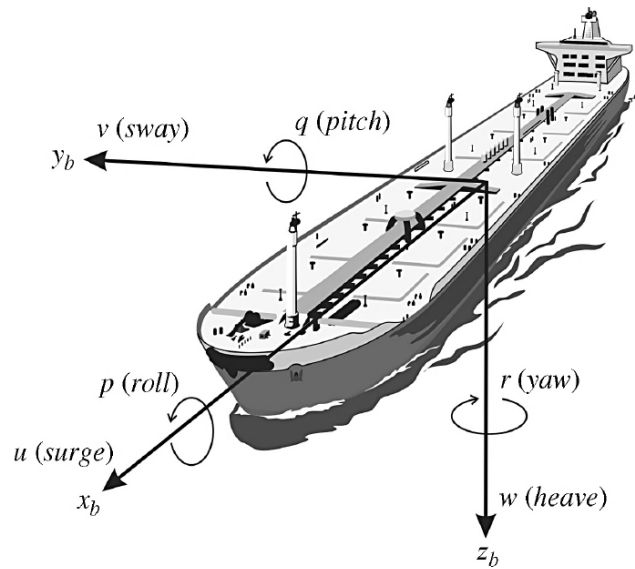


Figure 2-1: Motion in 6 DOF for a marine craft in body-fixed reference frame [14]

- $g(\eta)$: Gravitational/buoyancy forces and moments
- τ_c : Control inputs
- τ_{wave} : Wave-induced forces (disturbances)

2-3 Kinematics

The study of dynamics of a marine craft is divided into two parts: Kinematics (Section 2-3), which comprises only geometrical aspects of motion, and Rigid-Body Kinetics (see Section 2-4), which is the analysis of the forces and moments causing the motion [14].

2-3-1 Reference Frames

For the analysis of the motion of a marine craft in 6 DOF, it is convenient to define Earth-centered coordinate frames, Geographic reference frames and Body-fixed frames, as indicated in Figure 2-2.

Earth-Centered Reference Frames

Earth-centered reference frames consist of the Earth-centered inertial (ECI) and the Earth-centered Earth-fixed (ECEF) reference frames. The ECI frame $\{i\} = (x_i, y_i, z_i)$ is a non-accelerating reference frame in which Newton's laws of motion apply, and it is considered an inertial frame. The origin of $\{i\}$ is located at the centre o_i of the Earth. Similarly, the ECEF frame $\{e\} = (x_e, y_e, z_e)$ also has its origin o_e fixed to the centre of Earth; however, the axes rotate relative to the inertial frame ECI, which is fixed in space. The Earth rotation can be neglected for marine craft moving at relatively low cruise speed; thus, $\{e\}$ is considered

inertial. These frames are usually used for global guidance, navigation and control, for instance, to describe the motion and location of ships in transit between different continents. Nevertheless, since we are interested in marine craft operating in a local area, we focus on the two most essential reference frames, namely the BODY and the NED, which are introduced next.

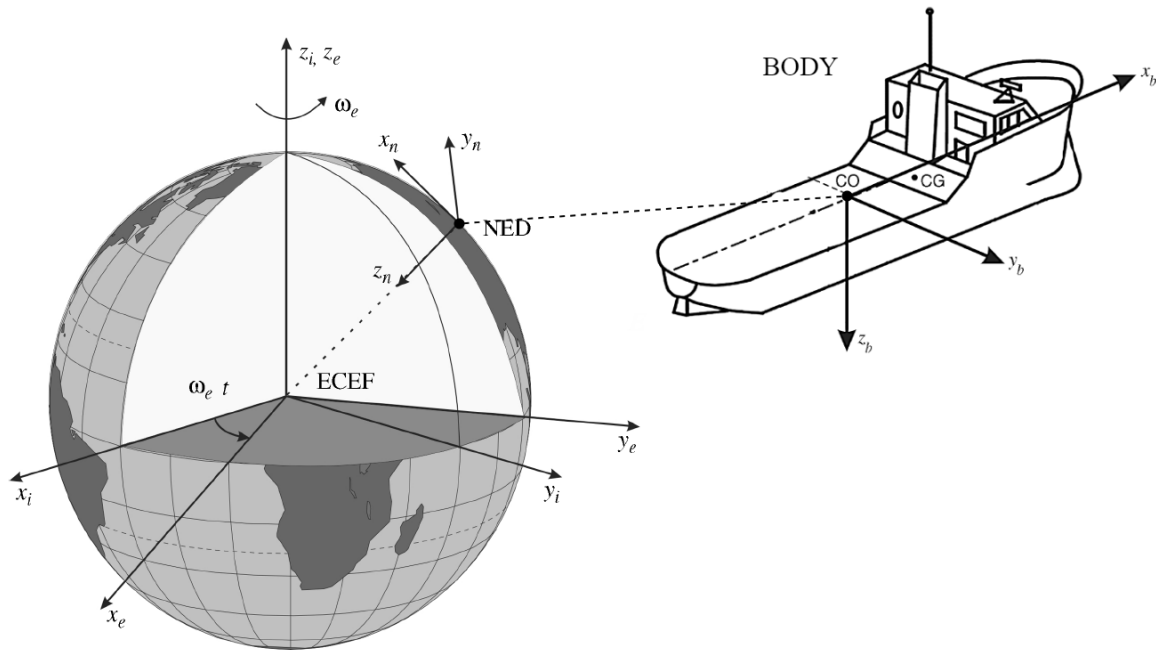


Figure 2-2: An overview of Reference Frames and the Body-fixed reference points [14]

Geographic Reference Frames (Tangent Planes)

- **NED $\{n\}$:** The North-East-Down (NED) coordinate system $\{n\} = (x_n, y_n, z_n)$ has its origin located at o_n , that is defined relative to the Earth's reference ellipsoid. It is typically defined as the tangent plane on the surface of the Earth moving with the craft but with axes pointing in different directions than the body-fixed axes of the craft. For this coordinate system, the x_n axis points towards true North, the y_n axis points towards East, while the z_n axis points downwards normal to the Earth's surface. The location of $\{n\}$ relative to ECEF is determined using two angles l and μ denoting the longitude and latitude, respectively. For marine craft operating in a local area (a geographical area of $10 \text{ km} \times 10 \text{ km}$), the longitude and latitude are approximated as constants; thus, an Earth-fixed tangent plane on the surface is used for navigation. It is usually referred to as flat Earth, for which one can suppose that $\{n\}$ is inertial such that Newton's laws still apply.

Body-Fixed Reference Frames

- **BODY $\{b\}$:** The body-fixed reference frame $\{b\} = (x_b, y_b, z_b)$ with origin o_b is a moving coordinate frame that is fixed to the craft. Linear and angular velocities of

the craft have to be expressed in the body-fixed coordinate system. In contrast, the position and orientation of the craft are described relative to the inertial reference frame (approximated by $\{n\}$ for marine crafts). Depending on the type of craft, the origin o_b is chosen appropriately. This point will be referred to as CO (see Figure 2-2). For marine craft, the body axes x_b , y_b and z_b are chosen to coincide with the principal axes of inertia, and they are usually defined as (for the terminology of the directions, see Figure 1-1a):

- x_b - longitudinal axis (directed from aft to fore)
- y_b - transversal axis (directed to starboard)
- z_b - normal axis (directed from top to bottom)

We define centre of gravity (CG) as the point where the total mass of the craft is treated as a point mass, and it is located at $r_g^b = [x_g, y_g, z_g]^T$ relative to CO.

2-3-2 6 DOF Vectorial Notation

The following notation is adopted for vectors in the coordinate systems $\{b\}$ and $\{n\}$ of a marine craft [14]:

- p_{nb}^n = position (distance) of the CO relative to o_n expressed in $\{n\}$
- Θ_{nb} = Euler angles from $\{b\}$ to $\{n\}$ (orientation of the marine craft with respect to NED)
- v_{nb}^b = linear velocity of the CO relative to o_n expressed in $\{b\}$
- ω_{nb}^b = angular velocity of $\{b\}$ with respect to $\{n\}$ expressed in $\{b\}$
- f_b^b = force with line of action through the point CO expressed in $\{b\}$
- m_b^b = moment about the point $\{o_b\}$ expressed in $\{b\}$

Thus, the different variables in Table 2-1 can now be conveniently expressed in a vectorial setting:

$$\begin{array}{ll}
 \text{NED position:} & p_{nb}^n = \begin{bmatrix} x_n \\ y_n \\ z_n \end{bmatrix} \in \mathbb{R}^3 & \text{Attitude (Euler angles):} & \Theta_{nb} = \begin{bmatrix} \phi \\ \theta \\ \psi \end{bmatrix} \in \mathbb{T}^3 \\
 \\
 \text{B-f linear velocity:} & v_{nb}^b = \begin{bmatrix} u \\ v \\ w \end{bmatrix} \in \mathbb{R}^3 & \text{B-f angular velocity:} & \omega_{nb}^b = \begin{bmatrix} p \\ q \\ r \end{bmatrix} \in \mathbb{R}^3 \\
 \\
 \text{B-f force:} & f_b^b = \begin{bmatrix} X \\ Y \\ Z \end{bmatrix} \in \mathbb{R}^3 & \text{B-f moment:} & m_b^b = \begin{bmatrix} K \\ N \\ M \end{bmatrix} \in \mathbb{R}^3
 \end{array}$$

where B-f denotes Body-fixed, \mathbb{R}^3 is the Euclidean space of dimension three and \mathbb{T}^3 denotes a torus of dimension three (shape of a sphere, 3-D), implying that there are three angles defined on the interval $[0, 2\pi]$. Generally, the motion of a marine craft in 6 DOF with o_b as the coordinate origin is described by the following vectors:

$$\eta = \begin{bmatrix} p_{nb}^n \\ \Theta_{nb} \end{bmatrix}, \quad \nu = \begin{bmatrix} v_{nb}^b \\ \omega_{nb}^b \end{bmatrix}, \quad \tau = \begin{bmatrix} f_b^b \\ m_b^b \end{bmatrix}$$

where $\eta \in \mathbb{R}^3 \times \mathbb{T}^3$ represents the position and orientation vector, $\nu \in \mathbb{R}^6$ represents the linear and angular velocity vectors that are decomposed in the body-fixed reference frame

and $\tau \in \mathbb{R}^6$ is used to describe the forces and moments acting on the craft in the body-fixed frame.

2-3-3 Euler Angle Transformation between BODY and NED

The 6 DOF kinematic equations that relate the BODY and NED reference frames are expressed in vector form as:

$$\begin{aligned} \dot{\eta} &= J_{\Theta}(\eta)\nu \\ &\Updownarrow \\ \begin{bmatrix} \dot{p}_{nb}^n \\ \dot{\Theta}_{nb} \end{bmatrix} &= \begin{bmatrix} R_b^n(\Theta_{nb}) & O_{3 \times 3} \\ O_{3 \times 3} & T_{\Theta}(\Theta_{nb}) \end{bmatrix} \begin{bmatrix} v_{nb}^b \\ \omega_{nb}^b \end{bmatrix} \end{aligned}$$

where J_{Θ} is the transformation matrix, that is build up of the linear velocity transformation matrix $R_b^n(\Theta_{nb})$ and the angular transformation matrix $T_{\Theta}(\Theta_{nb})$ [14]. The definitions of these matrices are given as follows:

$$R_b^n(\Theta_{nb}) = \begin{bmatrix} c\psi c\theta & -s\psi c\phi + c\psi s\theta s\phi & s\psi s\phi + c\psi c\phi s\theta \\ s\psi c\theta & c\psi c\phi + s\phi s\theta s\psi & -c\psi s\phi + s\theta s\psi c\phi \\ -s\theta & c\theta s\phi & c\theta c\phi \end{bmatrix} \quad (2-2)$$

$$T_{\Theta}(\Theta_{nb}) = \begin{bmatrix} 1 & s\phi t\theta & c\phi t\theta \\ 0 & c\phi & -s\phi \\ 0 & s\phi/c\theta & c\phi/c\theta \end{bmatrix} \quad (2-3)$$

where we use the abbreviations $s \cdot = \sin(\cdot)$, $c \cdot = \cos(\cdot)$ and $t \cdot = \tan(\cdot)$. The definitions of $R_b^n(\Theta_{nb})$ and $T_{\Theta}(\Theta_{nb})$, shows that J_{Θ} depends on the Euler angles. Therefore, the kinematic equations for the system are nonlinear.

The $R_b^n(\Theta_{nb})$ is described by three principal rotations about the z , y and x axes (zyx convention). It is worth noting that the order in which these rotations are performed is not arbitrary. In guidance, navigation and control applications, it is common to use the zyx convention from $\{n\}$ to $\{b\}$ specified in terms of the Euler angles ϕ , θ and ψ for the rotations. This rotation sequence is described mathematically as

$$R_b^n(\Theta_{nb}) := R_{z,\psi} R_{y,\theta} R_{x,\phi}$$

where principal rotation matrices (one axis rotations) are defined as:

$$R_{x,\phi} = \begin{bmatrix} 1 & 0 & 0 \\ 0 & c\phi & -s\phi \\ 0 & s\phi & c\phi \end{bmatrix}, \quad R_{y,\theta} = \begin{bmatrix} c\theta & 0 & s\theta \\ 0 & 1 & 0 \\ -s\theta & 0 & c\theta \end{bmatrix}, \quad R_{z,\psi} = \begin{bmatrix} c\psi & -s\psi & 0 \\ s\psi & c\psi & 0 \\ 0 & 0 & 1 \end{bmatrix} \quad (2-4)$$

2-4 Rigid-Body Kinetics

The Nonlinear 6 DOF Rigid-Body EOM are derived using the Newton–Euler formulation and vectorial mechanics, which are defined in the vectorial setting as:

$$M_{RB}\dot{\nu} + C_{RB}(\nu)\nu = \tau_{RB} \quad (2-5)$$

where M_{RB} is the rigid-body mass matrix, $C_{RB}(\nu)$ is the rigid-body Coriolis and centripetal matrix due to the rotation of $\{b\}$ about the inertial frame $\{n\}$, $\nu = [u, v, w, p, q, r]$ is the generalized velocity vector expressed in $\{b\}$ and $\tau_{RB} = [X, Y, Z, K, M, N]$ is a generalized vector of external forces and moments expressed in $\{b\}$ [14].

The external forces are given by the sum:

$$\tau_{RB} = \tau_c + \tau_{wave} - g(\eta),$$

and their content will be discussed in the following sections.

The matrices M_{RB} and $C_{RB}(\nu)$ of Eq. (2-5) are given as follows:

$$M_{RB} = \begin{bmatrix} m & 0 & 0 & 0 & mz_g & -my_g \\ 0 & m & 0 & -mz_g & 0 & mx_g \\ 0 & 0 & m & my_g & -mx_g & 0 \\ 0 & -mz_g & my_g & I_x & -I_{xy} & -I_{xz} \\ mz_g & 0 & -mx_g & -I_{yx} & I_y & -I_{yz} \\ -my_g & mx_g & 0 & -I_{zx} & -I_{zy} & I_z \end{bmatrix} \quad (2-6)$$

$$C_{RB}(\nu) = \begin{bmatrix} 0 & 0 & 0 & 0 & 0 & 0 \\ 0 & 0 & 0 & 0 & 0 & 0 \\ 0 & 0 & 0 & 0 & 0 & 0 \\ -m(y_gq + z_gr) & m(y_gp + w) & m(z_gp - v) & 0 & 0 & 0 \\ m(x_gq - w) & -m(z_gr + x_gp) & m(z_gq + u) & m(y_gq + z_gr) & -m(x_gq - w) & -m(x_gr + v) \\ m(x_gr + v) & m(y_gr - u) & -m(x_gp + y_gq) & -m(y_gp + w) & m(z_gr + x_gp) & -m(y_gr - u) \\ & & & -m(z_gp - v) & -m(z_gq + u) & m(x_gp + y_gq) \\ & & & 0 & -I_{yz}q - I_{xz}p + I_zr & I_{yz}r + I_{xy}p - I_yq \\ & & & I_{yz}q + I_{xz}p - I_zr & 0 & -I_{xz}r - I_{xy}q + I_xp \\ & & & -I_{yz}r - I_{xy}p + I_yq & I_{xz}r + I_{xy}q - I_xp & 0 \end{bmatrix} \quad (2-7)$$

where I_x , I_y and I_z are the moments of inertia about the x_b , y_b and z_b axes, $I_{xy} = I_{yx}$, $I_{xz} = I_{zx}$ and $I_{yz} = I_{zy}$ are the products of inertia, and m represents the total mass of the hydrofoil craft. These parameters, as well as the vector r_g^b are obtained by the use of a computer-aided design (CAD) software like in article [7] where they consider an underwater remotely operated vehicle (ROV).

When CO coincides with the CG ($r_g^b = [0, 0, 0]^T$) and by the assumption that the hydrofoil craft has homogeneous mass distribution and xz-plane symmetry, then $I_{xy} = I_{yz} = 0$ [14]. Additionally, it is assumed that the hydrodynamic force caused by the propeller(s), i.e. thrust, only influences the hydrodynamic forces X , Z , and the hydrodynamic moment K , that lie in the plane of symmetry [36]. This assumption can also be found in aircraft dynamics, which generally have many similarities with the dynamics of a hydrofoil craft. Consequently, it is common to split the set of EOM of a marine craft into two parts using these assumptions. One describes the motion in the symmetry plane of the marine vessel, i.e., the symmetric motions (longitudinal), and the other part describes the asymmetric motions (lateral) [36], [11]. Hence this classification of motions is summarized in Table 2-2:

Table 2-2: Classification of motions

Symmetric motions (longitudinal)	Asymmetric motions (lateral)
x (surge)	y (sway)
z (heave)	ϕ (roll)
θ (pitch)	ψ (yaw)

It is worth noting that the previous statement holds as long as the deviations from equilibrium points and disturbances remain small; thus, no hydrodynamic coupling exists between the symmetric and the asymmetric DOFs [36].

For the case of HEARP, the system is not entirely symmetrical by design, so the CG is shifted by a few centimetres to the right side of the craft (see Section 3-5). This leads to nonzero values for the products of inertia for I_{xy} and I_{yz} . Additionally, due to the rotatable podded propeller, the generated thrust does not affect only the hydrodynamic forces and forces of the symmetric set of motions but also the asymmetrical ones. Hence, the different motions of the craft are not completely decoupled. This fact also gives reasoning for the choice to model and control the motions of heave, roll and pitch, which combines the theoretically symmetrical and asymmetrical motions.

2-5 Hydrostatics

In the terminology of hydrostatics, the gravitational and buoyancy forces are called restoring forces and are comparable to the spring forces in a mass–damper–spring system. For a floating craft, the restoring forces are defined by the volume of the displaced fluid, the location of the centre of buoyancy (CB), the area of the water plane and its associated moments. The aforementioned restoring forces are dominant for the hullborne mode of the hydrofoil craft. However, in the case of the foilborne mode, the lift forces are more dominant and support the largest portion of the weight of the hydrofoil craft. Therefore a hydrofoil craft operating in foilborne cannot be considered a floating vessel. It is assumed that the buoyancy force B is negligible (small displaced volume by T-foils, struts, rudder and propeller) with respect to the magnitude of the lift forces F_L . Then B force is omitted ($B \approx 0$), and with the choice of CO coinciding with CG, we can approximate the vector $g(\eta)$ as follows [14]:

$$g(\eta) \approx \begin{bmatrix} mg \sin(\theta) \\ -mg \sin(\phi) \cos(\phi) \\ -mg \cos(\phi) \cos(\theta) \\ 0 \\ 0 \\ 0 \end{bmatrix} \quad (2-8)$$

It is remarkable to mention that the resulting vector $g(\eta)$ depends only on the gravitational force, and it is equivalent to the vector of external forces and moments due to gravity for an aircraft [36].

2-6 Hydrodynamics

The ship dynamics study has mainly been covered by two main theories: manoeuvring and seakeeping. Manoeuvring represents the study of motion of marine crafts in the absence of wave excitation (calm water). Conversely, seakeeping represents the study of motion of marine crafts on constant heading ψ and speed U (which includes the case of zero speed), when there is wave excitation. Even though both approaches are concerned with the same topics, the study of motion, stability and control, the distinction between them allows us to make different assumptions that simplify the study in each case.

In seakeeping analysis, the hydrodynamic forces are frequency-dependent and take into account the fluid memory effects. On the other hand, in manoeuvring theory, hydrodynamic coefficients are approximated by constant values; hence fluid memory effects are omitted. The main results of this section rely on the assumption that the hydrodynamic forces and moments are approximated at one frequency of oscillation such that the fluid-memory effects are neglected. This leads to a nonlinear mass–damper–spring system with constant coefficients [14].

2-6-1 Hydrodynamic Added Mass and Coriolis–Centripetal Forces

Hydrodynamic added mass is considered a virtual mass added to a system since an accelerating or decelerating body has to move some volume of the surrounding fluid as it advances through it. The expressions for the Coriolis and centripetal matrix $C_A(\nu)$ are derived using the fluid kinetic energy via an energy formulation. More precisely, one can consider a Lagrangian framework based on nonlinear manoeuvring theory for a rotating frame $\{b\}$ with respect to $\{n\}$. Based on Lagrangian theory, the hydrodynamic Coriolis and centripetal matrix $C_A(\nu)$ is a function of added mass M_A . A detailed analysis of these forces is found in [14].

Liu et al. [30] stated that for a fully-submerged hydrofoil craft, the added mass is minimal compared to the mass of the whole craft; therefore these hydrodynamic terms are neglected. An extensive study should investigate how these parameters can be calculated or identified and check whether their magnitude is significant compared to the parameters of rigid-body matrices. In this study, in order to reduce the complexity of the derived dynamical model, the added mass and the hydrodynamic Coriolis–centripetal forces are neglected.

2-6-2 Damping Forces

The hydrodynamic damping of a marine craft is mainly originated from: Potential Damping, Skin Friction, Wave Drift Damping, Damping Due to Vortex Shedding and Lifting Forces. The various damping terms contribute to both linear and quadratic damping. Nevertheless, it is challenging to separate these effects. In this study, for simplicity, we assume that the hydrodynamic damping for the hydrofoil craft includes only drag and lift forces acting on the hydrofoils, so all the other effects will be neglected, like in the work of [40]. A more detailed analysis of how these forces are modelled is presented in Section 2-8.

2-7 Waves

A hydrofoil craft operating in ambient waves is subject to unsteady excitation forces due to the incident waves. These excitation forces are usually quite significant since the craft is moving at a high cruise velocity; hence the encounter frequency with the incident wave system is also considerable [19]. Kim and Yamato [26] performed an experiment of hydrofoil lift measurement in regular waves for heading seas to confirm the variations due to the excitation force. From this experiment, they observed that the variation might reach up to 30% of the total lift of hydrofoil in regular waves. Therefore, it is concluded that the effect of ambient waves on the hydrofoil dynamics is significant.

The sea waves are typically generated through the action of the natural wind and gravity, and generally are irregular and random. For example, no two waves have precisely the same height, and they may travel across the surface at different speeds and in different directions. Regular (harmonic) waves never occur in the natural ocean environment, although they can be produced in laboratory towing tanks and form the basis of many seakeeping model experiments. The theory of irregular waves is based on the assumption that they can be represented by 'superposing' or adding together a suitable assembly of regular waves. Therefore, a comprehensive understanding of the physics of regular waves is one of the essential tools in the study of ship seakeeping behaviour [32].

In this study, a dynamical model of regular waves is combined with the dynamical model of the HEARP with the aim to simulate the response of the craft in the presence of incident waves. In order to develop this dynamical model, the following assumptions are made:

- Interaction between the waves and the craft is solely modelled by the wave-induced local velocity of the water surrounding the hydrofoils.
- The effect of integrating the loads due to the linear hydrodynamic pressure in the incident waves (Froude-Kriloff forces) is neglected [12].
- The effect of the hydrofoils and the struts on the incident waves is neglected. Thus, it is assumed that the fore and aft hydrofoils encounter the same unaffected waves but in different positions.

In this section, the characteristics of ideal regular waves are introduced by taking inspiration mainly from the book of [32].

2-7-1 Linear wave theory

The mathematical model of a regular wave that is used in this study is based on some fundamental assumptions of the linear wave theory, which are summarized below:

- The water is incompressible and inviscid.
- Waves propagate in the x -direction in a fluid with an infinite horizontal extent and no obstacles present.
- The water flow field is irrotational.
- Small-amplitude approximation, i.e. amplitude of the wave is small compared with the wave length and the water depth.

In Figure 2-3, it is shown a series of regular waves advancing across the surface of a body of water with constant depth d . The local coordinate system of the wave is denoted by

$\{w\} = (x_w, y_w, z_w)$ and has its origin at o_w . The waves are long-crested and two-dimensional: they propagate in the positive x_w direction, the crests are perpendicular to the x_w -axis, and they extend to infinity on either side of x_w -axis. Each wave crest progresses with the steady velocity c_w (the so-called wave celerity), so the waves never overtake each other. The wave length λ is defined as the horizontal distance between two consecutive crests, while the wave period T is defined as the time interval between two consecutive crests passing a fixed point. Where ζ_0 is the wave amplitude at the mean level of the sea surface ($z_w = 0$).

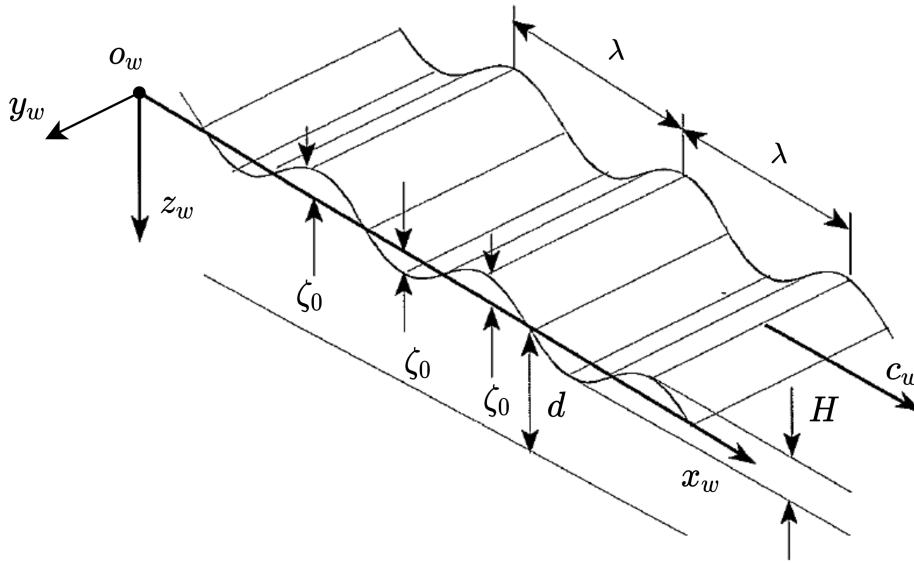


Figure 2-3: Regular wave [32]

Subsequently, the wave number k , the wave frequency ω and the wave celerity c_w are defined as:

$$\omega = \frac{2\pi}{T}; \quad k = \frac{2\pi}{\lambda}; \quad c_w = \frac{\omega}{k} \quad (2-9)$$

Assuming deep water, i.e. $d > \frac{\lambda}{2}$, the relation between the wave length and the wave frequency is defined by the following equation:

$$\lambda = \frac{2\pi g}{\omega^2} \quad (2-10)$$

With the use of velocity potential techniques of classical fluid dynamics and equation Bernoulli, the instantaneous depression (wave profile) of the water particles at constant depth z_w is defined as:

$$\zeta_h(t, x_w, z_w) = \zeta_0 e^{-kz_w} \sin(kx_w - \omega t) \quad (2-11)$$

where x_w and z_w denote the coordinates of some arbitrary point.

From Eq. (2-11), one can observe that as the depth z_w increases, the depression ζ_h of the wave decreases due to the exponential term. This equation can explain why the water is more 'calm' at large depths.

The velocity components of water particles at any point under the wave are calculated by:

$$u'_w(t, x_w, z_w) = -\frac{gk\zeta_0}{\omega} e^{-kz_w} \sin(kx_w - \omega t) \quad (2-12a)$$

$$v'_w(t, x_w, z_w) = 0 \quad (2-12b)$$

$$w'_w(t, x_w, z_w) = -\frac{gk\zeta_0}{\omega} e^{-kz_w} \cos(kx_w - \omega t) \quad (2-12c)$$

2-7-2 Wave Conditions

The wave conditions that are used for the control design and the simulations, are chosen based on the size of HEARP and the available equipment of the towing tank of TU Delft. Firstly, recall that the HEARP craft has a scaled size, so it is obvious that its operation in regular waves is limited by the length of its struts that support the hydrofoils. Based on the size of the struts and the other components of HEARP (see Section 3-5), the craft can operate in waves with an amplitude of $0 \leq \zeta_0 \leq 0.1m$, so the simulations are performed by considering this range of wave amplitudes.

It is a fact that wind-generated gravity waves are only one type amongst a variety that occurs in the oceans and along the shores of the world. All these waves can be ordered in terms of their period or wave length (see Figure 2-4) [21]. Looking at Figure 2-4, one can deduce that the wind-generated waves have approximately a period of $0.1 \text{ s} < T < 10 \text{ s}$. Based on the capabilities of the Towing Tank No. 1 of the Department of Maritime and Transport Technology of TU Delft [23], the available wave maker can generate regular waves with wave length $0.3 \text{ m} < \lambda < 6 \text{ m}$. In this study, it is decided that the control design and simulations with the regular waves are done by considering the wave length range of $1 \text{ m} \leq \lambda \leq 5 \text{ m}$ that lies within the capabilities of Towing Tank No. 1. It is worth noting that the length of HEARP (equals to 1.5 m, see Table 3-4) lies within this range. Using Eq. (2-9) and Eq. (2-10), the aforementioned wave length range give us a frequency that lies in the range $7.85 \text{ rad/s} \geq \omega \geq 3.51 \text{ rad/s}$ and a period that lies in the range $0.80 \text{ s} \leq T \leq 1.79 \text{ s}$. The resulting range of wave periods lies in the expected range of periods for wind-generated waves (see Figure 2-4).

2-7-3 Encounter Angle and Encounter Frequency

Although the wave frequency ω considerably influences the motions of a marine craft in regular waves, the motions are mostly dependent on the frequency with which the moving craft encounters the waves. The encounter angle β shown in Figure 2-5a, is defined as the angle between the heading of the craft and the direction of the waves. Depending on the value of this angle, we can categorize the waves as illustrated by Figure 2-5a. For example, with $\beta = 0^\circ$ we refer to following sea while with $\beta = 180^\circ$ we refer to head sea [32].

By assuming that the craft attempts to maintain a straight line track at a constant cruise speed U across the sea surface, the corresponding encounter frequency ω_e is described by:

$$\omega_e = \omega - \frac{\omega^2 U}{g} \cos(\beta) \quad (2-13)$$

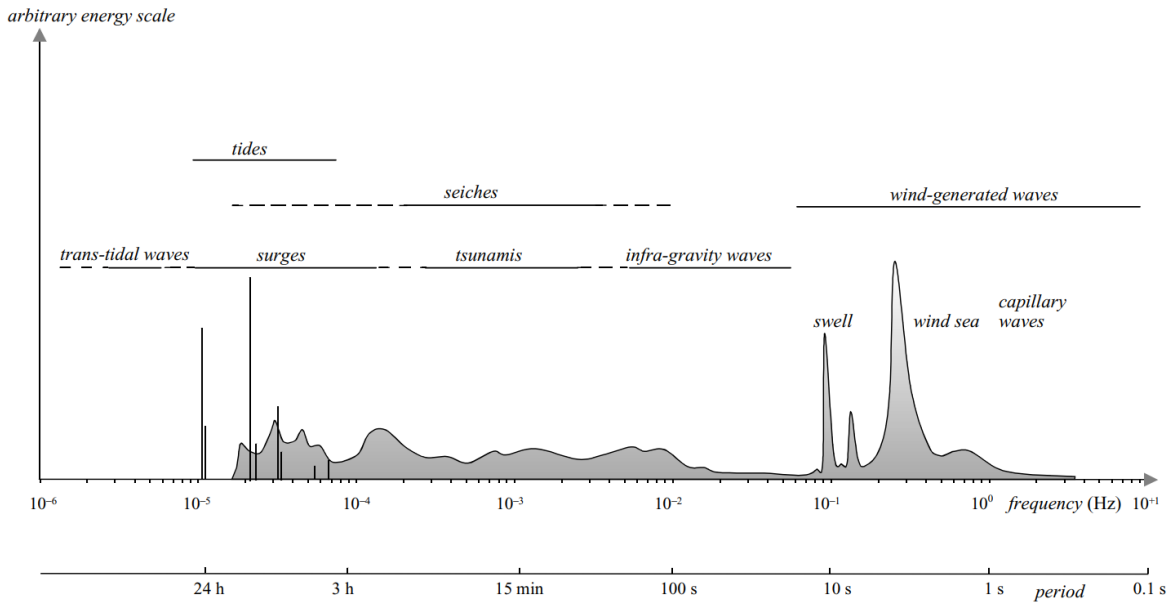


Figure 2-4: Frequencies and periods of the vertical motions of the ocean surface [21]

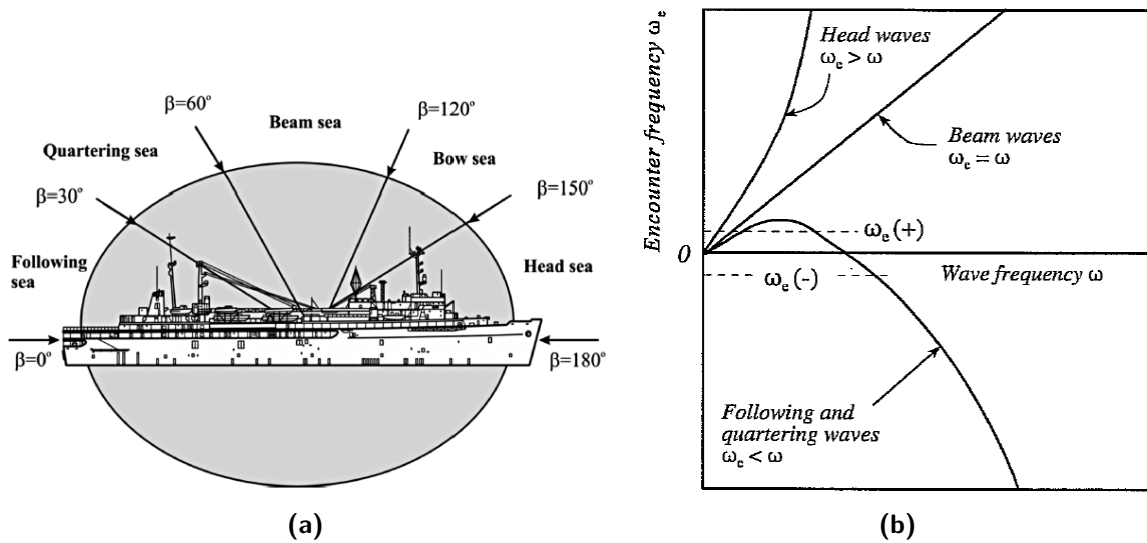


Figure 2-5: (a) Definition of encounter angle β [14] and (b) Encounter frequency and heading [32]

The influence of the heading of the craft on the encounter frequency is illustrated by Figure 2-5b. A negative encounter frequency means that the craft is overtaking the waves, while a positive encounter frequency means that the waves are overtaking the craft.

To consider the encounter angle and the encounter frequency in the mathematical model of the regular wave, the velocity components presented in Eq. (2-12) have to be reformulated. Thus, the wave coordinate system is rotated around z_w -axis by an angle β using a principal rotation of Euler angle $R_{z_w, \beta}$ (see Eq. (2-4)). Additionally, the frequency ω that lies inside the sine and cosine functions of Eq. (2-12) have to be replaced by the encounter frequency ω_e

[12]. Finally, the reformulated velocity components of the water particles are defined as:

$$\begin{bmatrix} u_w(t, x_w, z_w) \\ v_w(t, x_w, z_w) \\ w_w(t, x_w, z_w) \end{bmatrix} = \underbrace{\begin{bmatrix} \cos(\beta) & -\sin(\beta) & 0 \\ \sin(\beta) & \cos(\beta) & 0 \\ 0 & 0 & 1 \end{bmatrix}}_{R_{z_w, \beta}} \begin{bmatrix} u'_w \\ v'_w \\ w'_w \end{bmatrix} = \begin{bmatrix} -\frac{gk\zeta_0}{\omega} e^{-kz_w} \sin(kx_w - \omega_e t) \cos(\beta) \\ -\frac{gk\zeta_0}{\omega} e^{-kz_w} \sin(kx_w - \omega_e t) \sin(\beta) \\ -\frac{gk\zeta_0}{\omega} e^{-kz_w} \cos(kx_w - \omega_e t) \end{bmatrix} \quad (2-14)$$

Note here that because of a simplified 2D model for the wave-induced excitation forces presented later in Section 2-8-3, in this study, only following and head waves are used for the simulations. Therefore, the v_w component of the regular wave velocity field of Eq. (2-14) is omitted because of the fact that for either $\beta = 0^\circ$ (following sea) or $\beta = 180^\circ$ (head sea), we have that $\sin(\beta) = 0$.

2-8 Hydrofoil Lift and Drag Forces

When a hydrofoil vessel is sailing on the water surface, the hydrofoil surface will be at a certain angle of attack relative to the water flow and generates lift and drag forces and moments on the vessel [22]. The variation of lift and drag forces plays a crucial role in the hydrofoil craft motion [4]. For the sake of simplicity, in this study, the hydrodynamic forces acting on the strut of the hydrofoil and the side-way drag forces in the y direction of the hydrofoil are neglected. Thus, the effect of the hydrodynamic forces at the connection of the hydrofoil with its strut is also neglected. This section contains topics relevant to the detailed modelling of the hydrodynamic forces and moments.

2-8-1 Foil Geometry

To describe the geometry of a foil, a well-known standard nomenclature is used, which is presented in Figure 2-6. By considering the foil sketched in Figure 2-6, the following definitions are given [1], [37]:

- **Mean camber line::** The locus of points that are equidistant from the upper and lower surfaces of the foil.
- **Leading edge:** The part of the foil (edge) that hits the fluid particles first.
- **Trailing edge:** The part of the foil (edge) that hits the fluid particles last.
- **Chord line:** Straight line connecting the leading and trailing edges of the foil.
- **Chord c :** Distance between the leading and trailing edges measured along the chord line.
- **Camber:** Maximum distance between the mean camber line and the chord line, measured perpendicular to the chord line.
- **Span s :** Distance between the two edges (wing tip) of the wing, i.e. the width of the wing.
- **Planform:** The shape of the wing, when viewed from above looking down onto the wing.
- **Foil area A_h :** Projected area of the planform that is bounded by the leading and trailing edges and the wing tips.

- **Aspect Ratio AR :** Ratio between the square of the span s and the wing area A , i.e.

$$AR = \frac{s^2}{A}$$

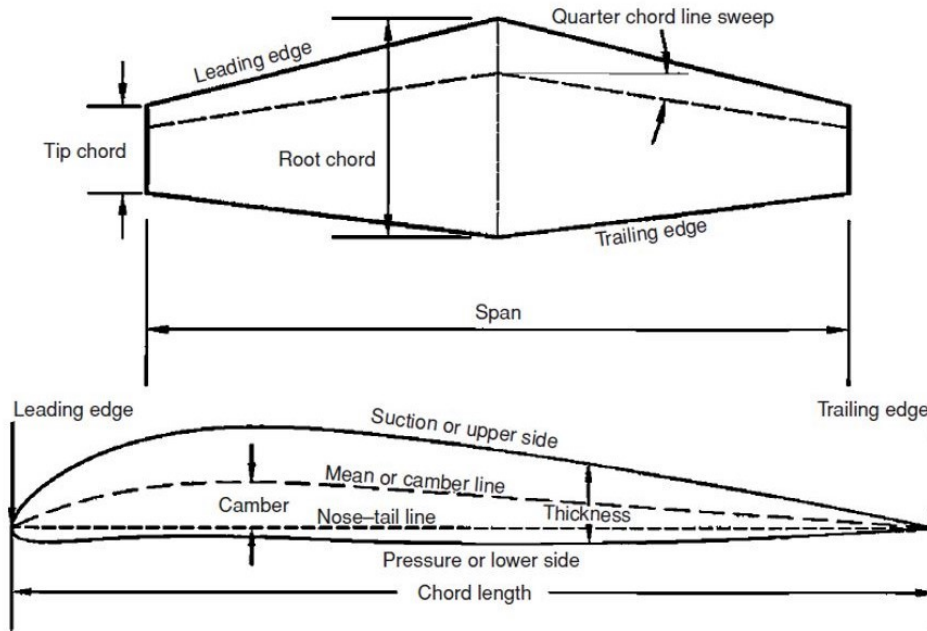


Figure 2-6: Foil Geometry [12]

2-8-2 Actuation mechanism

In the baseline design of HEARP, the dual servo actuation system of the Foil-Strut is used synchronously to actuate the module in the pitch direction. The rotating servo arm and the translating foil arm are connected by actuation rods. Due to the rigid rudder hinge body connection, the foil arm translates around the pitch axis.

In order to obtain an equation which relates the angle of the servo motor and the actuated pitch angle of a T-foil, Flying Fish has performed an extensive analysis for the joint of the Foil & Strut Module [13]. In this analysis, several distances and angles were defined as the attainable foil angles as a function of the actuation angle of servo motor θ_{servo} . Some of them are schematically depicted in the side and top views of the joint in Figure 2-7. From these joint schematics, the geometrical and kinematic relations were deduced. The primary variable of interest is the pitch angle of the foil or in other words, the foil angle of attack α (see Figure 2-7).

Based on the analysis of Flying Fish, a kinematic equation which can relate α with θ_{servo} directly cannot be derived. However, with an iterative procedure and a combination of different non-linear equations, they were able to relate α with θ_{servo} . This analysis was verified against measurements from a kinematic model in Fusion 360 CAD software. The results for a servo angle θ_{servo} ranging from -80° to 80° are depicted in Figure 2-8. From these results, it is observed that this relation is non-linear for large angles.

As it is shown in Figure 2-8, for $-30^\circ < \theta_{servo} < 30^\circ$, we may approximate the non-linear relation between α with θ_{servo} with a linear function. Hence, within the range $-10^\circ < \alpha < 10^\circ$,

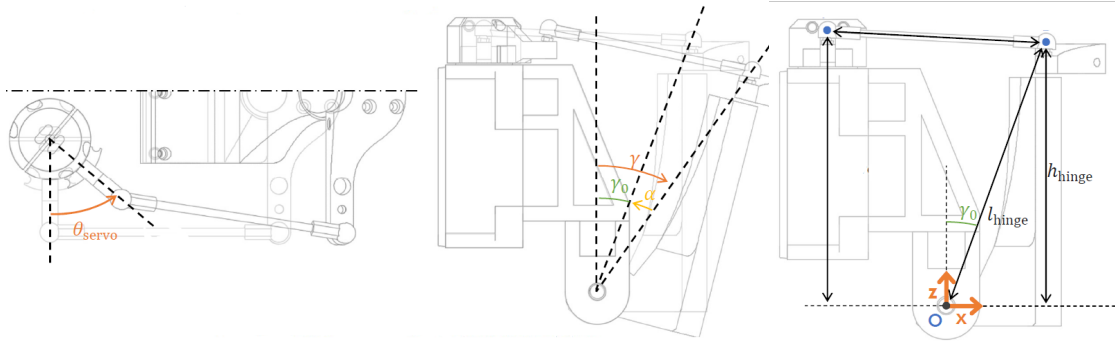


Figure 2-7: Geometrical analysis of T-foil actuation mechanism [13].

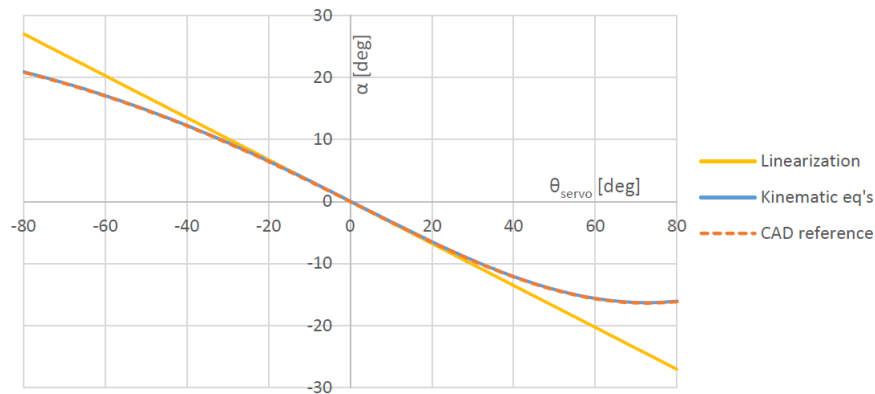


Figure 2-8: Foil angle of attack vs Servo actuation angle [13]

the linear approximation can accurately describe the relationship between the two angles. This approximation consists of the ratio of the two instantaneous arms of rotation:

$$\alpha_s \approx -\frac{l_s}{h_h} \theta_{servo} \quad (2-15)$$

where l_s and h_h corresponds to the distances l_{servo} and h_{hinge} respectively as they are defined in Figure 2-7. Note that the angle α_s corresponds to the angle α which is defined previously. This angle is called the swinging angle of the hydrofoil α_s (pitching angle of the hydrofoil with respect to craft BODY). For the sake of notation, the actual angle of the servo motor θ_{servo} is defined as δ_s , i.e. $\delta_s = \theta_{servo}$.

It is worth noting that the maximum achievable range of swinging angle α_s is constrained by the geometry of the joint. More precisely it is constrained to operate within the range $-10^\circ \leq \alpha_s \leq 23.5^\circ$. By using Eq. (2-15) and the values of the parameters (see Table 3-5), the operating range of the servo motors is $-69.72^\circ \leq \delta_s \leq 29.67^\circ$. This operating range is taken during the control design procedure (Chapter 4) to ensure that the actuators do not saturate during the expected operating conditions of HEARP.

In order to derive the equations for the location of the hydrofoil's centre of pressure (CP) (see Section 2-8-3) with respect to the CG of the craft, another geometrical analysis it is made. This geometrical analysis is shown in Figure 2-9, where one can see the distances between the joint and the CP of the hydrofoil. From this diagram, we obtain the following expression for

the angle γ_0 based on the trigonometry rules:

$$\gamma_0 = \arccos\left(\frac{l_{a_0}}{l_c}\right) \quad (2-16)$$

where l_{a_0} and l_c are constant distances that are measured with $\alpha_s = 0$ (chord line of hydrofoil parallel to the horizontal plane of the hydrofoil craft).

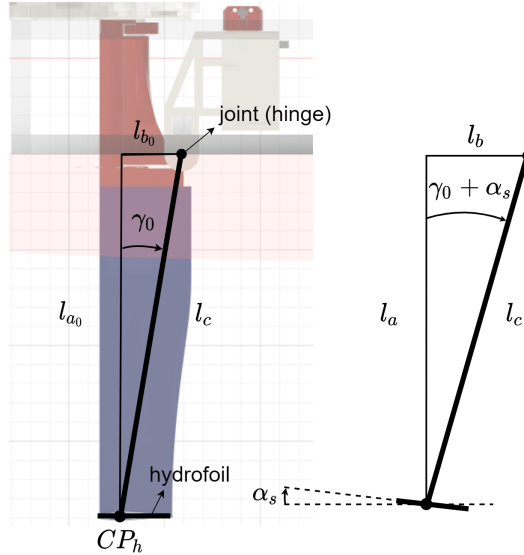


Figure 2-9: Geometrical analysis for the determination of the location of CP of the hydrofoil

The actuator dynamics of the servo motors are modelled as first order phase-lag systems (low-pass filters) with time constant τ_δ . The transfer function from the commanded servo motor angle $\delta_{s,c}$ to the actual servo motor angle δ_s becomes:

$$g_{sm}(s) = \frac{\delta_s}{\delta_{s,c}} = \frac{1}{\tau_\delta s + 1} \quad (2-17)$$

To give a simple interpretation of the transfer function of (2-17), assume that we give a unit-step command signal $\delta_{s,c}$. Then the time-domain response of the angle δ_s is described by:

$$\delta_s(t) = 1 - e^{-t/\tau_\delta}, \quad \text{for } t \geq 0 \quad (2-18)$$

From the Eq. (2-18), it is observed that initially, the output $\delta_s(t)$ is zero, and finally, it becomes unity. Note that as the time constant τ_δ decrease, the speed of the system response increases [38]. It is assumed that this first-order model is capable to capture sufficiently well the internal dynamics of the servo motors.

2-8-3 Modelling of hydrodynamic forces

Figure 2-10 illustrates the free-body diagram for the analysis of the hydrodynamical forces (lift F_L and drag F_D) acting on a hydrofoil. The local hydrofoil coordinate frame is defined as $\{h\} = (x_h, y_h, z_h)$, and x_h and z_h are parallel to the BODY x and z axes respectively.

According to the right-hand rule, the y_h -axis is supposed to go inward and is parallel to the BODY y -axis (is not drawn in Figure 2-10). The origin of coordinate frame $\{h\}$ is fixed at the CP of the hydrofoil. It is defined as the location where the resultant of a distributed load effectively acts on the hydrofoil. The resulting moment equals zero by integrating the effect of the distributed loads about the CP. In general, the location of the CP varies with the different angles of attack. Nevertheless, for sufficiently small angles of attack, a theoretical result proves that the CP is located at the quarter-chord point (back from the leading edge) for a symmetric foil [1]. So it is assumed that the hydrodynamic forces are applied at this point, which is located at r_h^b with respect to the CG of the craft:

$$r_h^b = [l_x, l_y, l_z]^T \quad (2-19)$$

where l_x , l_y and l_z are the moment arms of the hydrofoil (perpendicular distances from the CG of the craft).

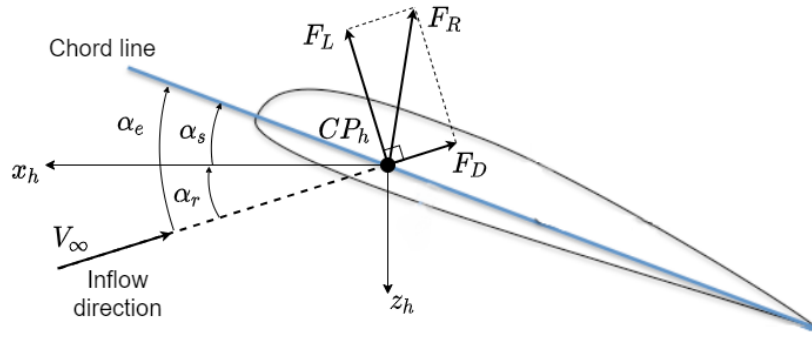


Figure 2-10: Free-body diagram of the hydrofoil

Because of the rotation about the hinge of the hydrofoil actuation mechanism (see Figure 2-9), l_x and l_z distances are functions of the swinging angle α_s , and they are defined as:

$$l_x(\alpha_s) = l_{x_j} + l_b = l_{x_j} + \sin(\gamma_0 + \alpha_s)l_c \quad (2-20a)$$

$$l_z(\alpha_s) = l_{z_j} + l_a = l_{z_j} + \cos(\gamma_0 + \alpha_s)l_c \quad (2-20b)$$

The distances l_{x_j} and l_{z_j} denote the horizontal and the vertical distances, respectively, between the joint (hinge) of the actuation mechanism of the hydrofoil and the CG of the hydrofoil craft. Additionally, the distance l_c and the angle γ_0 have defined previously in Eq. (2-16). It is important to mention that by looking to Eq. (2-20) one can deduce that for the aft hydrofoils, the absolute distance $|l_x(\alpha_s)|$ decreases as the α_s increases. This is because the quantity l_{x_j} is negative (located "behind" CG) while the quantity $\sin(\gamma_0 + \alpha_s)l_c$ is positive. Hence, this reduces the capability of the aft hydrofoils to influence pitch motion. The opposite phenomenon holds for the aft hydrofoil in which absolute distance $|l_x(\alpha_s)|$ increases as the α_s increases.

The resulting hydrodynamic force F_R acting on the hydrofoil is divided into (see Figure 2-10): the lifting component F_L , which is perpendicular to the relative water flow direction (negative z -axis), and the drag component F_D , which is parallel to the water flow direction (negative x -axis).

The definition of the different angles in Figure 2-10 are summarised below:

- α_r : Relative angle between the water flow direction and the x-axis of the hydrofoil.
- α_s : Swinging angle of the hydrofoil (pitching angle of the hydrofoil with respect to craft body) defined as the angle between the chord line of the hydrofoil and the x_h -axis (see Figure 2-15). This angle is considered the control input as the servo motors regulate it (see Section 2-8-2).
- α_e : Effective angle of attack between the chord line of the hydrofoil and the water flow direction.

The positive direction of these angles is determined by the right-hand rule for rotation about the y_f axis. The effective angle of attack α_e is originated from the extra angle caused by the motions of the craft BODY and the incident waves ([11], [22], [42], [28], [25], [40]). For variable incidence hydrofoils, α_e includes three parts:

- α_s : Swinging angle of the hydrofoil.
- θ : Pitching angle of the BODY of the craft.
- α_∞ : Additional angle caused by the change of water inflow velocity due to velocity perturbations of the hydrofoil. It originates from the velocities of the craft and the velocity components of the incident waves (see Figure 2-11).

The cruise speed U of the hydrofoil craft moving in the horizontal plane is defined as [14]:

$$U = \sqrt{u^2 + v^2} \quad (2-21)$$

In the presence of incident waves, the variation of force and moment originate from the temporal and spatial variation of water particles' velocity in the wave field, which eventually causes the change of attack angle in the hydrofoil. As mentioned in Section 2-7, the interaction between the waves and the craft is solely modelled by the wave-induced local velocity of the water surrounding the hydrofoils. Therefore, to incorporate the effect of incident waves into the modelling of the lift and drag forces, a simplified two-dimensional model of the incident wave is used ([19], [26] and [40]). It is assumed that the craft is advancing with steady velocity U in the presence of regular waves. Under these conditions, the change of water inflow velocity due to perturbations arising from the motions of the craft and the wave velocity components w_w and u_w is analysed in Figure 2-11. As it is shown, due to the velocity perturbations in x and z axes, the inflow velocity is equal to V_∞ and has an inclined direction by the angle α_∞ .

From Figure 2-11, it can be seen that the local coordinate frame of the waves o_w coincides with the NED frame. This choice is convenient because the position coordinates of the velocity components of the regular wave in Eq. (2-14) can be replaced by the instantaneous position of each hydrofoil expressed in the NED frame. For each time instant, the origin of the craft has a position p_{nb}^n and orientation Θ_{nb} relative to the NED frame. Recall that each hydrofoil is located at $r_h^b(\alpha_s)$ (see Eq. (2-19) and Eq. (2-20)) with respect to the CG of the craft. Thus the position of the craft relative to the NED frame becomes:

$$p_{nh}^n(\eta, \alpha_s) = \begin{bmatrix} x_n^h \\ y_n^h \\ z_n^h \end{bmatrix} = p_{nb}^n + R_b^n(\Theta_{nb})r_h^b(\alpha_s) \quad (2-22)$$

where $R_b^n(\Theta_{nb})$ is the linear velocity transformation matrix defined in Eq. (2-2). Therefore, the variables x_w and z_w of the velocity components of the regular wave in Eq. (2-14) are replaced by x_n^h and z_n^h respectively. Recall that the reduced-order model in 3 DOF includes

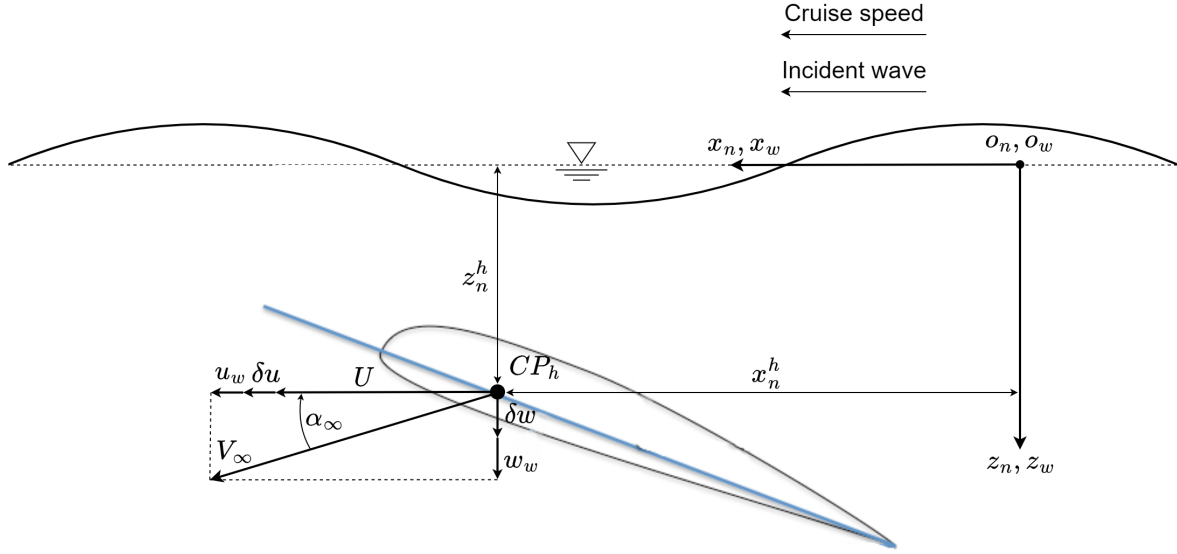


Figure 2-11: Change of inflow velocity due to different motions of the hydrofoil in the presence of incidence waves

only the heave, roll and pitch motions. Therefore, the NED positions x_n and y_n (included in vector p_{nb}^n), and the yaw angle ψ (included in vector Θ_{nb}) that are included in Eq. (2-22), are set to zero.

The components of the velocity perturbations at CP_h of the hydrofoil due to the craft motions, δu and δw in x_h and z_h axes respectively are defined as ([40], [5], [25]):

$$\delta u(\dot{\theta}, \alpha_s) = l_z(\alpha_s)\dot{\theta} \quad (2-23a)$$

$$\delta w(\dot{z}_n, \dot{\theta}, \dot{\phi}, \alpha_s) = \dot{z}_n + l_y\dot{\phi} - l_x(\alpha_s)\dot{\theta} \quad (2-23b)$$

The angle α_∞ is defined as the angle between the inflow velocity V_∞ and the horizontal axis x_n that is parallel to the mean free water surface. Finally, the equations for α_∞ and the V_∞ are given by ([40], [5], [25], [22]):

$$\alpha_\infty(\dot{z}_n, \dot{\theta}, \dot{\phi}, \alpha_s, u_w, w_w) = \tan^{-1} \left(\frac{\delta w + w_w}{U + \delta u + u_w} \right) \quad (2-24)$$

$$V_\infty(\dot{z}_n, \dot{\theta}, \dot{\phi}, \alpha_s, u_w, w_w) = \sqrt{(U + \delta u + u_w)^2 + (\delta w + w_w)^2} \quad (2-25)$$

where δu and δw are obtained from Eq. (2-23) and U is obtained from Eq. (2-21).

In Figure 2-12, one can see a 2D sketch illustrating the motion of a hydrofoil craft, such as HEARP, that moves in the x - z plane with constant cruise speed U .

Finally, the equations for α_r and α_e are functions of the motions of the craft, and the swinging angle α_s and they are given by:

$$\alpha_r(\theta, \dot{z}_n, \dot{\theta}, \dot{\phi}, \alpha_s, u_w, w_w) = \theta + \alpha_\infty \quad (2-26a)$$

$$\alpha_e(\theta, \dot{z}_n, \dot{\theta}, \dot{\phi}, \alpha_s, u_w, w_w) = \alpha_s + \alpha_r \quad (2-26b)$$

where α_∞ and α_s are obtained from Eq. (2-24) and Eq. (2-15) respectively.

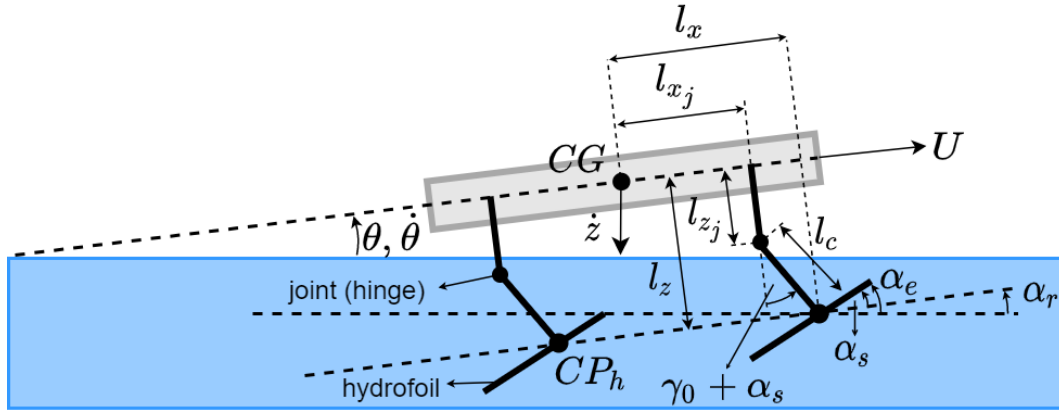


Figure 2-12: Motion of a hydrofoil craft in calm water

Based on the hydrodynamic theory and all the analyses mentioned above, the lift and drag forces of hydrofoil are defined by:

$$F_L(z_n, \dot{\theta}, \dot{\phi}, \alpha_s, u_w, w_w) = \frac{1}{2} \rho V_\infty^2 A_h C_L(\alpha_e) \quad (2-27a)$$

$$F_D(z_n, \dot{\theta}, \dot{\phi}, \alpha_s, u_w, w_w) = \frac{1}{2} \rho V_\infty^2 A_h C_D(\alpha_e) \quad (2-27b)$$

where ρ is the fluid density, A_h is the projected hydrofoil area and C_L , and C_D are the lift and drag coefficients, respectively [5]. The projected area of hydrofoil is calculated using a CAD model because, in general, it does not have a simple rectangular shape but some more complicated shape, such as in Figure 1-6a and Figure 2-6.

2-8-4 Lift and Drag coefficients

In general, the coefficients $C_L(\alpha_e)$ and $C_D(\alpha_e)$ are nonlinear functions of the effective angle of attack. Regarding the lift coefficient, when the α_e is small, the lift is linearly dependent on α_e . If the foil has a non-zero camber (see Figure 2-6), the lift is non-zero when $\alpha_e = 0$. On the other hand, if the camber is zero, the foil is considered symmetrical, and the lift equals zero when $\alpha_e = 0$. For small angles of attack, the flow over the hydrofoil remains laminar and attached. Under these conditions, the lift and drag coefficients are modelled with acceptable accuracy using linear approximations [5].

However, for large values of α_e , cavitation and ventilation occur, depending on speed and submergence. The cavitation occurs when the pressure on the upper side (suction side) of the foil equals the vapour pressure. Hence, when a large part of the suction side of the foil is cavitating, the lift force is distinctly reduced in relation to a non-cavitating foil at the same speed. Moreover, also as a consequence of cavitation, ventilation may arise. Ventilation means that there is a connection or an air tunnel between the air and the foil surface. Thus, the presence of ventilation leads to a significant drop in the lifting capacity of a foil. This phenomenon should also concern control during manoeuvring because it would cause ventilation along fore struts, which may ventilate the forward foil system and cause loss of the lift force. Figure 2-13 schematically shows how the steady lift force depends on the

angle of attack α and flap angle δ . More precisely, for small α and δ , the lift force is linearly dependent on these angles. Conversely, cavitation and ventilation occur for larger angles, leading to a substantial decrease in lift force as a consequence of these phenomena [12].

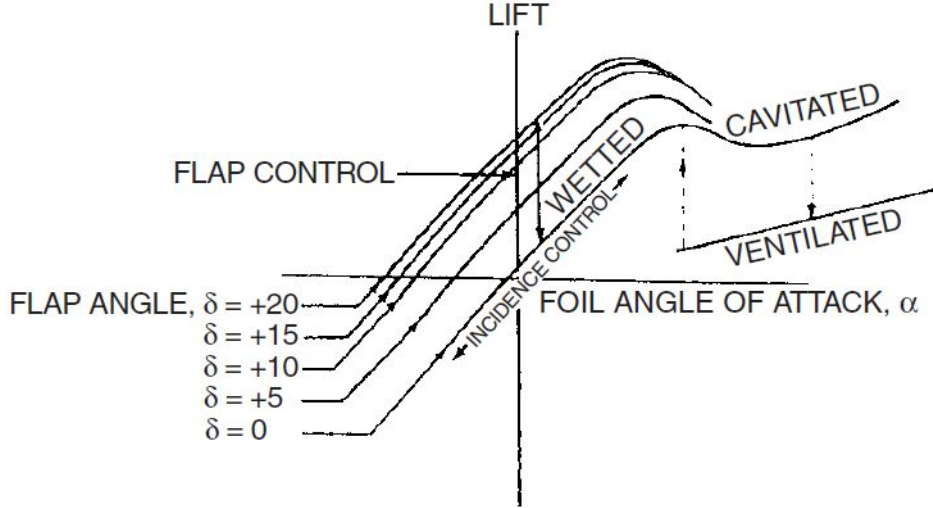


Figure 2-13: Foil lift curves [12]

The developed dynamical model of this thesis uses linear approximations of the lift and drag coefficients, which are obtained from the study of [5]. Regarding the lift coefficient, it is linearized by a first-order Taylor series approximation which is defined as:

$$C_L(\alpha_e) \approx C_{L_0} + C_{L_\alpha} \alpha_e \quad (2-28)$$

where the coefficient C_{L_0} is the value of the C_L when $\alpha_e = 0$ ($C_{L_0} = 0$ for symmetrical foils) and C_{L_α} is the slope of the linear approximation defined as $C_{L_\alpha} = \frac{dC_L}{d\alpha_e}$. This linear approximation is usually valid for angles within the range of $\alpha_e = \pm 15$ deg.

The slope of the linear lift coefficient is reasonably approximated by:

$$C_{L_\alpha} = \frac{\pi AR}{1 + \sqrt{1 + (AR/2)^2}}$$

The drag coefficient C_D consists of two parts: induced drag and parasitic drag. The parasitic drag is roughly constant and is denoted by C_{D_p} . It is generated by the shear stress of fluid moving over the wing and other effects. The induced drag is proportional to the square of the lift force for small angles of attack. Combining these two types of drag, we have:

$$C_D(\alpha_e) = C_{D_p} + \frac{(C_{L_0} + C_{L_\alpha} \alpha_e)^2}{\pi e AR}$$

where parameter e is the Oswald efficiency factor, which ranges between 0.8 and 1.0.

By using a first-order Taylor series approximation of C_D about a nominal operating condition $\alpha_e = \alpha_e^*$, we can express linear approximation for the drag coefficient as:

$$C_D(\alpha_e) \approx C_{D_0} + C_{D_\alpha} \alpha_e, \quad \forall \alpha_e \approx \alpha_e^* \quad (2-29)$$

where the coefficient C_{D_0} is the value of the C_D when $\alpha_e = 0$ and C_{D_α} is the slope of the linear approximation defined as $C_{D_\alpha} = \frac{dC_D}{d\alpha_e}$.

The aforementioned linear approximations for lift and drag coefficients are illustrated by Figure 2-14. Note that the α angle in Figure 2-14, corresponds to α_e . Thus, these approximations are applied to the HEARP system by the assumption that the operation range of attack angles for the hydrofoils is limited to small angles.

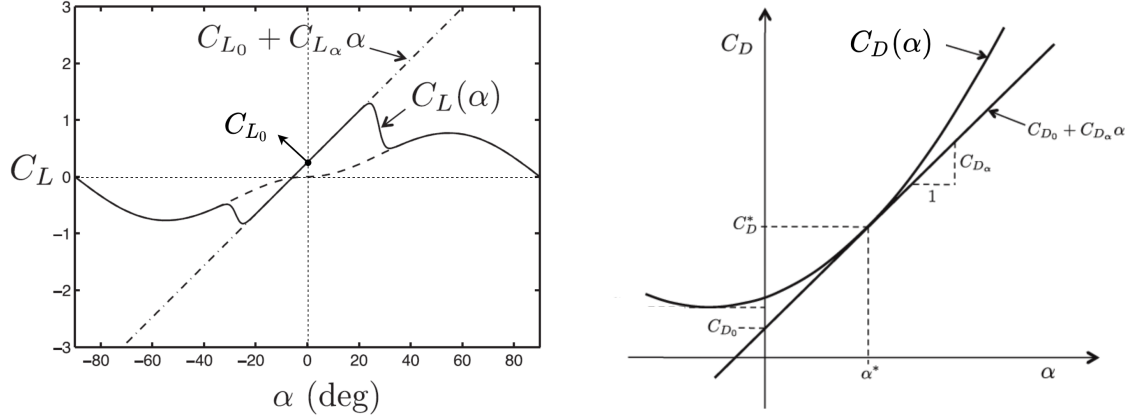


Figure 2-14: Linear approximations for the lift and drag coefficients [5]

Finally, using the linear approximations for the lift and drag coefficients of Eq. (2-28) and Eq. (2-29) respectively, the formulas for the corresponding hydrodynamic forces of Eq. (2-27) are now reformulated to:

$$F_L(\dot{z}_n, \dot{\theta}, \dot{\phi}, \alpha_s, u_w, w_w) = \frac{1}{2} \rho V_\infty^2 A_h (C_{L_0} + C_{L_\alpha} \alpha_e) \quad (2-30a)$$

$$F_D(\dot{z}_n, \dot{\theta}, \dot{\phi}, \alpha_s, u_w, w_w) = \frac{1}{2} \rho V_\infty^2 A_h (C_{D_0} + C_{D_\alpha} \alpha_e) \quad (2-30b)$$

Note that the lift and drag coefficients are the same for all hydrofoils because they all have the same design.

2-8-5 Hydrodynamic Force and Moment vector

Recall that side-way drag forces in the y_h direction of the hydrofoil are neglected in this study. Additionally the lifting component F_L is perpendicular to relative water flow direction (negative z_h -axis), and the drag component F_D is parallel to the water flow direction (negative x_h -axis). Hence, in vector notation, the forces acting on a hydrofoil are conveniently defined as $f_h = [-F_D, 0, -F_L]^T$. In order to express these forces in the BODY reference frame, a principal rotation of the Euler angle around the y_h -axis (see Eq. (2-4)) is used. In this way, the water flow direction is rotated by an angle α_r such that the resulting x_h -axis is parallel to the x -axis of BODY frame. Note that the angle ϕ is assumed to be negligible, so we do not use rotation about the x_h -axis. This transformation is described by the following expression with the use of the relative angle of attack α_r :

$$f_h^b = R_{y_h, \alpha_r}^T f_h \implies \begin{bmatrix} F_x \\ F_y \\ F_z \end{bmatrix} = \begin{bmatrix} \cos(\alpha_r) & 0 & -\sin(\alpha_r) \\ 0 & 0 & 0 \\ \sin(\alpha_r) & 0 & \cos(\alpha_r) \end{bmatrix} \begin{bmatrix} -F_D \\ 0 \\ -F_L \end{bmatrix} \quad (2-31)$$

where f_h^b denotes the force vector with a line of action through CP_h (centre of pressure of the hydrofoil) expressed in $\{b\}$ [14].

Subsequently, because the local coordinate frame $\{h\}$ of each hydrofoil is located at r_h^b (see Eq. (2-19)) relative to CO (which coincides with CG), the vector f_h^b creates moments as well. Therefore, the vector of the hydrodynamic forces and moments that act on each hydrofoil i is defined by:

$$\tau_i(\eta, \nu, u_{in}, d_w) = \begin{bmatrix} f_{h,i}^b \\ r_{h,i}^b \times f_{h,i}^b \end{bmatrix} = \begin{bmatrix} F_x^i \\ F_y^i \\ F_z^i \\ F_z^i l_y^i - F_y^i l_z^i \\ F_x^i l_z^i - F_z^i l_x^i \\ F_y^i l_x^i - F_x^i l_y^i \end{bmatrix} \quad (2-32)$$

where $r_{h,i}^b$ and $f_{h,i}^b$ are defined for each hydrofoil as in Eq. (2-19) and Eq. (2-31) respectively [14]. We denote $i = \{f, ap, as\}$, and where f , ap and as refers to fore, aft port and aft starboard hydrofoils respectively. Note here that the vector τ_i is a function of the positions η , the velocities ν , the control inputs u_{in} (see Eq. (2-34a)) and the wave disturbances d_w (see Eq. (2-35)). All the equations presented in this section are used to construct each τ_i vector.

As already discussed, these forces depend on the motions of each hydrofoil, the swinging angle controlled by the servo motors (see Section 2-8-2), but also include additional angles that originate from the wave disturbances. The part of the hydrodynamic forces that depend on the velocities ν is considered as damping force, while the part that depends on the positions η is considered as restoring force. The part of these forces which is controlled by the actuators is considered as the control input. Moreover, the last part of the forces that originate from the wave velocity components is called wave excitation forces (disturbances). Because of the nonlinearities of the vector τ_i , it is impossible to decompose the forces into these four different parts. However, this decomposition is achieved by the linearization around the operating point of the hydrofoil craft, which is introduced later in Chapter 3.

2-9 Motion Equations for HEARP

2-9-1 Assumptions

Recall that this chapter aims to develop a reduced-order nonlinear dynamical model in 3 DOF (heave, roll and pitch) for the HEARP system. Therefore, using all the presented material in this chapter, the nonlinear 3 DOF dynamical model for HEARP is derived in this section. To do so, the following assumptions are made:

- HEARP is considered a rigid body with constant mass, so any possible oscillations of the different parts of the craft are neglected.
- Effects of rotating masses such as the rudder, the hydrofoils and the propeller are neglected.
- The origin of the body-fixed reference frame CO coincides with the CG ($r_g^b = [0, 0, 0]^T$).
- Buoyancy forces are considered negligible.

- Forces and moments due to added mass and hydrodynamic Coriolis-centripetal forces are neglected.
- The hydrodynamic damping of the hydrofoil craft is modelled only by drag and lift forces acting on the hydrofoils. Thus, any other effects such as potential damping, skin friction, wave drift damping and damping due to vortex shedding are neglected.
- The hydrodynamic forces acting on the hydrofoils' struts, the rudder and the propeller, and the side-way drag forces in y_h of the hydrofoil are neglected. Furthermore, the effect of the roll angle on the lift and drag forces is also neglected.
- With the use of 2 SISO feedback controllers for the rudder and the propeller, respectively, the velocities of the surge, sway and yaw motions of the hydrofoil craft are regulated to $u = U_0$, $v = 0$ and $r = 0$. Where U_0 is the constant cruise speed used for the simulations and the experiments.
- The interaction between the waves and the craft is modelled by the wave-induced local velocity of the water surrounding the hydrofoils.
- Variations of the inflow velocity due to interactions between the different components of the craft, such as the fore and aft hydrofoils, are not modelled.
- All the states of the system are estimated by the EKF algorithm, which is used by the PX4 software (see Section 1-2).
- The presence of surface effects, cavitation and ventilation, is neglected.

2-9-2 Reduced-order Nonlinear Dynamical Model with 3 DOF

Consider the already presented modelling of different parts of Eq. (2-1) in the previous sections and the assumptions mentioned above. Hence, the reduced-order nonlinear dynamical model for HEARP with 3 DOF in a vectorial setting is described by:

$$M_{RB_3}\dot{\nu}_3 + C_{RB_3}(\nu_3)\nu_3 + g_3(\eta_3) = \tau_{f_3}(\eta_3, \nu_3, u_{in}, d_w) + \tau_{ap_3}(\eta_3, \nu_3, u_{in}, d_w) + \tau_{as_3}(\eta_3, \nu_3, u_{in}, d_w) \quad (2-33)$$

where $\eta_3 = [z_n, \phi, \theta]^T$ is the reduced vector of positions and angles expressed in NED reference frame and $\nu_3 = [w, p, q]^T$ is the reduced vector of linear and angular velocities expressed in BODY reference frame.

As we only take into account the control inputs arising from the three hydrofoils, the vector of actual control input u_{in} and the vector of commanded control input u_c (see (2-17)) are defined as:

$$u_{in}(t) = [\delta_s^f(t), \delta_s^{ap}(t), \delta_s^{as}(t)]^T \quad (2-34a)$$

$$u_c(t) = [\delta_{s,c}^f(t), \delta_{s,c}^{ap}(t), \delta_{s,c}^{as}(t)]^T \quad (2-34b)$$

where δ_s^i and $\delta_{s,c}^i$ denote the actual and the commanded angles of servo motors, respectively, for fore, aft port and aft starboard hydrofoils. It should be mentioned that the dynamics of the actuators are not included in the reduced-order dynamical model, but they are incorporated in the control design in Chapter 4 via a block diagram formulation. Therefore the input vector of Eq. (2-33) is the u_{in} , while the u_c is used as input vector to an individual model that captures the dynamics of the actuators (see Eq. (4-4)). Note that the angles of servo motors are functions of time; however, to simplify notation, the (t) is omitted later on.

The vector d_w consists of the velocity components of water particles due to incident waves in x_w and z_w axes for each hydrofoil. Recall that depending on the location of each hydrofoil

with respect to CG and the motions of the craft, the velocity components for each hydrofoil are different (see Eq. (2-22)). Thus, the vector d_w is finally defined by:

$$d_w(t, \eta_3, u_{in}) = \begin{bmatrix} u_w^f(t, x_n^f, z_n^f) \\ w_w^f(t, x_n^f, z_n^f) \\ u_w^{ap}(t, x_n^{ap}, z_n^{ap}) \\ w_w^{ap}(t, x_n^{ap}, z_n^{ap}) \\ u_w^{as}(t, x_n^{as}, z_n^{as}) \\ w_w^{as}(t, x_n^{as}, z_n^{as}) \end{bmatrix} \quad (2-35)$$

where the equations for each velocity component are given by Eq. (2-14), while the equations for the instantaneous location of each hydrofoil are given by Eq. (2-22). Recall that in Eq. (2-22), the variables x_n , y_n and ψ are set to zero because they are not part of the reduced-order model. Additionally, note that the vector d_w is a function time t , the positions and angles η_3 and the control inputs u_{in} .

Recall that using the SISO controllers for the rudder and propeller, the velocities of the surge, sway and yaw are regulated to $u = U_0$, $v = 0$ and $r = 0$. This assumption is expressed in mathematical terms by the vector $\bar{\nu} = [U_0, 0, w, p, q, 0]$, which is used for the derivation of the reduced-order matrices of the system. Note here that the velocities of heave, roll and pitch motions remain states of the dynamical model. Therefore, these values are filled in all the matrices of Eq. (2-33) to obtain the reduced-order matrices. Each of the reduced-order matrices and vectors of Eq. (2-33) is obtained by selecting the lines corresponding to heave, roll and pitch motions from the corresponding 6 DOF matrices. This is achieved by using a selection matrix which is chosen as:

$$L = \begin{bmatrix} 0 & 0 & 1 & 0 & 0 & 0 \\ 0 & 0 & 0 & 1 & 0 & 0 \\ 0 & 0 & 0 & 0 & 1 & 0 \end{bmatrix} \quad (2-36)$$

which satisfies $\nu_3 = [w, p, q]^T = L\nu$.

Subsequently, with the use of the matrix L (see Eq. (2-36)) and the 6 DOF matrices (see Eq. (2-6), Eq. (2-7), Eq. (2-8) and Eq. (2-32)) we can obtain the reduced order matrices and vectors of Eq. (2-33) as follows:

$$M_{RB_3} = LM_{RB}L^T = \begin{bmatrix} m & 0 & 0 \\ 0 & I_x & -I_{xy} \\ 0 & -I_{yx} & I_y \end{bmatrix} = \begin{bmatrix} m & 0 & 0 \\ 0 & I_x & -I_{xy} \\ 0 & -I_{xy} & I_y \end{bmatrix} \quad (2-37a)$$

$$C_{RB_3}(\nu_3)\nu_3 = LC_{RB}(\bar{\nu})\bar{\nu} = \begin{bmatrix} -mU_0q \\ -q(I_{xz}p + I_{yz}q) \\ p(I_{xz}p + I_{yz}q) \end{bmatrix} \quad (2-37b)$$

$$g_3(\eta_3) = Lg(\eta) = \begin{bmatrix} -mg \cos(\phi) \cos(\theta) \\ 0 \\ 0 \end{bmatrix} \quad (2-37c)$$

$$\begin{aligned} \tau_{i_3}(\eta_3, \nu_3, u_{in}, d_w) &= L\tau_i(\eta, \nu, u_{in}, d_w) \\ &= \begin{bmatrix} -(F_D^i \sin(\alpha_r^i) + F_L^i \cos(\alpha_r^i)) \\ -(F_D^i \sin(\alpha_r^i) + F_L^i \cos(\alpha_r^i))l_y^i \\ (F_D^i \sin(\alpha_r^i) + F_L^i \cos(\alpha_r^i))l_x^i - (F_D^i \cos(\alpha_r^i) - F_L^i \sin(\alpha_r^i))l_z^i \end{bmatrix} \end{aligned} \quad (2-37d)$$

where $i = \{f, ap, as\}$ corresponds to each of the hydrofoils. The equations for α_r^i , F_L^i and F_D^i are defined by Eq. (2-26a) and Eq. (2-30) respectively, with the only difference that here we define $U = U_0$. Note that $I_{xy} = I_{yx}$ as it is shown in Eq. (2-37a).

Linear State-Space Model

Control theory for linear systems is well developed. Practical experience confirms that commonly linear controllers that are designed using linear methods can provide satisfactory performance when applied to real nonlinear plants [44]. Therefore, we approximate the nonlinear system of HEARP by a linear system to use control design methods for linear systems. In this chapter, initially, the nonlinear state-space model is introduced, which is a modified version of the nonlinear EOM for the HEARP that was presented in Chapter 2. Next, the procedure to linearize the nonlinear model is presented and the resulting equations for the linear state-space model are given. Finally, the nominal values and the uncertainties of all the parameters of the system are defined.

3-1 Fundamental Properties of Linear Systems

One of the most important properties of linear systems is that they satisfy the superposition principle. To explain this property, let us consider the next example. Let $f(u)$ be a linear operator, let u_1 and u_2 be two independent variables (for example, input signals), and let α_1 and α_2 be two real scalars, then:

$$f(\alpha_1 \cdot u_1 + \alpha_2 \cdot u_2) = \alpha_1 \cdot f(u_1) + \alpha_2 \cdot f(u_2) \quad (3-1)$$

Thus, any linear system satisfies the property of Eq. (3-1), and it is described by linear ordinary differential equations with constant coefficients and which do not require differentiation of the inputs (independent variables) [44].

In practice, many electromechanical systems, such as the HEARP, involve nonlinear equations. However, as long as the system operates around the equilibrium point, it is possible to approximate the nonlinear system by a linear system. Such a linear system exhibits the same characteristics as the real nonlinear system when the latter operates within a limited range [38].

Time invariance is a fundamental concept used to describe systems whose properties do not change with time. In particular, for a time-invariant system if the input $u(t)$ gives output

$y(t)$, then if we shift the time at which the input is applied by a constant amount τ , $u(t + \tau)$ gives the output $y(t + \tau)$. Systems that are linear and time-invariant are often defined as linear time-invariant (LTI) systems. This class of systems has the interesting property that their response to an arbitrary input is completely characterized by their response to step inputs or short "impulses" [3].

3-2 Nonlinear State-Space Model

In control theory, a convenient form for describing dynamical systems' input/output behaviour is the so-called state-space representation. The state of a system is a collection of variables that summarize the past motion of a system for the purpose of predicting the future motion. For a system such as a hydrofoil craft, the state is the set of its positions and velocities. The development of state space models involves the modification of the dynamical models to include external actuators and sensors[3].

The HEARP system consists of n states ($x \in \mathbb{R}^n$), m inputs ($u_{in} \in \mathbb{R}^m$), l outputs ($y \in \mathbb{R}^l$) and p disturbances ($d_w \in \mathbb{R}^p$). Depending on the number of inputs and outputs of the dynamical system, usually, we can categorize them as single-input single-output (SISO) and multi-input multi-output (MIMO). To describe the dynamics of a physical system such as HEARP, the nonlinear state-space model of the following form can be used:

$$\dot{x}(t) = f(x(t), u_{in}(t), d_w(t)) \quad (3-2a)$$

$$y(t) = g(x(t)) \quad (3-2b)$$

where $f : \mathbb{R}^n \times \mathbb{R}^m \times \mathbb{R}^p \rightarrow \mathbb{R}^n$ and $g : \mathbb{R}^n \rightarrow \mathbb{R}^l$ are nonlinear smooth (continuously differentiable) mappings [3].

The dimension n of the state vector x is called the order of the model. The model given in Eq. (3-2) is called time-invariant because the functions f and g do not depend explicitly on time t . The model consists of two functions: the function f gives the rate of change of the state vector as a function of state x , control u_{in} and disturbance d_w , and the function g gives the measured outputs as functions of state x [3].

Assuming that all the states of the HEARP are estimated by the EKF algorithm that is provided by PX4 software, the dynamics of the measured signals are defined as:

$$y = g(x) \implies y = [\hat{z}_n, \hat{\phi}, \hat{\theta}]^T = [z_n, \phi, \theta]^T \quad (3-3)$$

where y denotes a vector of the estimated states obtained by the EKF algorithm.

The vector of wave disturbances d_w (see Eq. (2-35)) depends on the states and the outputs of the system. However, in order to simplify the coding for the simulations, it is decided to use a linear approximation of the position for the CP of each hydrofoil (submergence and distance from CG), depending on the chosen operating conditions. Considering this motivation and for the sake of notation, it is assumed that the vector d_w that lies in the nonlinear state-space of the HEARP is only a function of time.

Finally, after the reformulation of the nonlinear EOM of the reduced-order model in 3 DOF of Eq. (2-33) and Eq. (3-3), the nonlinear state space form for HEARP dynamics is given by:

$$\dot{x} = f(x, u_{in}, d_w) = \begin{bmatrix} \dot{z}_n \\ \dot{\phi} \\ \dot{\theta} \\ (M_{RB_3})^{-1} \left(-C_{RB_3}(x)x - g_3(x) + \tau_{h_3}(x, u_{in}, d_w) \right) \end{bmatrix} \quad (3-4a)$$

$$y = g(x) = \begin{bmatrix} z_n \\ \phi \\ \theta \end{bmatrix} \quad (3-4b)$$

where

$x = [z_n, \phi, \theta, \dot{z}_n, \dot{\phi}, \dot{\theta}]^T$: State vector

$u_{in} = [\delta_s^f, \delta_s^{ap}, \delta_s^{as}]^T$: Input vector

$y = [z_n, \phi, \theta]^T$: Output vector

$d_w = [u_w^f, w_w^f, u_w^{ap}, w_w^{ap}, u_w^{as}, w_w^{as}]^T$: Disturbance vector

$\tau_{h_3}(x, u_{in}, d_w) = \tau_{f_3}(x, u_{in}, d_w) + \tau_{ap_3}(x, u_{in}, d_w) + \tau_{as_3}(x, u_{in}, d_w)$: Hydrodynamic forces and moments

3-3 Derivation of the Linearized State-Space Model

As it was presented in Chapter 2, the derived reduced-order dynamical model for HEARP (see Eq. (2-33)) is highly nonlinear. Thus, a linear state-space model is derived from the linearization of the nonlinear state-space model in Eq. (3-4).

To explain the linearization methodology, consider a nonlinear state-space given by Eq. (3-2). The first step is the determination of the steady-state operating points x^* and u_{in}^* (equilibrium points), which are used for the linearization. Note that in steady-state conditions, the disturbance is assumed to be equal to zero, i.e. $d_w^* = 0$. A point $x^* \in \mathbb{R}^n$ is called an equilibrium point if there exists a specific $u_{in}^* \in \mathbb{R}^m$ (called the equilibrium input) such that:

$$f(x^*, u_{in}^*, d_w^*) = 0 \quad (3-5)$$

To give a more intuitive explanation of this notion, suppose that x^* is an equilibrium point (with equilibrium input u_{in}^*). Consider starting the system Eq. (3-2a) from initial condition $x(t_0) = x^*$, and applying the input $u_{in}(t) = u_{in}^*$ for all $t \geq t_0$. The resulting solution satisfies $x(t) = x^*$ for all $t \geq t_0$. That is why it is called an equilibrium point [39].

The derivation of the linear state-space model is based on the expansion of the nonlinear state-space model into Taylor series about the operating point and the retention of only the linear terms. Because we neglect higher-order terms of the Taylor series expansion, these neglected terms have to be small enough. In other words, the variables must deviate only slightly from the operating condition, otherwise the model will be inaccurate [38]. To eliminate the terms involving only steady-state quantities, we introduce the deviation variables:

$$\delta x(t) = x(t) - x^*, \quad \delta u_{in}(t) = u_{in}(t) - u_{in}^*, \quad \delta y(t) = y(t) - y^*, \quad \delta d_w(t) = d_w(t) - d_w^* \quad (3-6)$$

where $*$ represents the steady-state operating point or trajectory along which we perform the linearization [44]. The equilibrium output is defined by the equation $y^* = g(x^*)$.

3-3-1 Equilibrium Conditions

We can take inspiration from aircraft dynamics to determine the equilibrium conditions for a hydrofoil craft. An aircraft performs a level steady flight when it flies with constant cruise speed and along a level trajectory (parallel to the surface of the Earth). During a level steady flight, the Lift, Weight, Drag, and Thrust are in balance; thus, the aircraft is neither accelerating nor decelerating. Under these conditions the aircraft is in an equilibrium state which is defined as: the altitude $z_n = -h$ (constant height above Earth surface), the linear velocities u , v , w , the Euler angles ϕ , θ and ψ and the angular velocities p , q , and r are all constant. In the aerodynamics literature, an aircraft in equilibrium is said to be in trim. Generally, trim conditions may include states that are not constant. For example, in steady-climb flight, w is constant and z_n grows linearly [5].

Regarding the operation of a hydrofoil craft during the foilborne mode, the allowed variation of the vertical position is strictly limited by the length of the struts. Hence, the level steady flight with a straight line trajectory (constant heading) is defined as the equilibrium condition of the hydrofoil craft. It is worth noting that a steady-climb flight is only relevant during the take-off mode of the hydrofoil craft, which may last only a few seconds, thus it is not considered in this study. Using the chosen equilibrium condition of the hydrofoil craft, the equilibrium state is defined as:

- Linear velocities: $u^* = U_0$, $v^* = 0$ and $w^* = 0$
- Angular rates: $p^* = 0$, $q^* = 0$, and $r^* = 0$
- Euler angles: $\phi^* = 0$, $\theta^* = 0$ and $\psi^* = 0$
- Vertical NED position: $z_n^* = z_{n0}$ (above the mean free water surface)
- Wave disturbances: $d_w^* = O_6$ (vector of zeros)

Recall that it is assumed that with two SISO feedback controllers for the rudder and the propeller, the velocities of the surge, sway and yaw motions of the hydrofoil craft are regulated to $u = U_0$, $v = 0$ and $r = 0$.

When operating at the equilibrium state, the total lift force $\sum F_L^i$ originated from the three hydrofoils equal to the weight $W = mg$ of the hydrofoil craft. Moreover, the total moments $\sum K$ and $\sum M$ around roll and pitch angles respectively equal to zero. Thus, $\delta_s^i = \delta_s^{i*}$ is defined as the default angle of the servo motors for each of the hydrofoils, such that the aforementioned equilibrium conditions are satisfied.

Finally, the nonlinear state-space model of Eq. (3-4) is linearized around the equilibrium conditions, which are defined as:

$$x^* = [z_{n0}, 0, 0, 0, 0, 0]^T; \quad u_{in}^* = [\delta_s^{f*}, \delta_s^{ap*}, \delta_s^{as*}]^T; \quad d_w^* = O_6; \quad y^* = [z_{n0}, 0, 0]^T$$

3-3-2 Equations of the Linearized Model

The linearization of the nonlinear state-space model of HEARP (see Eq. (3-4)) is performed using Taylor series expansion and the deviation variables (see Eq. (3-6)). Hence, the linearized

state-space model is given by:

$$\frac{d\delta x(t)}{dt} = \underbrace{\frac{\partial f(x^*, u_{in}^*, d_w^*)}{\partial x}}_A \delta x(t) + \underbrace{\frac{\partial f(x^*, u_{in}^*, d_w^*)}{\partial u_{in}}}_{B} \delta u_{in}(t) + \underbrace{\frac{\partial f(x^*, u_{in}^*, d_w^*)}{\partial d_w}}_{B_d} \delta d_w(t) \quad (3-7a)$$

$$\delta y(t) = \underbrace{\frac{\partial g(x^*)}{\partial x}}_C \delta x(t) \quad (3-7b)$$

where $\frac{\partial f(x^*, u_{in}^*, d_w^*)}{\partial x}$ is the partial derivative of function $f(x, u_{in}, d_w)$ with respect to x evaluated at the equilibrium points x^* , u_{in}^* and d_w^* . A similar explanation can also be given to the other partial derivatives. The matrices A , B , B_d and C are the Jacobian matrices of the corresponding functions, which consist of real and constant coefficients. For the sake of conciseness the notation δ is omitted in the rest of the report.

Note that only the function f (derivative of the state vector) requires linearization because the g (output function) is already linear with respect to the state vector x . For the sake of simplicity and to avoid laborious analytical calculations of the Jacobian matrices by hand, the Symbolic Math Toolbox of Matlab is used [33]. In particular, all the equations of the system dynamics are defined with symbolic variables and using this toolbox, all the differentiations are defined computationally. The resulting equations for the matrices A , B , B_d and C and their corresponding numerical values are given in Appendix A.

3-4 Wave disturbance model

As mentioned in Section 3-2, it is decided to simulate the wave disturbance model of Eq. (2-35) by using the assumption that the craft operates sufficiently close to the equilibrium conditions. Therefore, the position of the CP for each hydrofoil expressed in the NED frame is approximated by evaluating the equilibrium conditions in the Eq. (2-22):

$$p_{n,i}^{n*}(x^*, u_{in}^*) = \begin{bmatrix} x_n^{i*} \\ y_n^{i*} \\ z_n^{i*} \end{bmatrix} = \begin{bmatrix} l_{x_j}^i + l_b \sin\left(\gamma_0 - \frac{l_s}{h_n} \delta_s^{i*}\right) \\ l_y^i \\ z_{n0} + l_{z_j}^i + l_b \cos\left(\gamma_0 - \frac{l_s}{h_n} \delta_s^{i*}\right) \end{bmatrix} \quad (3-8)$$

To clarify, the vector $p_{n,i}^n$ of Eq. (3-8) is the same with the vector p_{nh}^n of Eq. (2-22).

Finally, the simulation model for the wave velocity components of each hydrofoil that is used to calculate the time-dependend disturbance signal is given by the following set of equations:

$$d_w(t) = \begin{bmatrix} u_w^f(t) \\ w_w^f(t) \\ u_w^{ap}(t) \\ w_w^{ap}(t) \\ u_w^{as}(t) \\ w_w^{as}(t) \end{bmatrix} = \begin{bmatrix} -\frac{gk\zeta_0}{\omega} e^{-kz_n^{f*}} \sin(kx_n^{f*} - \omega_e t) \cos(\beta) \\ -\frac{gk\zeta_0}{\omega} e^{-kz_n^{f*}} \cos(kx_n^{f*} - \omega_e t) \\ -\frac{gk\zeta_0}{\omega} e^{-kz_n^{ap*}} \sin(kx_n^{ap*} - \omega_e t) \cos(\beta) \\ -\frac{gk\zeta_0}{\omega} e^{-kz_n^{ap*}} \cos(kx_n^{ap*} - \omega_e t) \\ -\frac{gk\zeta_0}{\omega} e^{-kz_n^{as*}} \sin(kx_n^{as*} - \omega_e t) \cos(\beta) \\ -\frac{gk\zeta_0}{\omega} e^{-kz_n^{as*}} \cos(kx_n^{as*} - \omega_e t) \end{bmatrix} \quad (3-9)$$

where the numerical values of the x_n^{i*} and z_n^{i*} are given in Table 3-1.

Table 3-1: Equilibrium position of the CP for each hydrofoil expressed in NED frame

Variable	Value (m)
x_n^{f*}	0.54
x_n^{ap*}	-0.16
x_n^{as*}	-0.14
z_n^{f*}	0.22
z_n^{ap*}	0.22
z_n^{as*}	0.21

3-5 Numerical values for system parameters

In this section, all the nominal parameters of the system are defined based on data provided by the Ship Hydromechanics Group of TU Delft, and the documentation for HEARP and the CAD model provided by Flying Fish [13]. It is a fact that the values of some parameters are estimated roughly but also some other parameters vary due to the surface effects, so they are considered uncertain. Therefore, the magnitude of potential deviation from the nominal value for each parameter is quantified approximately, and it is expressed either with a percentage % or with a range. With the use of these uncertain parameters, the perturbed plant (uncertain state-space model) is defined in Chapter 4 with the aim of designing a controller that is robust in the presence of the worst-case scenario uncertainties.

3-5-1 HEARP Mass Properties

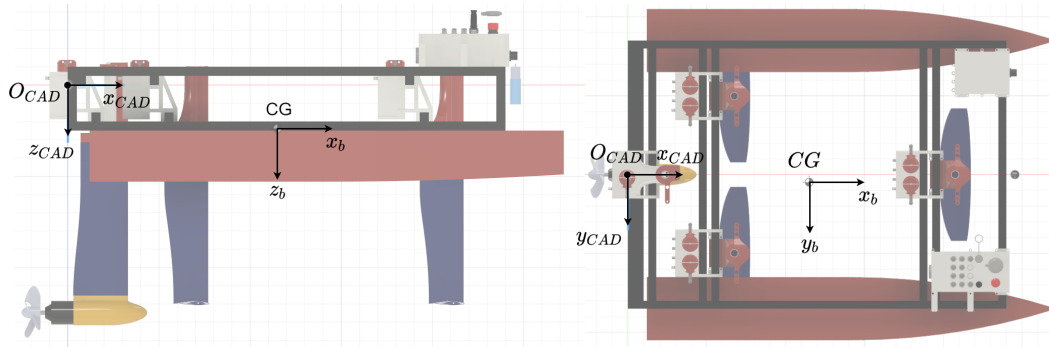
To obtain a rough estimation of the mass properties of HEARP, the documentation for HEARP and the CAD model of HEARP are used. The provided CAD model is designed in Autodesk Fusion 360. However, it is not accurate enough because the materials of the different parts are not appropriately defined, and some parts are not designed at all. In the documentation of HEARP, the actual masses of different sub-assemblies (such as enclosure boxes, T-foils, and frame) are given. Note that each sub-assembly consists of different parts with different materials. Therefore, to match the actual mass of the system with the mass of the CAD model, the density of each sub-assembly is approximated by a uniform density such that its mass in the CAD model matches its actual mass. To simplify this task, many small parts of the system are removed, such as bolts, nuts, rods, electrical devices, connectors, etc. Finally, after these modifications, the rough estimations for the nominal values for these parameters are obtained from Fusion 360, and they are reported in Table 3-2.

Due to these simplifications and approximations, the resulting mass properties are not completely accurate. Hence it is decided to assign a $\pm 10\%$ uncertainty to all the resulting parameters. For the mass, it is assigned an uncertainty of $\pm 5\%$ because the given mass is relatively accurate (see Table 3-2). Recall that the hydrodynamic added mass, which is considered a virtual mass added to a system, is neglected in the modelling of the HEARP. Thus, using these uncertainties, it can be stated that the added mass effect may be included indirectly in the perturbed plant dynamics. However, because of the lack of experimental data or accurate estimation of added mass coefficients by analytical or numerical methods, it is not possible to be sure about the aforementioned statement.

Table 3-2: Estimation of mass properties of HEARP from 360 Fusion

Parameter	Nominal Value	Uncertainty
m	29.38 kg	[-5%,5%]
I_x	3.77 kg m ²	[-10%,10%]
I_{xy}	-0.32 kg m ²	[-10%,10%]
I_y	7.60 kg m ²	[-10%,10%]
x_{CG}	0.58 m	[-10%,10%]
y_{CG}	0.02 m	[-10%,10%]
z_{CG}	0.12 m	[-10%,10%]

Note that in Table 3-2, x_{CG} , y_{CG} and z_{CG} denotes the location of the CG with respect to the origin of the CAD model O_{CAD} which is located at the back upper midpoint of the frame of HEARP. The location of CG and O_{CAD} are shown in the Figure 3-1.

**Figure 3-1:** Location of the origin of CAD model and the CG of system [13]

3-5-2 Operating conditions of HEARP

Considering the nominal operating conditions of HEARP during the tests of Flying Fish (see Table 1-1), it is decided to use the cruise speed of $U_0 = 4$ m/s for the linear state-space model. Currently, the cruise speed depends on the control skills of the operator, who regulate the speed of the propeller via remote control. Additionally, due to variations in the effective attack angles of hydrofoils during the operation of the craft, the drag forces also vary. This phenomenon affects the nominal cruise speed slightly. Therefore, it is decided to assign an uncertainty of $\pm 10\%$ for the nominal cruise speed.

The nominal submergence of the hydrofoils (see Table 1-1) depends on the length of the struts. Hence, the submergence of the hydrofoils must be small enough to ensure that during the foilborne mode, the hulls are not touching the free surface of the water. On the other hand, the hydrofoils should be sufficiently submerged such that they are not very close to the surface of the water to avoid sudden reduction of lift forces due to free-surface effects. Depending on the estimated location of CG (see Table 3-2) and the nominal submergence of the hydrofoils (see Table 1-1), the equilibrium vertical position of CG is calculated at around $z_{n0} = -0.25$ m. The parameters mentioned above of the steady-state condition of HEARP,

as well as the environmental conditions (g and ρ), are reported in Table 3-3.

Table 3-3: Steady-state conditions for the foilborne operation of HEARP and environmental conditions

Parameter	Nominal Value	Deviation from Nominal Value
U_0	4 m/s	[-10%,10%]
z_{n0}	-0.25 m	-
g	9.81 m/s ²	-
ρ (for 15°C, [45])	999.1 kg/m ³	-

3-5-3 Hydrofoils Parameters

Table 3-4 summarizes the design specifications of the hydrofoils of the HEARP.

Table 3-4: Design specifications of hydrofoils

Description	Value
c (Mean chord)	0.0805 m
s (Span)	0.40 m
A_h (Projected area)	0.0322 m ²
AR (Aspect Ratio)	5
Section profile	NACA 0012

To determine the lift and drag coefficients, the Ship Hydromechanics Group of TU Delft have performed various experiments validated by theoretical calculations. These experiments were done at the nominal hydrofoil submergence of 0.2 m, and their resulting data are used in this study to obtain the nominal values of lift and drag coefficients. The resulting diagrams for C_L and C_D as a function of the angle of attack are shown in Figure 3-2.

From Figure 3-2, it is observed that the lift and drag coefficients have the expected shape based on the Figure 2-14. That is, the C_L and C_D are nonlinear functions of the effective angle of attack α_e , which are approximated by linear functions for a small region around the operation point (see Eq. (2-30)). Based on experiments and the documentation of Flying Fish, for a cruise speed between 3 – 6 m/s, the hydrofoils of HEARP are expected to operate within the range of $-5^\circ \leq \alpha_e \leq 10^\circ$. Therefore, with the use of the Matlab function `polyfit()` [33], we perform a polynomial curve fitting on the nonlinear functions for the determination of the best fit for linear functions (in a least-squares sense). For the C_L it is used the range $-10^\circ \leq \alpha_e \leq 10^\circ$ while for the C_D it is used the range $-5^\circ \leq \alpha_e \leq 10^\circ$. The linear approximations of these coefficients are illustrated in Figure 3-2, and their corresponding values are reported in Table 3-5. Note that the values of these coefficients are calculated for angles expressed in radians.

As it is shown in Figure 3-2, the accuracy of the linear approximation for C_L is very high for the whole range of $-10^\circ \leq \alpha_e \leq 10^\circ$. Conversely, the C_D is approximated with lower accuracy, especially for $\alpha_e \leq 0$, because of the quadratic shape of the nonlinear function.

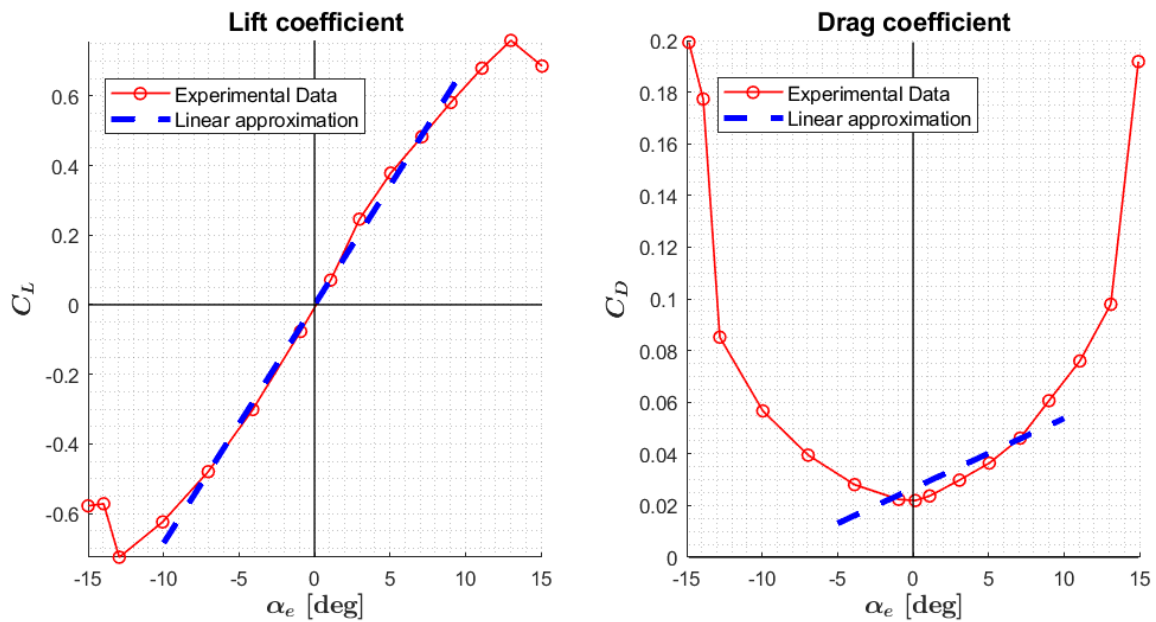


Figure 3-2: Lift and drag coefficients as a function of angle of attack based on experimental data from Ship Hydromechanics Group of TU Delft

In order to quantify the percentage error of the linear approximation for C_D , the following equation is used:

$$\text{Error} = \frac{C_{D,nl} - C_{D,l}}{C_{D,nl}} \cdot 100$$

where $C_{D,nl}$ denotes the actual value of the nonlinear coefficient, while $C_{D,l}$ denotes the linear approximation.

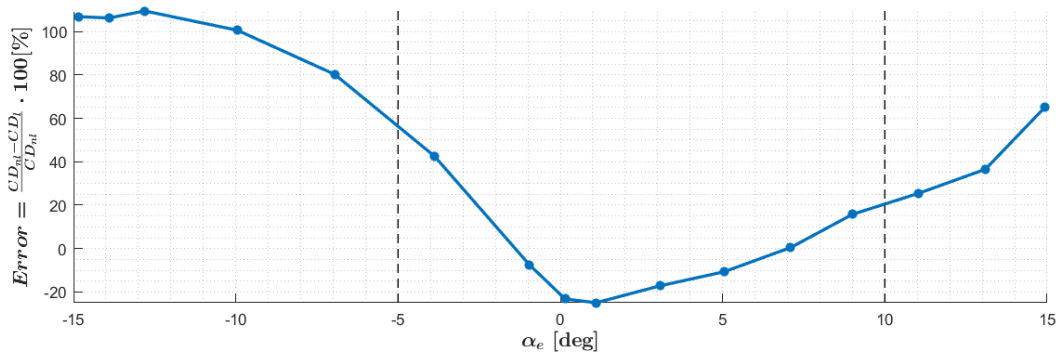


Figure 3-3: Error of linear approximation for drag coefficient C_D as function of effective angle of attack α_e

As it is shown in Figure 3-3, within the operation range of hydrofoils ($-5^\circ \leq \alpha_e \leq 10^\circ$) the error of the linear approximation of C_D varies approximately between $[-20\%, 50\%]$. This range of deviations from the nominal value of the linear approximation is used as uncertainty for the C_D coefficient.

When a hydrofoil operates in proximity to a free surface of the water, the lift and drag forces differ from the case of infinite submergence. Based on the study of [8], the effect of surface proximity is primarily a function of submergence depth to chord ratio, and for depths greater than two chords, the effect is negligible. More precisely, the lift force reduces as the hydrofoil approaches the free surface. Let us denote C_L , the lift coefficient that varies with the submergence depth, while $C_{L,\infty}$ denote the lift coefficient for an infinite submergence depth. Hence, the Lift Reduction Factor ($LRF = C_L/C_{L,\infty}$) versus submergence depth to chord ratio for different AR, based on different theories is shown in Figure 3-4. These theories are validated with experimental results in [8].

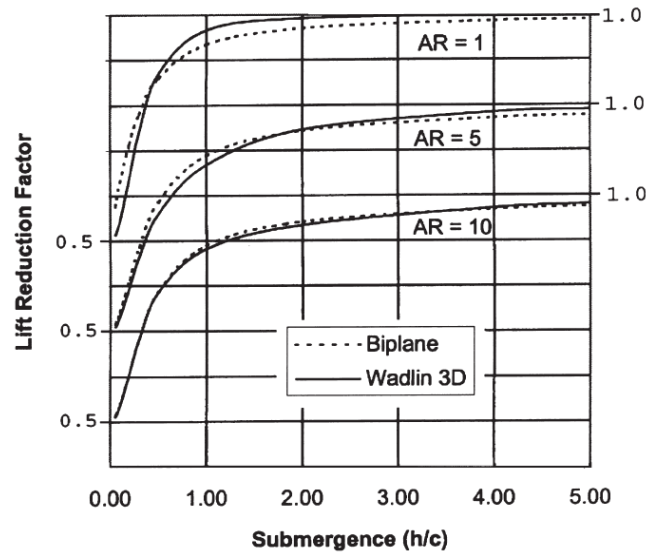


Figure 3-4: Lift reduction factor versus submergence depth to chord ratio for different AR [8]

Based on the nominal submergence (see Table 1-1) and the chord length (see Table 3-4), we have a ratio $h/c \approx 2.5$. The AR is equal to 5 (see Table 3-4), so by using the results of Figure 3-4, the lift reduction factor is calculated as $LRF = 0.95$. Based on the length of the struts and the height of the hulls, it is assumed that the hydrofoils of HEARP can operate foilborne within the range $1 \leq h/c \leq 3.5$. Using this range, the lift reduction factor can vary within the range $0.85 \geq LRF \leq 1$ with a nominal value of $ARF = 0.95$. Note that the resulting lift and drag coefficients of Figure 3-2 are estimated by experimental data for $h/c \approx 2.5$ ($ARF = 0.95$). Therefore, it is assigned to the lift coefficients an uncertainty of $[-10\%, 5\%]$.

Regarding the effect of the surface proximity on the drag coefficient, based on the experimental results in [47] it is stated that the drag coefficient depends on the ratio h/c in a similar manner as the lift coefficient. This is reasoned by the fact that C_D includes lift-induced drag that is proportional to the C_L , so as the ratio h/c reduces, the drag force reduces as well. Because it is already assigned a large amount of uncertainty to the drag coefficient due to the error of the linear approximation (see Figure 3-3), it is assumed that any variations due to surface proximity lie in the range of $[-20\%, 50\%]$.

All the required distances needed to determine the location of CP for each hydrofoil with respect to the CG of the craft are calculated using the CAD model and confirmed with

physical measurements on HEARP. Recall that it is assigned an uncertainty to the location of CG (see Table 3-2). Thus, we assign an uncertainty of $\pm 10\%$ to all the distances that depend on the location of CG. Note that for the parameter $l_{z_j}^i$, it is decided to assign an uncertainty of ± 0.05 m because of its small magnitude.

Regarding the time constant τ_δ^i for each servo motor (see Eq. (2-17)), its nominal value is fixed to $\tau_\delta^i = 0.05$ s. It is selected empirically based on the intuition of the responses of the servo motors during different experiments. However, because of the absence of measurements, we assign to the time constant an uncertainty of $[-25\%, 25\%]$. Note that the nominal value and the uncertainty of each τ_δ^i are the same for all hydrofoils. Nevertheless, each parameter is treated as an independent uncertainty because each servo motor may have a different load; thus, their responses will differ.

All the parameters that are related to the hydrofoils with their corresponding deviations from the nominal value are reported in Table 3-5 (see Chapter 2 for their definition).

Table 3-5: Parameters that are related to hydrodynamic forces

Parameter	Nominal Value	Uncertainty	Parameter	Nominal Value	Uncertainty
C_{L_0}	-3.64e-4	[-10%,5%]	μ	0.214 rad	-
C_{L_α}	3.925	[-10%,5%]	$l_{x_j}^f$	0.402 m	[-10%,10%]
C_{D_0}	0.027	[-20%,50%]	$l_{x_j}^a = l_{x_j}^{ap} = l_{x_j}^{as}$	-0.298 m	[-10%,10%]
C_{D_α}	0.155	[-20%,50%]	l_y^f	-0.024 m	[-10%,10%]
l_s	0.06 m	-	l_y^{ap}	-0.24 m	[-10%,10%]
h_h	0.178 m	-	l_y^{as}	0.19 m	[-10%,10%]
l_c	0.484 m	-	$l_{z_j} = l_{z_j}^f = l_{z_j}^{ap} = l_{z_j}^{as}$	0.006 m	[-0.05m,0.05m]
l_{a_0}	0.473 m	-	$\tau_\delta^f, \tau_\delta^{ap}, \tau_\delta^{as}$	0.05 s	[-25%,25%]

3-5-4 Equilibrium Input

To calculate the equilibrium input u_{in}^* that corresponds to the default angle of the servo motors for each of the hydrofoil, the Eq. (3-5) is used. All the nominal parameters of the system that are defined in Section 3-5 and the equilibrium conditions for states and disturbances (see Section 3-5-2) are substituted in the nonlinear state space of Eq. (3-4a). The resulting equations of the form $f(x^*, u_{in}^*, d_w^*) = 0$ are solved numerically with the use of the Matlab function `vpasolve()` [33]. The resulting equilibrium input is defined as:

$$\begin{bmatrix} \delta_s^{f*} \\ \delta_s^{ap*} \\ \delta_s^{as*} \end{bmatrix} = \begin{bmatrix} -14.00^\circ \\ -14.48^\circ \\ -20.06^\circ \end{bmatrix} \implies \begin{bmatrix} \alpha_s^{f*} \\ \alpha_s^{ap*} \\ \alpha_s^{as*} \end{bmatrix} = \begin{bmatrix} 4.72^\circ \\ 4.88^\circ \\ 6.76^\circ \end{bmatrix}$$

where the values for α_s^{i*} are calculated using Eq. (2-15).

From these results, it is observed that the equilibrium angles for the hydrofoils differ. This is reasoned by the fact that the CG of the craft in x and y axes is not located at the mid-planes of the frame due to the non-symmetrical mass distribution of HEARP. Additionally, the equilibrium angles for servo motors and the swinging angles lie within the range where their linear approximations is pretty accurate (see Figure 2-8 and Figure 3-2).

Chapter 4

Control Design

This chapter presents all the necessary background and the procedure for the design of motion control systems for a hydrofoil craft. It is worth noting that this design is focused on a hydrofoil craft that is foilborn and operates with the platforming mode (see Figure 1-4). More precisely, the general goal of the control system is to perform a stable level steady flight (see Section 3-3-1) and decouple the motions of the craft from the incident waves. Hence, tracking reference signals is essential mainly for the heave motion when the craft needs to change its altitude. For example, this may happen when the wave amplitude changes or the craft has to perform a landing or take-off.

The controllers presented in this chapter are designed using the fundamental theory of multi-variable feedback control for linear systems. The largest portion of the content of this chapter was taken from [44]. Furthermore, the controller synthesis and the analysis of system properties are done using the Control System Toolbox and the Robust Control Toolbox of Matlab [33]. The required background of the theory for the different algorithms and functions is presented briefly. Thus, the interested readers are prompted to use the given references for more information.

4-1 Fundamental Properties of Control Systems

This section introduces some of the properties of linear systems that are useful for the design of feedback controllers. Two of the fundamental properties of a control system are the concepts of state *controllability* and state *observability*. These two concepts are explained briefly below [44].

Definition 4.1 State Controllability. *The dynamical system $\dot{x} = Ax + Bu$, or equivalently the pair (A, B) , is said to be state controllable if, for any initial state $x(0) = x_0$, any time $t_1 > 0$ and any final state x_1 , there exists an input $u(t)$ such that $x(t_1) = x_1$. Otherwise, the system is said to be state uncontrollable.*

The system (A, B) is state controllable if and only if the controllability matrix

$$\mathcal{C} \triangleq [B \ AB \ A^2B \ \dots \ A^{n-1}B]$$

has rank n (full row rank). Here n is the number of states.

Definition 4.2 State observability. *The dynamical system $\dot{x} = Ax + Bu$, $y = Cx + Du$ (or the pair (A, C)) is said to be state observable if, for any time $t_1 > 0$, the initial state $x(0) = x_0$ can be determined from the time history of the input $u(t)$ and the output $y(t)$ in the interval $[0, t_1]$. Otherwise the system, or (A, C) , is said to be state unobservable.*

The system (A, C) is state observable if and only if we have full column rank (rank n) of the observability matrix

$$\mathcal{O} \triangleq \begin{bmatrix} C \\ CA \\ CA^2 \\ \vdots \\ CA^{n-1} \end{bmatrix}$$

If a system is not controllable, it can be divided into two subsystems, one of which (if it exists) is controllable, and the other is uncontrollable. If the uncontrollable subsystem is stable, i.e. all the poles lie in the left-half plane (LHP), then the entire system is said to be *stabilizable*. The set of stabilizable systems includes the controllable systems as a subset, i.e. every controllable system is stabilizable, but not every stabilizable system is controllable. Similarly, a system that is not observable can be divided into two subsystems, one of which (if it exists) is observable and the other is not. If the unobservable subsystem is stable, the entire system is said to be *detectable*. Thus the observable systems are a subset of the detectable systems [16]. A more formal definition of these properties is given below [44].

Definition 4.3 Stabilizable, detectable and hidden unstable modes. *A system is stabilizable if all unstable modes are state controllable. A system is detectable if all unstable modes are observable. A system with unstabilizable or undetectable modes is said to contain hidden unstable modes.*

Another important property that is very useful for the design of feedback controllers is the concept of minimal realization, which is given below [44].

Definition 4.4 Minimal realization, McMillan degree and hidden mode. *A state-space realization (A, B, C, D) of $G(s)$ is said to be a minimal realization of $G(s)$ (see Eq. (4-1)) if A has the smallest possible dimension (i.e. the fewest number of states). The smallest dimension is called the McMillan degree of $G(s)$. A mode is hidden if it is not state controllable or observable and thus does not appear in the minimal realization.*

Since only controllable and observable states contribute to the input-output behaviour from u to y , it follows that a state-space realization is minimal if and only if (A, B) is state controllable and (A, C) is state observable.

The system of HEARP (see Eq. (3-7)) it is controllable and observable, as the controllability matrix \mathcal{C} and the observability matrix \mathcal{O} have full rank, i.e. $\text{rank}(\mathcal{C}) = n = 6$ and $\text{rank}(\mathcal{O}) = n = 6$.

4-2 System Representation in the Frequency Domain

The classical frequency response techniques are fundamental parts of multivariable feedback control theory for the analysis and design of controllers. These techniques have been successfully used by control engineers in industrial applications for decades and can provide insight into the benefits and limitations of feedback control. The transfer function is the representation of system dynamics in the frequency domain. The LTI model of Eq. (3-7) is transformed to the transfer function representation by applying Laplace transform, which finally results in:

$$\begin{aligned} y(s) &= \left(C(sI - A)^{-1}B + D \right) u_{in}(s) + \left(C(sI - A)^{-1}B_d \right) d_w(s) \\ &= G(s)u_{in}(s) + G_d(s)d_w(s) \end{aligned} \quad (4-1)$$

where $G(s)$ represent the effect of the inputs u_{in} on the outputs y , whereas $G_d(s)$ represents the effect the disturbances d_w (incident waves) on y [44].

For SISO systems, $G(s)$ is a rational transfer function of the form:

$$G(s) = \frac{\beta_{n_z}s^{n_z} + \dots + \beta_1s + \beta_0}{s^n + \alpha_{n-1}s^{n-1} + \dots + \alpha_1 + \alpha_0} \quad (4-2)$$

where $\alpha_0, \alpha_1, \dots, \alpha_n$ and $\beta_0, \beta_1, \dots, \beta_{n_z}$ scalar real coefficients independent of time.

For MIMO systems, $G(s)$ is a matrix of transfer functions of the form:

$$\begin{bmatrix} y_1 \\ \vdots \\ y_l \end{bmatrix} = \underbrace{\begin{bmatrix} g_{11}(s) & g_{12}(s) & \cdots & g_{1m}(s) \\ g_{21}(s) & g_{22}(s) & \cdots & g_{2m}(s) \\ \vdots & \vdots & \ddots & \vdots \\ g_{l1}(s) & g_{l2}(s) & \cdots & g_{lm}(s) \end{bmatrix}}_{G(s)} \begin{bmatrix} u_1 \\ \vdots \\ u_m \end{bmatrix} \quad (4-3)$$

where $g_{ij}(s)$ represents the transfer function from input j to output i .

For the specific problem of the HEARP, $G(s)$ is a matrix of transfer functions with three inputs and three outputs, while $G_d(s)$ is a matrix of transfer functions with six inputs and three outputs. These transfer function matrices are obtained by using the Eq. (4-1) and their numerical values are given in Eq. (B-1) and Eq. (B-2) respectively.

For the same problem, $G_{sm}(s)$ denotes the transfer function matrix of the actuator dynamics, which is based on the model of Eq. (2-17). It is defined as a block-diagonal system of the form:

$$\underbrace{\begin{bmatrix} \delta_s^f \\ \delta_s^{ap} \\ \delta_s^{as} \end{bmatrix}}_{u_{in}(s)} = \underbrace{\begin{bmatrix} g_{sm}^f(s) & 0 & 0 \\ 0 & g_{sm}^{ap}(s) & 0 \\ 0 & 0 & g_{sm}^{as}(s) \end{bmatrix}}_{G_{sm}(s)} \underbrace{\begin{bmatrix} \delta_{s,c}^f \\ \delta_{s,c}^{ap} \\ \delta_{s,c}^{as} \end{bmatrix}}_{u_c(s)}, \quad \text{where } g_{sm}^i(s) = \frac{1}{\tau_\delta^i s + 1} \quad (4-4)$$

The numerical values of $G_{sm}(s)$ are given in Eq. (B-3). An illustration of the open-loop block diagram of the HEARP system is shown in Figure 4-1.

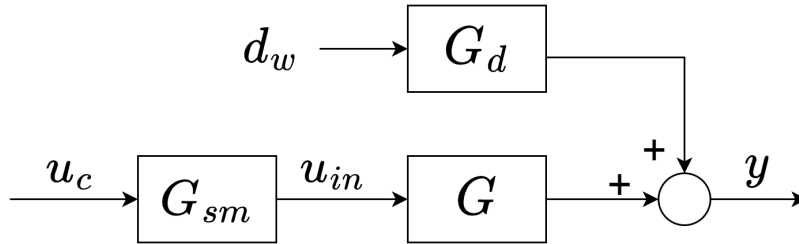


Figure 4-1: Open-loop block diagram of the HEARP system

4-2-1 Poles and Zeros

In Eq. (4-2), n is the order of the denominator (pole polynomial) and is also called the order of the system, and n_z is the order of the numerator (or zero polynomial). In addition, $n - n_z$ denotes the pole excess or relative order of the system. Most practical systems are proper, i.e. $n \geq n_z$, so they are realized by the state-space description of Eq. (3-7) and the transfer functions of Eq. (4-1).

The poles of $G(s)$ are defined as the finite values $s = p$, where $G(p)$ has a singularity ("is infinite"), or alternatively the eigenvalues (modes) of the state-space matrix A . Note that if A does not correspond to a minimal realization, then the set of the resulting poles will include the poles (eigenvalues) corresponding to uncontrollable and/or unobservable states (see Section 4-1).

The zeros of $G(s)$ arise when competing effects, internal to the system, are such that the output is zero even when the inputs (and the states) are not themselves identically zero. In the general case that also includes multivariable systems, z_i is a zero of $G(s)$ if the rank of $G(z_i)$ is less than the normal rank of $G(s)$. This definition of zeros for multivariable systems is based on the transfer function matrix, corresponding to a minimal realization of a system, and they are also called *transmission zeros*.

By the right-half plane (RHP), we mean the closed right half of the complex plane, including the imaginary axis ($j\omega$ -axis). The LHP is the open left half of the complex plane, excluding the imaginary axis. A RHP-pole (unstable pole) is a pole located in the right-half plane and thus includes poles on the imaginary axis. Similarly, a RHP-zero ("unstable" zero) is a zero located in the right-half plane [44].

The poles and the transmission zeros of the transfer function matrices $G(s)$ and $G_d(s)$ (see Eq. (4-1)) are calculated using the Matlab functions `pole(.)` and `tzero(.)` [33]. Their numerical values are reported in Table 4-1. From Table 4-1, it is observed that the both systems do not have any transmission zeros, while they have four real stable poles that lie in the LHP and two poles located at 0. The similarity of the poles of the systems $G(s)$ and $G_d(s)$ is justified by the fact that they have the same state-space matrix A .

The results of Table 4-1 indicate that the system is marginally stable, i.e. for a bounded input the resulting steady-state output will be dominated by oscillations with constant amplitude [10]. Moreover, it is deduced that the stable modes of the system are over-damped as they have zero complex parts. Similar results regarding the location of the poles of hydrofoil crafts are found in [40] and [4], which implies that our results are reasonable. It is worth noting that

the system does not have fundamental limitations on performance because of the presence of RHP-poles or RHP-zeros (there are not exist in this system).

Table 4-1: Poles and transmission zeros of the transfer function matrices $G(s)$ and $G_d(s)$

Poles	Zeros
0.00	-
0.00	
-30.55	
$-2.91 \cdot 10^{-15}$	
-7.85	
-5.54	

4-2-2 Frequency Response

To obtain the frequency response of the system, we replace s by $j\omega$ in the transfer function model $G(s)$. This can mainly describe the system's response to sinusoidal input with varying frequency. The advantage of this interpretation is that it is directly linked to the time domain. At each frequency ω , the complex number $G(j\omega)$ (or complex matrix for a MIMO system) captures how the system reacts to persistent sinusoidal inputs of frequency ω .

A physical interpretation of the frequency response of a stable linear system $y = G(s)u$ is defined as follows: by sending a sinusoidal input signal through a system $G(s)$, the magnitude of the output signal is amplified by a factor $|G(j\omega)|$ and its phase is shifted by $\angle G(j\omega)$. Both $|G(j\omega)|$ and $\angle G(j\omega)$ depend on the frequency ω . The dependency of these variables is plotted explicitly in Bode plots (with ω as the independent variable) or implicitly in a Nyquist plot (phase plane plot). These plots are useful tools for analysing the design, stability and performance of feedback controllers.

It is worth noting that, in general, MIMO systems are coupled. To explain this concept, consider a MIMO plant with m inputs and l outputs and a transfer matrix $G(s)$ (see Eq. (4-3)). Then if there is a change in the first input, u_1 , then this will generally affect all the outputs, y_1, y_2, \dots, y_l . That is, there is an interaction between all the inputs and outputs. A non-interacting plant would result if u_1 only affects y_1 , u_2 only affects y_2 , and so on.

The main difference between a scalar (SISO) system and a MIMO system is the presence of directions in the latter. Directions are relevant for vectors and matrices but not for scalars. However, most of the techniques used for SISO systems may be extended to MIMO systems. The singular value decomposition (SVD) is a helpful tool to quantify multivariable directionality, so most SISO results involving the absolute value (magnitude) may be generalised to multivariable systems by considering the maximum singular value. This tool is introduced briefly as follows [44].

Consider a fixed frequency ω where $G(j\omega)$ is a constant $l \times m$ complex matrix, and denote $G(j\omega)$ by G for simplicity. Any matrix G may be decomposed into its singular value decomposition, and we write

$$G = U\Sigma V^H$$

where

Σ is an $l \times m$ matrix with $k = \min\{l, m\}$ non-negative singular values, σ_i , arranged in descending order along its main diagonal; the other entries are zero. The singular values are the positive square roots of the eigenvalues of $G^H G$ for a given frequency, where G^H is the complex conjugate transpose of G ,

$$\sigma_i(G) = \sqrt{\lambda_i(G^H G)}$$

U is an $l \times l$ unitary matrix of output singular vectors, u_i that represent the output directions of the plant.

V is an $m \times m$ unitary matrix of input singular vectors, v_i that represent the input directions.

The singular values of a transfer function are important indicators of frequency domain performance and robustness as well (see Section 4-3-3). They can be computed numerically using the Matlab function `sigma(·)` [33].

4-2-3 \mathcal{H}_∞ norm

The symbol \mathcal{H} stands for Hardy space. The set of all stable and proper transfer functions is denoted by \mathcal{H}_∞ . By considering a proper linear stable system $G(s)$, its \mathcal{H}_∞ norm is defined as the maximum of the largest singular values of $G(s)$ across all frequencies, which is defined as:

$$\|G(s)\|_\infty \triangleq \max_{\omega} \bar{\sigma}|G(j\omega)|$$

Roughly speaking, using this norm in the control design method, we aim to minimize the peak(s) of the singular values of one or more selected transfer functions [44]. The value of \mathcal{H}_∞ norm of any transfer function matrix can be obtained using the Matlab function `norm(·)` [33].

4-2-4 Structured Singular Value

The structured singular value μ is a function which provides a generalization of the singular value $\bar{\sigma}$, and the spectral radius ρ (absolute value of maximum eigenvalue). With the use of μ , necessary and sufficient conditions for Robust Stability (RS) and Robust Performance (RP) can be obtained in order to evaluate the robustness of the designed controller. More details about the evaluation of the controllers are shown later in Section 4-7. A formal definition of the structured singular value is given as follows:

Definition 4.5 Structured singular value. *Let M be a given complex matrix and let $\Delta = \text{diag}\{\Delta_I\}$ denote a set of complex matrices with $\bar{\sigma}(\Delta) \leq 1$ and with a given block-diagonal structure (in which some of the blocks may be repeated and some may be restricted to be real). The real non-negative function $\mu(M)$, called the structured singular value, is defined by*

$$\mu(M) \triangleq \frac{1}{\min\{k_m | \det(I - k_m M \Delta) = 0 \text{ for structured } \Delta, \bar{\sigma}(\Delta) \leq 1\}}$$

where k_m is the so-called multivariable stability margin (scalar factor). If no such structured Δ exists then $\mu(M) = 0$.

A large value of μ is "bad" as it means that a small perturbation makes $(I - M\Delta)$ singular. Therefore, in general it is desired to have a small value of μ , and more specifically less than 1 [44]. The value of μ as function of frequency for any transfer function matrix can be obtained using the Matlab function `musvv()` [33].

4-3 Feedback Control

4-3-1 Closed-loop Transfer Functions

The objective of a control system is to manipulate the plant input u with the aim of achieving the desired response of the output y . The goal of the servo problem (reference tracking) is to control u such that the output is kept close to a given reference input r . On the other hand, the goal of the regulator problem (disturbance rejection) is to control u to counteract the effect of a disturbance d . For both cases, we aim to maintain the control error $e = y - r$ small enough. The algorithm for manipulating u based on the available information is the controller K . A priori information about the expected disturbances and reference inputs, the plant model (G) and disturbance model (G_d), are needed to arrive at a satisfactory design for K . A block diagram for the negative feedback structure is shown in Figure 4-2.

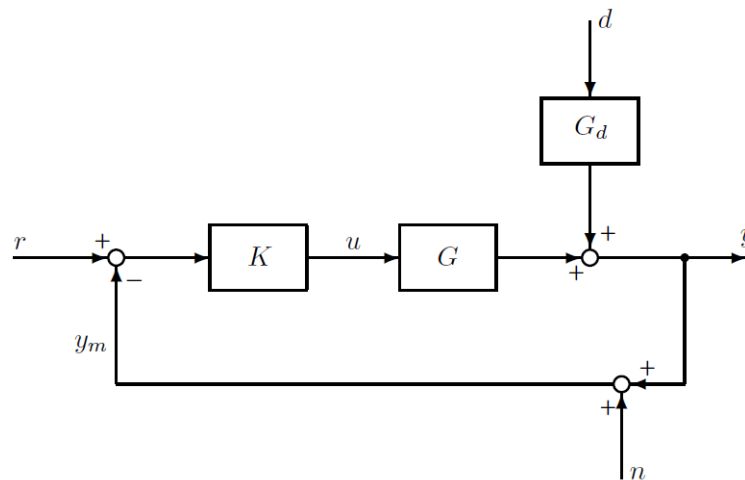


Figure 4-2: Block diagram of a negative feedback control system [44]

The input to the controller $K(s)$ is $r - y_m$ where $y_m = y + n$ is the measured output and n is the measurement noise. Therefore, the input to the plant is

$$u = K(s)(r - y - n) \quad (4-5)$$

For a negative feedback controller, the substitution of Eq. (4-5) into Eq. (4-1) yields the derivation of the equation of closed-loop response for the feedback control system which is

given as:

$$\begin{aligned}
 y &= GK(r - y - n) + G_d d \\
 (I + GK)y &= GKr + G_d d - GK n \\
 \implies y &= \underbrace{GK(I + GK)^{-1}r}_T + \underbrace{(I + GK)^{-1}G_d d}_S - \underbrace{GK(I + GK)^{-1}n}_T
 \end{aligned} \tag{4-6}$$

The control error is:

$$e = y - r = -Sr + SG_d d - Tn \tag{4-7}$$

where we have used the fact that $T - I = S$. The corresponding plant input signal is:

$$u = K Sr - K S G_d d - K S n = K S (r - G_d d - n) \tag{4-8}$$

The following notation and terminology are used:

- Loop transfer function: $L = GK$
- Sensitivity function: $S = (I + GK)^{-1} = (I + L)^{-1}$
- Complementary sensitivity function: $T = GK(I + GK)^{-1} = L(I + L)^{-1}$

From Eq. (4-6) it is seen that S is the closed-loop transfer function from the output disturbances to the outputs, while T is the closed-loop transfer function from the reference signals to the outputs. The term complementary sensitivity for T follows from the identity $T + S = I$ [44].

4-3-2 Stability

A critical issue in designing feedback controllers is to achieve stability. For LTI systems, the following definition is used to describe stability:

Definition 4.6. *A system is (internally) stable if none of its components contains hidden unstable modes and the injection of bounded external signals at any place in the system results in bounded output signals measured anywhere in the system.*

Here we define a signal $u(t)$ to be "bounded" if there exists a constant c such that $|u(t)| < c$ for all t . The word internally is included in the definition to stress that we not only require the response from one particular input to another particular output to be stable but also require stability for signals injected or measured at any point in the system [44]. The internal stability of a control system can be evaluated easily using the appropriate the closed-loop system and the Matlab function `isstable(.)` [33].

4-3-3 Evaluating closed-loop performance

Besides closed-loop stability, a key objective of control is to improve performance, that is, to make the output $y(t)$ exhibit desirable characteristics. The evaluation of the closed-loop performance of systems is performed mainly either in the time domain via step response analysis or in the frequency domain via frequency response analysis. The advantage of the frequency domain over step response analysis is that it considers a broader class of signals (sinusoids of

any frequency). This makes it simpler to characterize feedback properties, particularly system behaviour around the bandwidth area. The characterization of the closed-loop performance in the frequency domain can be done from the frequency responses of the loop transfer function $L(j\omega)$ and the closed-loop transfer functions $T(j\omega)$ and $S(j\omega)$.

For MIMO systems, $\sigma(S(j\omega))$ is a function of frequency that gives useful information about the effectiveness of feedback control. To give a short explanation of this, consider the ratio $\|e(\omega)\|_2/\|r(\omega)\|_2$, where r is the vector of sinusoidal reference inputs, e is the vector of control errors, and $\|\cdot\|$ is the vector 2-norm. This gain depends on the direction of $r(\omega)$, and it is bounded by the maximum and minimum singular value of S ,

$$\underline{\sigma}(S(j\omega)) \leq \frac{\|e(\omega)\|_2}{\|r(\omega)\|_2} \leq \bar{\sigma}(S(j\omega))$$

In terms of performance, it is reasonable to require that the gain $\|e(\omega)\|_2/\|r(\omega)\|_2$ remains small for any direction of $r(\omega)$, including the "worst-case" direction which gives a gain of $\bar{\sigma}(S(j\omega))$. The singular values of $S(j\omega)$ may be plotted as functions of frequency. Typically, they are small at low frequencies where feedback is effective, and they approach 1 at high frequencies because any real system is strictly proper.

The maximum singular values of the sensitivity and complementary sensitivity functions, $M_S = \bar{\sigma}(S(j\omega))$ and $M_T = \bar{\sigma}(T(j\omega))$, usually has a peak larger than 1 around the gain crossover frequency ω_c (frequency where $\bar{\sigma}(L(j\omega)) = 1$). This peak is undesirable, but it is unavoidable for real systems. A large value of M_S or M_T indicates poor performance and robustness. Upper bounds on M_T and M_S have been common design specifications in classical control because they are related to the quality of the response in the time domain (overshoot and steady-state offset).

The concept of bandwidth is crucial for understanding the benefits and trade-offs involved when applying feedback control. Above, we considered peaks of closed-loop transfer functions, M_T and M_S , which are related to the quality of the response. For performance evaluation, we should also consider the response's speed (rise time and settling time), which leads to the consideration of the bandwidth frequency of the system. Generally, a large bandwidth corresponds to a shorter rise time since high-frequency signals are more easily "passed on" to the outputs. Nevertheless, a high bandwidth denotes that the system is sensitive to noise. In contrast, the speed of the response is typically slow if the bandwidth is small, so the system is more robust.

For MIMO systems the bandwidth depends on directions, and we have a bandwidth region between a lower frequency where the maximum singular value $\bar{\sigma}(S(j\omega))$ ("worst-case" direction) reaches 0.7, and a higher frequency where the minimum singular value $\underline{\sigma}(S(j\omega))$ ("best-case" direction) reaches 0.7. If we want to associate a single bandwidth frequency for a multivariable system, then we consider the worst-case direction, and we define *bandwidth* ω_B as the frequency where $\bar{\sigma}(S(j\omega))$ crosses $\frac{1}{\sqrt{2}} = 0.7$ from below [44].

4-4 Signal-based \mathcal{H}_∞ Optimal Control Design

This section introduces the control design methodology of the signal-based \mathcal{H}_∞ optimal control. It is very general and appropriate for multivariable problems in which several objectives

must be considered simultaneously. In this approach, we define the plant and possibly the model uncertainty, the class of external signals affecting the system, and the norm of the error signals we want to keep small. Weights describe the expected or known frequency content of exogenous signals and the desired frequency content of error signals. Weights can also be used to model the uncertainties of the system. In this section, the synthesis procedure of the controller takes into account only the nominal plant, while in the Section 4-6, the synthesis methodology is extended for the model that also includes all the uncertainties of the system. With this method, one can synthesize a controller by minimizing an \mathcal{H}_∞ performance objective. This design strategy can automate the controller design and leaves the engineer to select reasonable bounds ("weights") on the desired closed-loop transfer functions [44].

4-4-1 Configuration of the Generalized Plant

For the specific problem of the hydrofoil craft, the signal-based \mathcal{H}_∞ control design methodology is formulated according to the block diagram of Figure 4-3. This formulation uses the general control configuration, where P is the generalized plant and K is the generalized controller. Note that in this formulation, the measurement noise is not considered. To construct P , one should note that it is an open-loop system in which all the signals that entering and exiting the controller K are considered. The definitions of the components and signals of the block diagram of Figure 4-3 are summarized below:

- G : Plant model (see Eq. (4-1))
- G_d : Disturbance model (see Eq. (4-1))
- G_{sm} : Actuator model (see Eq. (4-4))
- u_c : Commanded plant inputs (output of the controller, input to G_{sm})
- u_{in} : Actual plant inputs (output of G_{sm} , input to G)
- v : Controller inputs that consist of the commands and the measured system outputs (see Eq. (4-5)).
- w : Exogenous inputs that include the reference inputs (commands, setpoints) r and the wave disturbances d_w .
- z : Exogenous outputs that consist of the error signals z_1 to be minimized (see Eq. (4-7)), and the commanded plant inputs u_c (z_2).
- P : Generalized plant model that includes G , G_d and G_{sm} , the interconnection structure between the plant and the controller K , and the weighting functions that are used for the controller synthesis (see Section 4-4-2).

The equations of the output signals as a function of the input signals for the block diagram of Figure 4-3 are given by:

$$\begin{aligned} z_1 &= W_P W_r r - W_P G_d W_d d_w - W_P G G_{sm} u_c \\ z_2 &= W_u u_c \\ v &= W_r r - G_d W_d d_w - G G_{sm} u_c \end{aligned}$$

Thus, the generalized plant P is a transfer function matrix with dimensions 9×12 and has the following structure:

$$\begin{bmatrix} z_1 \\ z_2 \\ v \end{bmatrix} = P(s) \begin{bmatrix} r \\ d_w \\ u_c \end{bmatrix} = \begin{bmatrix} W_P W_r & -W_P G_d W_d & -W_P G G_{sm} \\ O_{3 \times 3} & O_{3 \times 6} & W_u \\ W_r & -G_d W_d & -G G_{sm} \end{bmatrix} \begin{bmatrix} r \\ d_w \\ u_c \end{bmatrix} \quad (4-9)$$

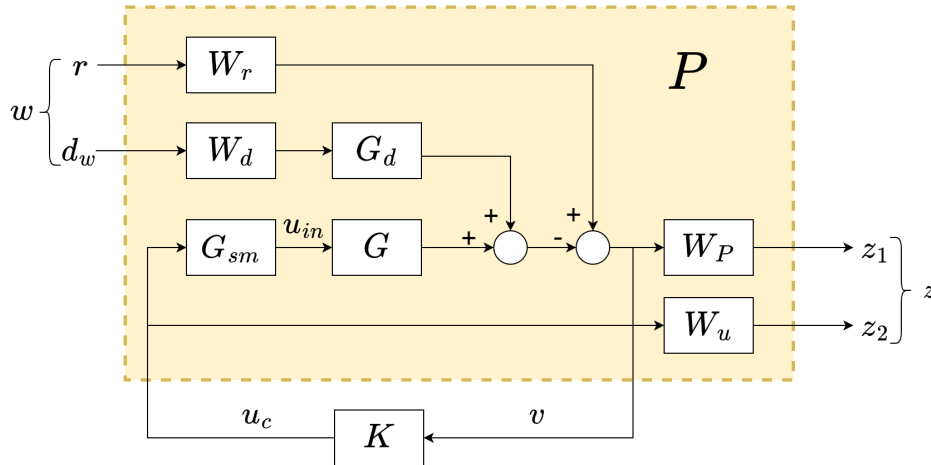


Figure 4-3: Block diagram of signal-based \mathcal{H}_∞ optimal control problem for the nominal plant

The generalized plant P in Eq. (4-9) is constructed using the Matlab function `connect()` [33].

4-4-2 Weight Design

As it is shown in Figure 4-3, the signal-based \mathcal{H}_∞ control design methodology includes different weighting functions. The choice of these weights is made aiming to achieve the desired closed-loop performance of the system, which satisfies certain requirements. More precisely, the weights W_r and W_d may be constant or dynamic and describe the relative importance and/or frequency content of the reference signals and the disturbances. Additionally, the weights W_P and W_u respect the desired frequency content of the error e and the control signals u_c , respectively. The design of these weighting functions is introduced in this section. It is important to mention that their final design is selected based on the recommendations from theory and after an iterative procedure of tuning their different parameters. This tuning is done using the results of different frequency responses and simulations for the objectives of reference tracking and disturbance rejection.

Performance Weight

Recall from 4-3-3 that the sensitivity function S is a valuable tool for evaluating closed-loop performance in both SISO and MIMO systems. Because we preferably want S to be small, for MIMO systems it is sufficient to consider simply its maximum singular value $\bar{\sigma}(S(j\omega))$. Let $1/|w_P(s)|$ (the inverse of the performance weight) represent the maximum allowed magnitude of $\|e(\omega)\|_2/\|r(\omega)\|_2$ at each frequency. This results in the following performance requirement:

$$\begin{aligned} \bar{\sigma}(S(j\omega)) < 1/|w_P(j\omega)|, \forall \omega &\Leftrightarrow \bar{\sigma}(w_P S(j\omega)) < 1, \forall \omega \\ &\Leftrightarrow \|w_P S\|_\infty < 1 \end{aligned}$$

where the \mathcal{H}_∞ norm (see also Section 4-2-3) is defined as the peak of the maximum singular value of the frequency response.

A common choice for the performance weight matrix for MIMO systems is

$$W_P = \text{diag}\{w_{P,i}\} \quad \text{where } w_{P,i}(s) = \frac{s/M_i + \omega_{B,i}}{s + \omega_{B,i}A_i} \quad (4-10)$$

Selecting $A_i \ll 1$ ensures approximate integral action with $S(0) \approx 0$ (minimize steady-state tracking error). The variable M_i represents the required maximum peak magnitude of S for each output. The peak specification is often selected as less than 2 for all outputs, preventing noise amplification at high frequencies and introducing a margin of robustness. The variable $\omega_{B,i}$ defines the desired closed-loop bandwidth which may be different for each output. A large value of $\omega_{B,i}$ yields a faster response for output i [44].

The weights of Eq. (4-10) are finally selected the same for all channels and their numerical values are summarized below:

- $M_i = 1.5$
- $A_i = 10^{-4}$
- $\omega_{B,i} = 5 \text{ rad/s}$

Therefore the performance weight W_P is a block diagonal transfer function matrix of the form:

$$W_P(s) = w_{P,i}(s)I_3, \quad \text{where } w_{P,i}(s) = 0.67 \frac{s + 7.5}{s + 0.0005} \quad (4-11)$$

where I_3 denotes the identity matrix of dimension 3.

Control Input Weight

A way to achieve robustness and to restrict the magnitude of the input signals (see (4-8)), is to place an upper bound $|1/w_{u,i}(s)|$ on the magnitude of each output channel i of the system $\|KS\|_\infty$. If we require tight control at low frequencies, then input usage is unavoidable at low frequencies. However, it is essentially limited by the allowable cost of control effort and saturation limit of the actuators. In general, it is required to use a high-frequency penalty to minimize the usage of the control input at high frequencies, so that sensitivity to noise and disturbance signals is avoided. A common choice to satisfy these requirements is given by:

$$w_{u,i}(s) = \frac{s + \omega_{bc,i}/M_{u,i}}{\epsilon_i s + \omega_{bc,i}} \quad (4-12)$$

where $\omega_{bc,i}$ represent the required maximum bandwidth of the controller. Moreover $M_{u,i}$ and ϵ_i represents the magnitude of $|w_{u,i}(j\omega)|$ at low frequencies and at high frequencies respectively [50].

Recall from Section 2-8-2 that the actuators (servo motors) have limitations on their magnitude. Hence, the weighting functions $w_{u,i}(s)$ are tuned by an iterative procedure such that system performance is satisfactory and control input signals are kept away from the saturation limits of the servo motors. The weights of Eq. (4-12) are selected the same for all control inputs, and their values are summarized below:

- $M_{u,i} = 100$
- $\omega_{bc,i} = 50 \text{ rad/s}$
- $\epsilon_i = 0.001$

Therefore the overall control input weight W_u is a block diagonal transfer function matrix of the form:

$$W_u(s) = w_{u,i}(s)I_3, \quad \text{where } w_{u,i}(s) = 1000 \frac{s + 0.05}{s + 50000} \quad (4-13)$$

where I_3 denotes the identity matrix of dimension 3.

Reference Signal Weight

Recall that the primary goal of the motion control system for the hydrofoil craft that is foilborne and operates with the platforming mode is to perform a stable level steady flight while it rejects the wave disturbances. Regarding the goal of reference tracking, we are mainly interested in the heave motion, while the roll and pitch motions have less importance. To achieve a high-performance system response with low overshoot and small control signals, the reference signals should be limited in low-frequency changes. For example, step signals that has infinite frequency content should be avoided because the instantaneous change of their value.

We therefore use as a weighting function for reference signals the transfer function of a DC amplifier [10]. It is a low-pass filter multiplied with a gain, and it is described by:

$$w_{r,i}(s) = \frac{k_{0,i}}{\tau_{r,i}s + 1}$$

For frequencies above $\omega = 1/\tau_{r,i}$ the log magnitude decreases rapidly toward $-\infty$, thus the output of $w_{r,i}$ can follow a sinusoidal input faithfully at frequencies $\omega \leq 1/\tau_{r,i}$ [38]. The gain $k_{0,i}$ represents the magnitude of the transfer function at low frequencies, i.e. $k_{0,i} = |w_{r,i}(0)|$. Therefore it can be used to tune the importance of the reference tracking for each channel.

Finally, the values of the weighting functions for reference signals are chosen the same for all channels, except the gain of the heave motion that is chosen higher than the gains of roll and pitch motions. Their values are summarized below:

- $k_{0,z_n} = 0.2$
- $k_{0,i} = 0.1$
- $\tau_{r,\phi} = \tau_{r,\theta} = 4 \text{ s}$

Therefore the reference weight W_r is a block diagonal transfer function matrix of the form:

$$W_r(s) = \begin{bmatrix} w_{r,z_n}(s) & 0 & 0 \\ 0 & w_{r,\phi}(s) & 0 \\ 0 & 0 & w_{r,\theta}(s) \end{bmatrix}$$

where

$$w_{r,z_n}(s) = \frac{0.05}{(s + 0.25)} \quad w_{r,\phi}(s) = w_{r,\theta}(s) = \frac{0.025}{(s + 0.25)}$$

Wave Disturbance Weight

The frequency content of the wave excitation forces acting on the hydrofoil craft is dominated by the range of expected encounter frequencies. Thus, the selected frequency range of the

waves is taken into account for the design of the wave disturbance weight. In this way, we aim to design a controller that shall be capable of rejecting any wave disturbances with frequencies in this range. Recall from Section 2-7-2 that the selected range of wave frequencies is $1.57 \text{ rad/s} \leq \omega \leq 15.70 \text{ rad/s}$. Using Eq. (2-13) and the nominal cruise velocity of $U_0 = 4 \text{ m/s}$, we calculate the maximum and minimum absolute values of the encounter frequencies ω_e for head and following waves. The resulting values are reported in Table 4-2. From the results of Table 4-2, it is observed that the maximum absolute value for encounter frequency occurs for head waves, while the minimum one occurs for following waves.

Table 4-2: Maximum and minimum of absolute values for the encounter frequencies of head and following waves

Wave type	Encounter angle β ($^\circ$)	Max $ \omega_e $ (rad/s)	Min $ \omega_e $ (rad/s)
Head	180	32.98	8.54
Following	0	17.28	1.52

Hence, the weighting function for the wave disturbances is modelled as a band pass filter, which allows a non-zero magnitude of the disturbance signal only for frequencies that lie within the selected frequency range. This type of filter is described by:

$$\begin{aligned}\omega_0 &= \sqrt{\omega_H \omega_L} \\ Q &= \frac{\omega_0}{\omega_H - \omega_L} \\ w_{d,i}(s) &= \frac{H_{0,i} \frac{\omega_0}{Q} s}{s^2 + \frac{\omega_0}{Q} s + \omega_0^2}\end{aligned}$$

where ω_H and ω_L denotes the high and low frequencies that define the required range and H_0 denotes the maximum peak of $w_{d,i}(s)$, i.e. $H_0 = \max(|w_{d,i}(j\omega)|)$ [51]. The value of $H_{0,i}$ can be used to tune the importance of the disturbance rejection for each channel.

The values of the weighting functions for wave disturbances are chosen the same for all channels, and their values are reported below:

- $H_{0,i} = 1.5$
- $\omega_L = 1.52 \text{ rad/s}$
- $\omega_H = 32.98 \text{ rad/s}$

Therefore the wave disturbance weight W_d is a block diagonal transfer function matrix of the form:

$$W_d(s) = w_{d,i}(s)I_6, \quad \text{where } w_{d,i}(s) = \frac{47.19s}{(s + 29.78)(s + 1.68)}$$

where I_6 denotes the identity matrix of dimension 6.

4-4-3 Controller synthesis

The overall control objective of the \mathcal{H}_∞ optimal controller is to minimize the worst-case norm of the transfer function matrix N from w to z across all frequencies (see Figure 4-4), i.e. the \mathcal{H}_∞ norm [44]. The controller design problem is then:

- Find a controller K , which, based on the information in v , generates a control signal u_c , which counteracts the influence of w on z , thereby minimizing the closed-loop norm from w to z ($z = Nw$).

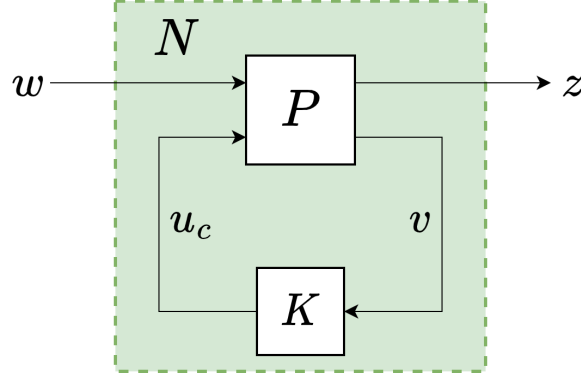


Figure 4-4: General control configuration for the case with no model uncertainty [44]

The generalized plant in Figure 4-4 is described by:

$$\begin{bmatrix} z \\ v \end{bmatrix} = P(s) \begin{bmatrix} w \\ u_c \end{bmatrix} = \begin{bmatrix} P_{11}(s) & P_{12}(s) \\ P_{21}(s) & P_{22}(s) \end{bmatrix} \begin{bmatrix} w \\ u_c \end{bmatrix} \quad (4-14)$$

$$u_c = K(s)v \quad (4-15)$$

with a state-space realization of the generalized plant P given by

$$P \stackrel{s}{=} \left[\begin{array}{c|cc} A & B_1 & B_2 \\ \hline C_1 & D_{11} & D_{12} \\ C_2 & D_{21} & D_{22} \end{array} \right] \quad (4-16)$$

The result of Eq. (4-14) is obtained by partitioning the generalized plant P of Eq. (4-9) such that its parts are compatible with the signals w , z , u_c and v . More precisely, the parts have dimensions: P_{11} : 6×9 , P_{12} : 6×3 , P_{21} : 3×9 and P_{22} : 3×3 .

Note that P_{22} has dimensions compatible with the controller, i.e. if K is an $n_{u_c} \times n_v$ matrix, then P_{22} is an $n_v \times n_{u_c}$ matrix. From Eq. (4-9) we deduce that $P_{22} = -GG_{sm}$. This subsystem actually corresponds to the series connection of the actuators model and the plant model and has a negative sign because of the negative feedback.

The closed-loop system N is derived by using a lower linear fractional transformation (LFT) of P with K as the parameter, and it is described by:

$$N = F_l(P, K) \triangleq P_{11} + P_{12}K(I - P_{22}K)^{-1}P_{21} \quad (4-17)$$

The derivation of N from P and K is performed easily using the Matlab function `lft`(\cdot) [33]. Note that for the \mathcal{H}_∞ synthesis problem, N has dimensions 6×9 .

With reference to the general control configuration of Figure 4-4, the standard \mathcal{H}_∞ optimal control problem is to find a stabilizing controller K (a controller that yield internal stability of the closed-loop system), which minimizes:

$$\gamma = \min_K \|N(K)\|_\infty, \quad \text{where } \|N(K)\|_\infty = \max_\omega \bar{\sigma}(N(K)(j\omega)) \quad (4-18)$$

Generally, when $\gamma < 1$, the resulting controller satisfies all the design specifications defined by the weighting functions. The existence of a stabilizing controller K is ensured by the satisfaction of the following conditions:

- The pair (A, B_2) is stabilizable.
- The pair (A, C_2) is detectable.

These conditions are satisfied as the system that results from the series connection of the actuator model and the plant model ($P_{22} = -GG_{sm}$) is controllable and observable (see Definition 4.3).

The controller synthesis is performed using the command `hinfsyn(·)` which computes the \mathcal{H}_∞ optimal controller [33]. The major characteristics of the resulting controller K for the signal-based \mathcal{H}_∞ optimal control problem are reported in Table 4-3. From Table 4-3, it is deduced that all the design specifications are satisfied as we have $\gamma < 1$. Furthermore, the order of the resulting controller equals the number of states in the plant $G(s)$ plus the number of states in the weighting functions, which is considered relatively low. It is important to mention that the controller is stable as the maximum real part of its eigenvalues is negative, i.e. lies in the LHP. The singular value plot of the resulting controller, as well as other useful plots, are presented in Section 4-7-2 in order to compare it with the controller obtained from the μ -synthesis problem in Section 4-6-2.

Table 4-3: Characteristics of the signal-based \mathcal{H}_∞ optimal controller

Number of states	γ	$\max(\text{Re}(\lambda(K)))$
24	0.35	$-4.95 \cdot 10^{-5}$

4-5 Characterization of Uncertainties

4-5-1 Introduction to Robustness

A control system is considered robust if it remains stable and it obeys specific performance criteria in the presence of possible uncertainties [17]. These uncertainties originate from differences between the actual system and the dynamical model used for the control design. These differences are referred to as model/plant mismatch or just model uncertainty. The fundamental idea in \mathcal{H}_∞ robust control is to examine whether the design specifications are satisfied even for the "worst-case" uncertainty. It is worth noting that model uncertainty is not the only concern for robustness. Other concerns include sensor and actuator failures, physical constraints, changes in control objectives, etc. Nevertheless, when we refer to robustness in terms of control design in this thesis project, we mean robustness with respect to model uncertainty [44].

In order to consider the model uncertainty, we can suppose that the dynamic behaviour of a plant is described not by a single LTI model but by a set Π of possible LTI models, sometimes denoted as the "uncertainty set". For the description of these definitions, we use the following notation:

- Π - a set of possible perturbed plant models.
- $G(s) \in \Pi$ - nominal plant model (with no uncertainty).

$G_p(s) \in \Pi$ - perturbed plant model (includes uncertainty).

The "norm-bounded uncertainty description" is used, where the set Π is generated by allowing \mathcal{H}_∞ norm-bounded stable perturbations to the nominal plant $G(s)$. This corresponds to a continuous description of the model uncertainty, which leads to an infinite number of possible plants G_p in the set Π . In order to explain the resulting model of the perturbed plant, let us denote E a perturbation which is not normalized, and Δ a normalized perturbation ($\|\Delta\|_\infty \leq 1$). Hence, instead of considering a single model G , we can study the behaviour of a class of models, $G_p = G + E$, where the model "uncertainty" or "perturbation" is bounded, however is unknown. Common weighting matrices $w(s)$ are used to express $E = w\Delta$ in terms of normalized perturbations Δ .

4-5-2 Representing Uncertainties

Generally, the different sources of model uncertainty are classified into two main categories:

1. **Parametric (real) uncertainty:** The structure and the order of model are known, however the model has some uncertain parameters.
2. **Dynamic (frequency-dependent) uncertainty:** The model include uncertainty because of missing dynamics, mostly at high frequencies, either due to neglected dynamics or due to lack of understanding of the physical process. This source of uncertainty is included almost in any dynamical model of a real system.

Parametric uncertainty is sometimes called *structured uncertainty* as it models the uncertainty in a structured manner. Analogously, dynamic uncertainty is sometimes called *unstructured uncertainty*. However, one should be careful about using these terms because there can be several levels of structure, especially for MIMO systems.

In this work, we consider the source of uncertainty for the HEARP system that originates from the deviation of its parameters from their actual values, due to errors in their estimation, nonlinearities, and changes in the operating conditions. Regarding the plant model G and the disturbance model G_d there are in total 15 uncertain parameters (see Table 3-2, Table 3-3 and Table 3-5), namely: m , I_x , I_{xy} , I_y , U_0 , C_{L0} , $C_{L\alpha}$, C_{D0} , $C_{D\alpha}$, $l_{x_j}^f$, $l_{x_j}^a$, l_y^f , l_y^{ap} , l_y^{as} , l_{z_j} . Moreover the actuator model G_{sm} has 3 uncertain parameters (see Table 3-5), namely: τ_δ^f , τ_δ^{ap} , τ_δ^{as} . Note that the perturbed systems that include the real parametric uncertainty are denoted by the subscript p , i.e. G_p , $G_{d,p}$ and $G_{sm,p}$.

To introduce a general procedure for handling parametric uncertainty that is suitable for numerical calculations, consider an uncertain state-space model

$$\dot{x} = A_p x + B_p u \quad (4-19a)$$

$$y = C_p x + D_p u \quad (4-19b)$$

Assume that the state-space matrices of Eq. (4-19) have uncertainty in some real parameters $\delta_1, \delta_2, \dots$ and assume in the simplest case that they depend linearly on these parameters, i.e.

$$A_p = A + \sum \delta_i A_i, \quad B_p = B + \sum \delta_i B_i, \quad C_p = C + \sum \delta_i C_i, \quad D_p = D + \sum \delta_i A D_i, \quad (4-20)$$

where A, B, C and D are the matrices that describe the nominal plant. This description has multiple perturbations, so a single perturbation cannot represent it. Nevertheless, we can

separate out the perturbations affecting A, B, C and D , and then collect them in a large diagonal matrix Δ with the real δ_i 's along its diagonal. Note that some of the δ_i 's may have to be repeated. Furthermore, note that seemingly nonlinear parameter dependencies, such as δ_1^2 and $\delta_1 \cdot \delta_2$ may be rewritten in the standard linear block diagram form, which leads to repetition of the parameters. The procedure handle the nonlinear parameter dependencies analytically is quite complicated and it lies outside the scope of this thesis. In practice it can be done automatically with available software [44].

For defining all the parametric uncertainties, the Matlab function `ureal`(\cdot) is used [33]. Furthermore with the use of Matlab function `lftdata`(\cdot) [33], we can decompose all the uncertain parameters into fixed certain and normalized uncertain parts. For the systems G and the G_d , this method leads to a very complicated representation of their perturbed versions because of the many nonlinear parameter dependencies present in the matrices of Eq. (3-7) (see Appendix A to realise the amount of these nonlinear parameter dependencies). Using the resulting representation of the perturbed systems, it is possible to perform simulations and frequency response analyses, despite the expensive computational cost. Nevertheless, regarding the controller synthesis, the problem is not solvable with a normal computer because of the enormous size of the required computations.

Hence, it is decided to represent the parametric uncertainty by complex perturbations for all systems (G_p , $G_{d,p}$ and $G_{sm,p}$). Because the representation of uncertainty in the frequency domain is much simpler, this approach has the advantage of the significant simplification of the analysis and especially the controller synthesis. The drawback of this approach is that it may be conservative as it introduces possible plants that are not present in the original set. The methodology to implement this approach is introduced below.

4-5-3 Approximating parametric uncertainty by complex perturbations

One of the most frequently used forms of uncertainty is the multiplicative uncertainty which may be represented by the block diagram in Figure 4-5, and its equation is given by:

$$\Pi_I : G_p(s) = G(s)(1 + w_I(s)\Delta_I(s)); \quad \underbrace{|\Delta_I(j\omega)| \leq 1}_{\|\Delta_I\|_\infty \leq 1} \forall \omega$$

where $\Delta_I(s)$ can be any stable transfer function which at each frequency has a magnitude less than or equal to 1. $\Delta_I(s)$ can be defined using the Matlab function `ultidyn`(\cdot). Additionally, $w_I(s)$ is a rational transfer function. The subscript I denotes "input", which is relevant for MIMO systems, while for SISO systems, it does not matter whether we consider the perturbation at the input or output of the plant.

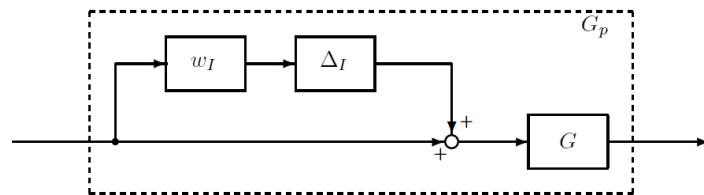


Figure 4-5: Plant with multiplicative uncertainty [44]

To explain how to obtain the weighting function $w_I(s)$, consider a SISO system with a nominal plant $G(s) \in \Pi$ and a perturbed plant $G_p \in \Pi$. Here Π is the set of all possible perturbed plants that result from parametric uncertainty. We want to describe this set of plants by a single (lumped) complex perturbation, Δ_I . To achieve this, at each frequency we find the smallest radius $l_I(\omega)$ that includes the maximum relative error between $G(s)$ and G_p . This radius is given by:

$$l_I(\omega) = \max_{G_p \in \Pi} \left| \frac{G_p(j\omega) - G(j\omega)}{G(j\omega)} \right| \quad (4-21)$$

Subsequently, the weighting function $w_I(s)$ is chosen as a rational transfer function that covers the set:

$$|w_I(j\omega)| \geq l_I(\omega) \quad \forall \omega \quad (4-22)$$

One may also view $w_I(s)$ as a weight introduced to normalize the perturbation to be less than 1 in magnitude at each frequency. Therefore only the magnitude of the weight matters, and to avoid unnecessary problems, $w_I(s)$ is chosen to be stable and minimum-phase (no RHP poles, no RHP zeros and no delays). Additionally, $w_I(s)$ is also selected to be of low order to simplify the controller design [44].

A finite set Π of possible perturbed plants can be obtained by generating a finite number of random samples of G_p using the Matlab function `usample(.)` [33]. Next, using the frequency responses of G and G_p for a finite range of frequencies $\omega_{\min} \leq \omega \leq \omega_{\max}$, the weighting function $w_I(s)$ can be constructed by the Matlab function `ucover(.)` [33]. Note that the range of frequencies should be chosen sufficiently large to capture all variations of the magnitude of the frequency response of G .

Regarding the MIMO systems, the aforementioned methodology can be implemented by finding a scalar transfer function $w_{I,ij}(s)$ for each element of the transfer function matrix. This transfer function captures the maximum relative error (see Eq. (4-21) and Eq. (4-22)) between g_{ij} and g_{pij} . The scalar models obtained are then combined in a transfer matrix in order to determine the uncertainty model of the MIMO plant. Consider, for example, the model of a two-input, two-output uncertain plant with transfer function matrix:

$$G_p(s) = \begin{bmatrix} g_{p,11}(s) & g_{p,12}(s) \\ g_{p,21}(s) & g_{p,22}(s) \end{bmatrix}$$

where $g_{p,ij}(s)$ are scalar transfer function containing uncertainty. These transfer functions are represented by the corresponding models that approximate the maximum error of each element separately. If a multiplicative uncertainty model represents each element, the model of the whole system is obtained as

$$G_p^a(s) = \begin{bmatrix} g_{11}(s)(1 + w_{I,11}(s)\delta_{I,11}) & g_{12}(s)(1 + w_{I,12}(s)\delta_{I,12}) \\ g_{21}(s)(1 + w_{I,21}(s)\delta_{I,21}) & g_{22}(s)(1 + w_{I,22}(s)\delta_{I,22}) \end{bmatrix} \quad (4-23)$$

where $g_{ij}(s)$ are nominal transfer functions, $w_{I,ij}(s)$ are the weighting functions obtained after approximation and $\delta_{I,ij}$ are complex scalar uncertainties [17].

Thus, the aim is to implemented this approach to the perturbed systems G_p , $G_{d,p}$ and $G_{sm,p}$ that include the real parametric uncertainties. Initially, the weighting functions that cover the relative error of each channel of the transfer function matrices are obtained using the method that is described at the beginning of Section 4-5-3 (using the functions `usample(.)`)

and `ucover(·)`). After an iterative procedure, the order of the weighting functions for each channel of G and G_d is chosen as 3, while for G_{sm} is chosen as 1. Furthermore, after another iterative procedure, the number of random samples used for each case is chosen to be equal to 100. It was observed that this amount of random samples can give repetitive results for the weighting functions. This implies that the largest error (worst-case uncertainties) of the frequency responses of the systems are most likely included in the generated finite set of the perturbed systems. Note that a larger number of random samples increases the computational cost considerably without finding uncertainties leading to the largest error.

The results of this procedure are illustrated by the frequency responses of the relative error between the nominal and the perturbed systems that are shown in Figure 4-6, Figure 4-7 and Figure 4-8. Note that for the system G_{sm} there is only one frequency response because its block-diagonal form with equal g_{sm}^i . From the results of Figure 4-6, Figure 4-7 and Figure 4-8 it is observed that all the scalar transfer functions $w_{I,G^{ij}}$, $w_{I,G_d^{ij}}$ and w_{I,G_{sm}^i} cover accurately their corresponding relative errors for all channels for all systems.

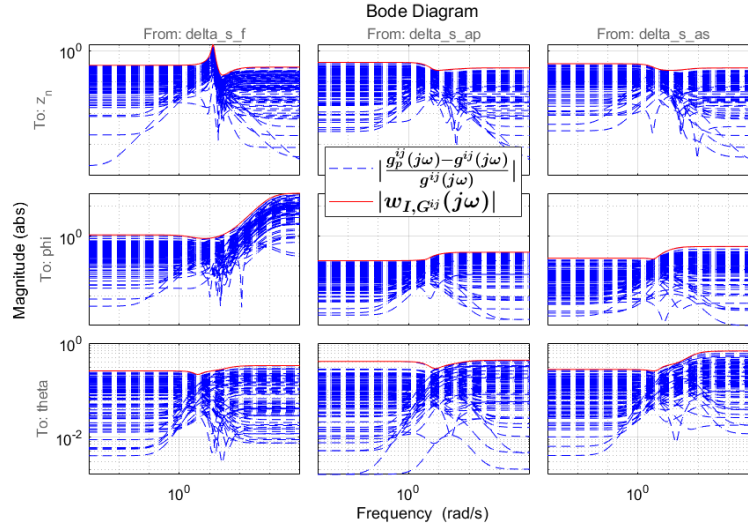


Figure 4-6: Frequency responses of the relative error between the nominal and the perturbed systems for each channel of G

The next step is to formulate the approximated perturbed systems G_p^a , $G_{d,p}^a$ and $G_{sm,p}^a$ using the form of Eq. (4-23). Note that the superscript a denotes the approximated perturbed systems with the multiplicative uncertainty. After different tries, it is observed that when the form of Eq. (4-23) is used to construct the generalized plant for the system with uncertainties (see Section 4-6), different issues occur during the implementation of μ -synthesis algorithm. More precisely, the K -step of the DK -iteration algorithm in order to be solvable, requires that the pair (A, B_2) is stabilizable and the pair (A, C_2) is detectable (see Eq. (4-18)). In order to satisfy this condition, it is required to use the minimal realization of the generalized plant that includes the weighting functions of the multiplicative uncertainties for each of the approximated perturbed systems. However, by using the minimal realization, other numerical issues arise, and the stabilizability and the detectability conditions are again violated. Hence, using this uncertainty modelling, it was not possible to use the μ -synthesis algorithm to design the robust optimal controller.

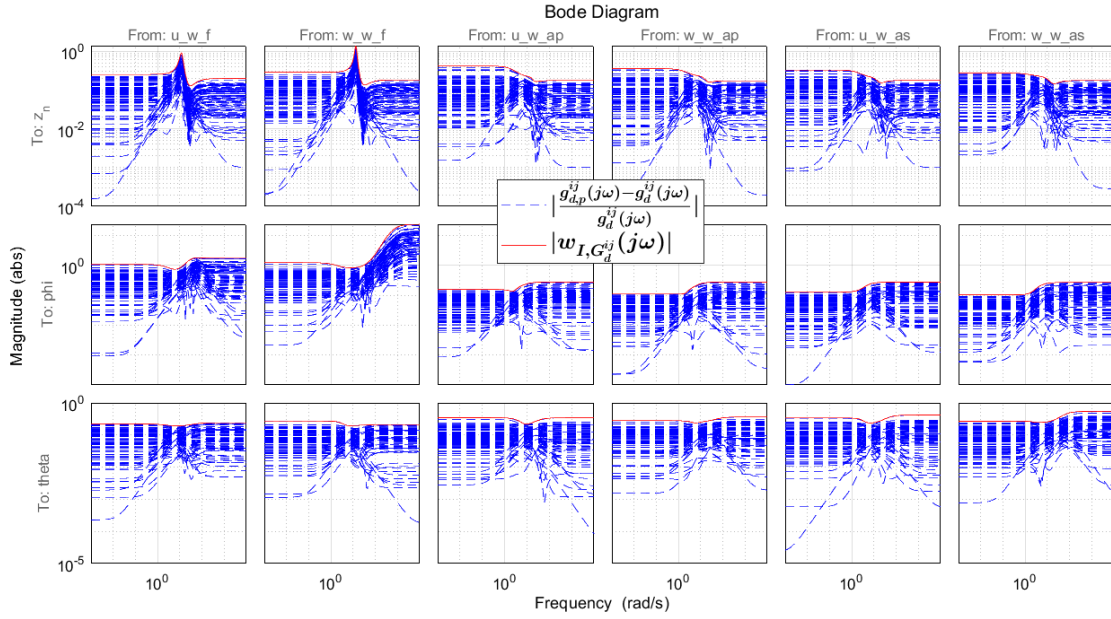


Figure 4-7: Frequency responses of the relative error between the nominal and the perturbed systems for each channel of G_d

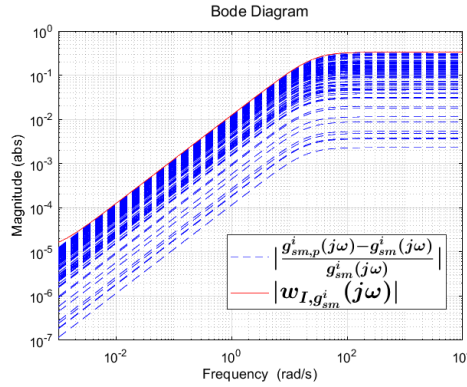


Figure 4-8: Frequency response of the relative error between the nominal and the perturbed systems for g_{sm}^i

To resolve the issues mentioned above, we followed different approaches, including the use of the form of additive uncertainties for MIMO systems (see Section 4.2.5 of [43] for more information). After this iterative procedure, it is decided to use the standard equation of the multiplicative input uncertainties for MIMO systems that is given by:

$$\Pi_I : G_p^a(s) = G(s)(1 + \Delta_I(s)W_I(s)) \tag{4-24}$$

where $W_I(s)$ and Δ_I are full matrices that are constructed by combining the scalar weighting functions $w_{I,ij}(s)$ and the complex scalar uncertainties $\delta_{I,ij}$ of each individual channel respectively. It was observed that this approach gives the best results in terms of the accuracy of the approximation of the parametric uncertainties by complex perturbations.

The drawback of this approach is that the accuracy of the approximation for G_p^a and $G_{d,p}^a$ (full transfer function matrices) is relatively poor for some frequency ranges. This results

from the fact that each channel of the perturbed system G_p^a of Eq. (4-24) includes weighting functions and perturbations from different channels because of the matrix multiplications. To compensate for this "error" of the approximation, the maximum magnitude of Δ_I for G_p^a and $G_{d,p}^a$ instead of 1 is selected to have a lower value. This value is tuned iteratively to maximize the accuracy of the approximation. Note that the aforementioned problem does not occur for the case of $G_{sm,p}^a$ because it has a block-diagonal form. Finally, the approximated perturbed systems G_p^a , $G_{d,p}^a$ and $G_{sm,p}^a$ are formulated as in Eq. (4-25), Eq. (4-26) and Eq. (4-27) respectively.

$$G_p^a(s) = G(s)(I_3 + \Delta_{I,G}(s)W_{I,G}(s)) \quad (4-25a)$$

$$W_{I,G}(s) = \begin{bmatrix} w_{I,G^{11}} & w_{I,G^{12}} & w_{I,G^{13}} \\ w_{I,G^{21}} & w_{I,G^{22}} & w_{I,G^{23}} \\ w_{I,G^{31}} & w_{I,G^{32}} & w_{I,G^{33}} \end{bmatrix} \quad (4-25b)$$

$$\Delta_{I,G}(s) \in \mathbb{C}^{3 \times 3} \text{ (full complex perturbation matrix); } \|\Delta_{I,G}(j\omega)\|_\infty \leq b_G = 0.5, \forall \omega \quad (4-25c)$$

where the scalar weighting functions for each channel $w_{I,G^{ij}}$ are obtained from Figure 4-6 and their numerical values are given in Eq. (B-4). Additionally, b_G denotes the upper bound on the magnitude of $\Delta_{I,G}$, and it is used to "tune" the accuracy of the approximation. It is chosen at 0.5 after an iterative procedure.

$$G_{d,p}^a(s) = G_d(s)(I_6 + \Delta_{I,G_d}(s)W_{I,G_d}(s)) \quad (4-26a)$$

$$W_{I,G_d}(s) = \begin{bmatrix} w_{I,G_d^{11}} & w_{I,G_d^{12}} & w_{I,G_d^{13}} & w_{I,G_d^{14}} & w_{I,G_d^{15}} & w_{I,G_d^{16}} \\ w_{I,G_d^{21}} & w_{I,G_d^{22}} & w_{I,G_d^{23}} & w_{I,G_d^{24}} & w_{I,G_d^{25}} & w_{I,G_d^{26}} \\ w_{I,G_d^{31}} & w_{I,G_d^{32}} & w_{I,G_d^{33}} & w_{I,G_d^{34}} & w_{I,G_d^{35}} & w_{I,G_d^{36}} \end{bmatrix} \quad (4-26b)$$

$$\Delta_{I,G_d}(s) \in \mathbb{C}^{6 \times 6} \text{ (full complex perturbation matrix); } \|\Delta_{I,G_d}(j\omega)\|_\infty \leq b_{G_d} = 0.5, \forall \omega \quad (4-26c)$$

The scalar weighting functions for each channel $w_{I,G_d^{ij}}$ are obtained from Figure 4-7 and their numerical values are given in Eq. (B-5). Additionally, b_{G_d} denotes the upper bound on the magnitude of $\Delta_{I,G}$, and it is used to "tune" the accuracy of the approximation. It is chosen at 0.5 after an iterative procedure.

$$G_{sm,p}^a(s) = G_{sm}(s)(I_3 + \Delta_{I,G_{sm}}(s)W_{I,G_{sm}}(s)) \quad (4-27a)$$

$$W_{I,G_{sm}}(s) = \begin{bmatrix} w_{I,G_{sm}^1} & 0 & 0 \\ 0 & w_{I,G_{sm}^2} & 0 \\ 0 & 0 & w_{I,G_{sm}^3} \end{bmatrix} \quad (4-27b)$$

$$\Delta_{I,G_{sm}}(s) = \text{diag}\{\delta_{G_{sm}^i}\}, i = \{1, 2, 3\}; |\delta_{G_{sm}^i}(j\omega)| \leq 1, \forall \omega, \forall i \quad (4-27c)$$

The scalar weighting function for each diagonal channel w_{I,G_{sm}^i} is obtained from Figure 4-8 and its numerical value is given in Eq. (B-6).

To validate qualitatively the accuracy of the approximation of the parametric uncertainties by complex perturbations for the three systems, we use 20 random realizations of the singular

value plots of all systems. The results are shown in Figure 4-9. Recall that the systems G_p , $G_{d,p}$ and $G_{sm,p}$ correspond to the real parametric uncertainty, while the systems G_p^a , $G_{d,p}^a$ and $G_{sm,p}^a$ correspond to the approximated perturbed systems by the multiplicative input uncertainty.

From Figure 4-9a and Figure 4-9b, it is observed that the variations of the singular values for the approximated perturbed systems match quite well with the corresponding variations of the actual perturbed systems. Nevertheless, it can be seen that the variations of the smallest singular value are quite large for the approximated perturbed systems with respect to the actual perturbed systems. Regarding the actuator model in Figure 4-9c, it is deduced that the approximation of the uncertainties is very accurate for all the frequency ranges.

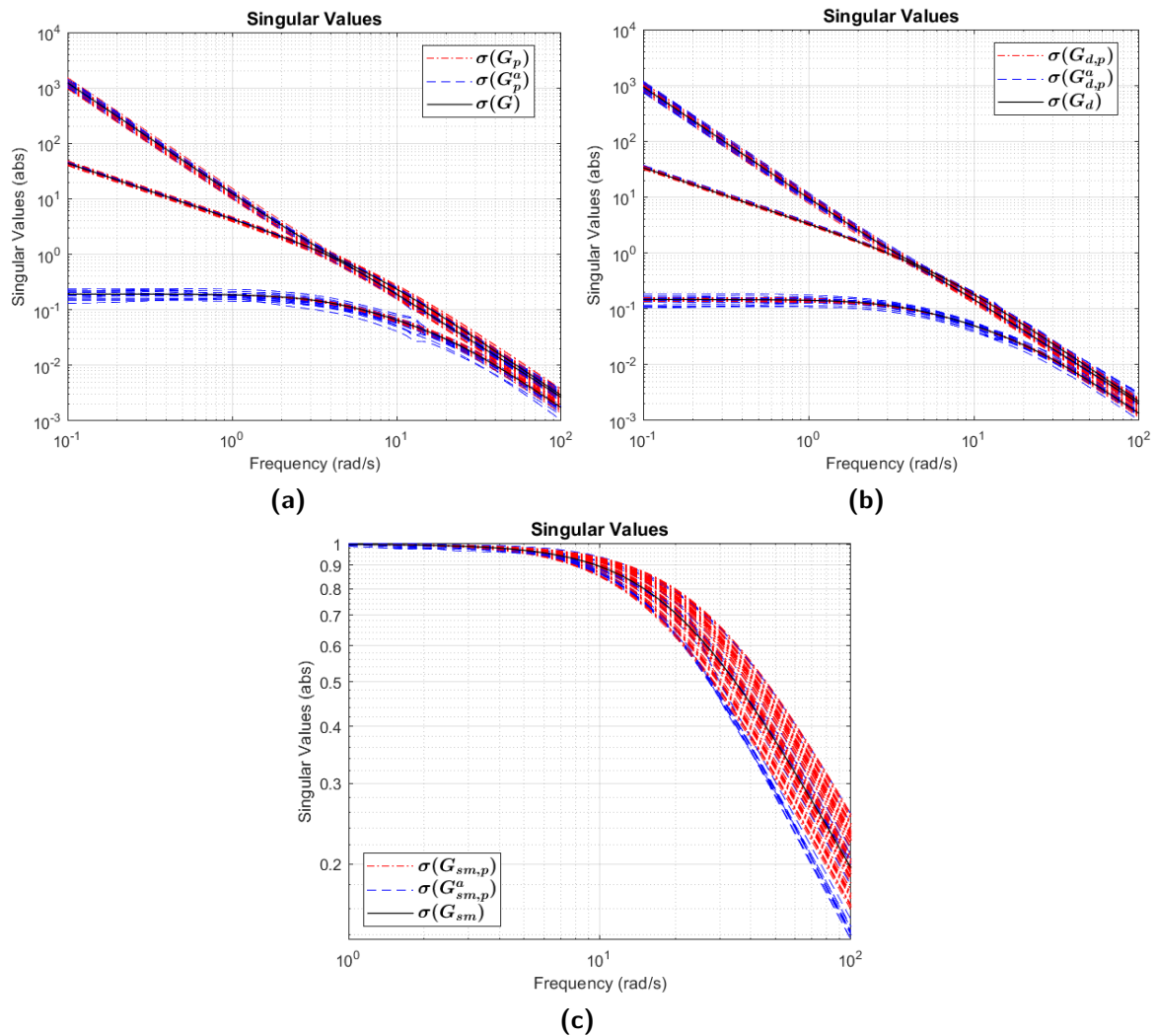


Figure 4-9: Singular value plots of the perturbed systems with the real parametric uncertainty and the approximated perturbed systems with the multiplicative input uncertainty

Overall, it is concluded that the chosen method for approximating the parametric uncertainty by complex perturbations using the form of the multiplicative input uncertainty, leads to satisfactory results. Therefore, the resulting approximated perturbed systems (see Eq. (4-

25), Eq. (4-26) and Eq. (4-27)) are used for the design of the μ -synthesis robust controller.

4-6 Optimal robust control design using μ -synthesis

The objective of this section is to present an optimal robust controller in terms of minimizing μ (structured singular value), which is designed using the DK-iteration algorithm. This involves solving a sequence of scaled \mathcal{H}_∞ problems like in Eq. (4-18) [44]. Note that this control design uses the same design weights as the design of the signal-based \mathcal{H}_∞ optimal controller (see Section 4-4-2).

4-6-1 Configuration of the Generalized Plant

The μ -synthesis control design methodology is formulated as shown by the block diagram of Figure 4-10. This formulation uses the general control configuration with uncertainty, where P is the generalized plant, K is the generalized controller, and Δ is a block-diagonal matrix that includes all the sources of uncertainty. Using the modelled uncertainties presented in Section 4-5, the transfer function matrix Δ is formulated as:

$$y_\Delta = \Delta u_\Delta \implies \begin{bmatrix} y_{\Delta_{G_{sm}}} \\ y_{\Delta_G} \\ y_{\Delta_{G_d}} \end{bmatrix} = \begin{bmatrix} \Delta_{I,G_{sm}} & O_{3 \times 3} & O_{3 \times 3} \\ O_{3 \times 3} & \Delta_{I,G} & O_{3 \times 3} \\ O_{6 \times 3} & O_{6 \times 3} & \Delta_{I,G_d} \end{bmatrix} \begin{bmatrix} u_{\Delta_{G_{sm}}} \\ u_{\Delta_G} \\ u_{\Delta_{G_d}} \end{bmatrix} \quad (4-28)$$

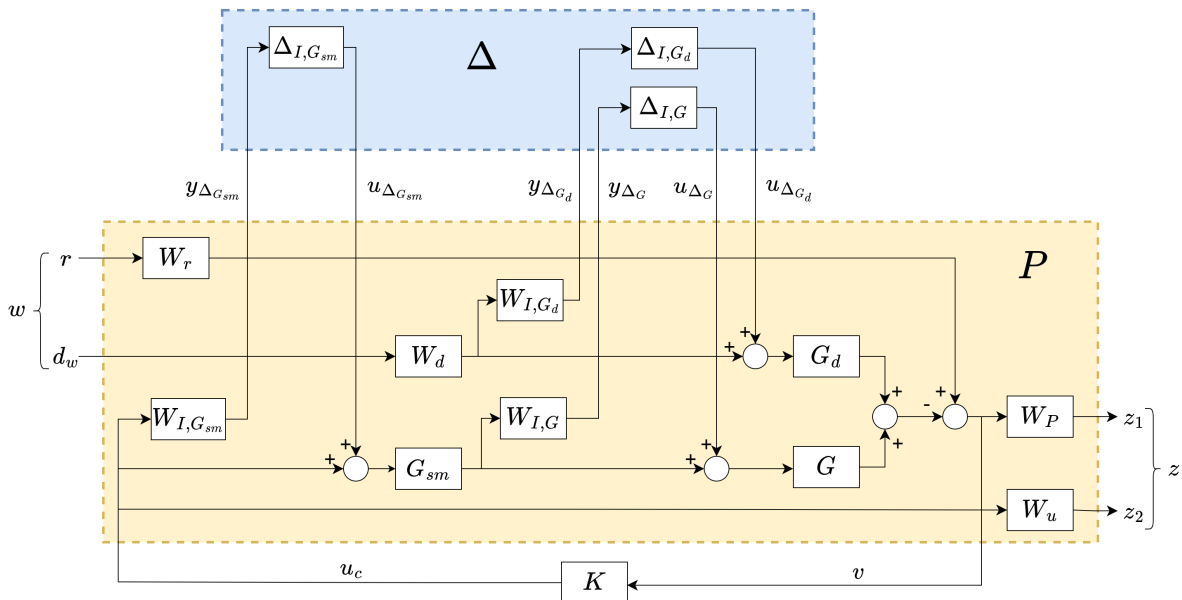


Figure 4-10: Block diagram of signal-based μ -synthesis optimal control problem for the perturbed plant

Most of the different components and the signals of the block diagram in Figure 4-10 have the same definition as the corresponding components and signals of the block diagram in

Figure 4-3. The additional components of the block diagram in Figure 4-10 are the weighting transfer function matrices of the multiplicative input uncertainties (see Eq. (4-25), Eq. (4-26) and Eq. (4-27)) and their corresponding input-output signals.

The equations of the output signals as a function of the input signals for the block diagram of Figure 4-10 are given by:

$$\begin{aligned}
 y_{\Delta_{G_{sm}}} &= W_{I,G_{sm}} u_c \\
 y_{\Delta_G} &= W_{I,G} G_{sm} u_{\Delta_{G_{sm}}} + W_{I,G} G_{sm} u_c \\
 y_{\Delta_{G_d}} &= W_{I,G_d} W_d d_w \\
 z_1 &= -W_P G u_{\Delta_G} - W_P G_d u_{\Delta_{G_d}} + W_P W_r r - W_P G_d W_d d_w - W_P G G_{sm} u_c \\
 z_2 &= W_u u_c \\
 v &= -G u_{\Delta_G} - G_d u_{\Delta_{G_d}} + W_r r - G_d W_d d_w - G G_{sm} u_c
 \end{aligned}$$

So the generalized plant P is a transfer function matrix with dimensions 18×24 and has the following structure:

$$\begin{bmatrix} y_{\Delta_{G_{sm}}} \\ y_{\Delta_G} \\ y_{\Delta_{G_d}} \\ z_1 \\ z_2 \\ v \end{bmatrix} = \underbrace{\begin{bmatrix} O_{3 \times 3} & O_{3 \times 3} & O_{3 \times 6} & O_{3 \times 3} & O_{3 \times 6} & W_{I,G_{sm}} \\ W_{I,G} G_{sm} & O_{3 \times 3} & O_{3 \times 6} & O_{3 \times 3} & O_{3 \times 6} & W_{I,G} G_{sm} \\ O_{3 \times 3} & O_{3 \times 3} & O_{3 \times 6} & O_{3 \times 3} & W_{I,G_d} W_d & O_{3 \times 3} \\ O_{3 \times 3} & -W_P G & -W_P G_d & W_P W_r & -W_P G_d W_d & -W_P G G_{sm} \\ O_{3 \times 3} & O_{3 \times 3} & O_{3 \times 6} & O_{3 \times 3} & O_{3 \times 6} & W_u \\ O_{3 \times 3} & -G & -G_d & W_r & -G_d W_d & -G G_{sm} \end{bmatrix}}_{P(s)} \begin{bmatrix} u_{\Delta_{G_{sm}}} \\ u_{\Delta_G} \\ u_{\Delta_{G_d}} \\ r \\ d_w \\ u_c \end{bmatrix} \quad (4-29)$$

The generalized plant P in Eq. (4-29) is constructed using the Matlab function `connect()` [33].

4-6-2 Controller Synthesis

The overall control objective of the optimal robust controller is to minimize the norm of the transfer function matrix $F(N, \Delta)$ from w to z (see Figure 4-11) in the presence of the worst-case uncertainties Δ . Note that the structure with individual blocks for the generalized plant P , the controller K and the uncertainty Δ as it is shown in Figure 4-11, is useful for the controller synthesis. Alternatively, if the controller is given and we want to analyse the uncertain system, we use the so-called $N\Delta$ -structure in which the closed-loop block N with the uncertainty Δ are used (see Figure 4-11) [44].

The generalized plant in Figure 4-11 is described by:

$$\begin{bmatrix} y_{\Delta} \\ z \\ v \end{bmatrix} = \begin{bmatrix} P_{11}(s) & P_{12}(s) \\ P_{21}(s) & P_{22}(s) \end{bmatrix} \begin{bmatrix} u_{\Delta} \\ w \\ u_c \end{bmatrix} \quad (4-30)$$

with a state-space realization of the generalized plant P given by Eq. (4-16).

The result of Eq. (4-30) is obtained by partitioning the generalized plant P of Eq. (4-29) such that its parts are compatible with the signals y_{Δ} , z , v , u_{Δ} , w and u_c . More precisely, the

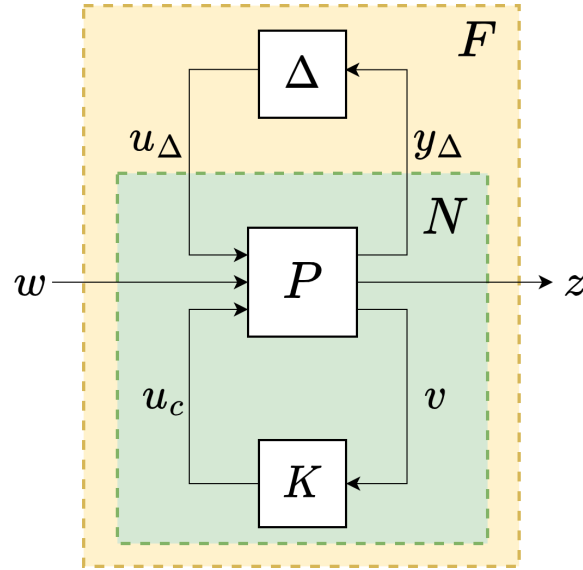


Figure 4-11: General control configuration for the case that includes model uncertainty [44]

parts have dimensions: P_{11} : 15×21 , P_{12} : 15×3 , P_{21} : 3×21 and P_{22} : 3×3 . Note here that P_{22} has the same dimensions and structure as for the case of the nominal system (see Eq. (4-9)).

The closed-loop system N is derived by using a lower linear fractional transformation (LFT) of P with K as the parameter, as shown in Eq. (4-17). To evaluate the perturbed (uncertain) transfer function F from external inputs w to z , we use Δ to close the upper loop around N (see Figure 4-11), resulting in an upper LFT:

$$F = F_u(N, \Delta) \triangleq N_{22} + N_{21}\Delta(I - N_{11}\Delta)N_{12} \quad (4-31)$$

The derivation of N from P and K , and F from N and Δ is done using the Matlab function `lft`(\cdot) [33]. Note that for the μ -synthesis problem, N has dimensions 15×21 while F has dimensions 6×9 .

As it was mentioned before, the structured singular value μ (see Definition 4.5) is a very powerful tool for analysing the conditions RS and RP of a given controller. Nevertheless, one may also seek to find the controller that minimizes a given μ condition: this is the μ -synthesis problem. Currently, there is no direct method to efficiently synthesise a μ -optimal robust controller. However, the method known as DK -iteration is available for complex perturbations. It combines \mathcal{H}_∞ synthesis, and μ -analysis and often yields good results. The starting point is the upper bound on μ in terms of the scaled singular value:

$$\mu(N) \leq \min_{D \in \mathcal{D}} \bar{\sigma}(DND^{-1})$$

The idea is to find the controller that minimises the peak value over frequency of this upper bound, namely

$$\min_K \left(\min_{D \in \mathcal{D}} (\|DN(K)D^{-1}\|_\infty) \right)$$

by alternating between minimizing $\|DN(K)D^{-1}\|_\infty$ with respect to either K or D (while holding the other fixed). To start the iterations, one selects an initial stable rational transfer matrix $D(s)$ with the appropriate structure. The DK -iteration then proceeds as follows:

1. **K-step:** Synthesize an \mathcal{H}_∞ controller for the scaled problem, $\min_K(\|DND^{-1}\|_\infty)$ with fixed $D(s)$.
2. **D-step:** Find $D(j\omega)$ to minimize at each frequency $\bar{\sigma}(DND^{-1}(j\omega))$ with fixed N .
3. Fit the magnitude of each element of $D(j\omega)$ to a stable and minimum-phase transfer function $D(s)$ and go to step 1.

The iteration may continue until satisfactory performance is achieved, $\|DND^{-1}\|_\infty \leq 1$, or until the \mathcal{H}_∞ norm no longer decreases. One fundamental problem with this approach is that although each minimisation step (K -step and D -step) is convex, joint convexity is not guaranteed. Therefore, the iterations may converge to a local optimum. However, practical experience suggests that the method works well in most cases.

The controller's order resulting from each iteration is equal to the number of states in the plant $G(s)$ plus the number of states in the weights plus twice the number of states in $D(s)$. For most cases, the true μ -optimal controller is not rational and will thus be of infinite order, but because we use a finite-order $D(s)$ to approximate the D -scales, we get a controller of finite (but often high) order.

Recall that if μ at a given frequency is less than 1, then the interpretation is that at this frequency, we can tolerate $1/\mu$ -times more uncertainty and satisfy our performance objective with a margin of $1/\mu$. In μ -synthesis, the designer commonly has to adjust some parameter(s) in the performance or uncertainty weighting function until the peak μ -value is close to 1. Because usually the uncertainty is fixed, the parameters of the performance weighting functions are adjusted.

To design the μ -synthesis optimal robust controller with the DK -iteration algorithm, we use the Matlab function `musyn`(\cdot) [33]. The key characteristics of the resulting controller K for the μ -synthesis optimal robust control problem are reported in Table 4-4. From Table 4-4, it is deduced that all the design specifications are satisfied up to a satisfactory extent, and also, the controller is robust for the modelled uncertainty as the value of μ is quite close to 1. In addition, the order of the resulting controller equals the number of states in the plant $G(s)$ plus the number of states in the weighting functions plus twice the number of states in $D(s)$. As it is expected, the order of the controller is quite high.

With the aim to reduce the complexity and the computation cost of the resulting controller, we use an order-reduction method (see Section 4-6-3). In that way, it can be implemented more easily to the available hardware and software on HEARP. Lastly, the controller is again stable as the maximum real part of its eigenvalues is negative, i.e. lies in the LHP. The singular value plot of the resulting controller, as well as other useful plots, are presented at the end of the chapter in order to compare it with the controller obtained from the signal-based \mathcal{H}_∞ problem in Section 4-4-3.

Table 4-4: Characteristics of the μ -synthesis optimal robust controller

Number of states	μ	$\max(\text{Re}(\lambda(K)))$
199	1.13	$-5.00 \cdot 10^{-4}$

4-6-3 Controller Order-Reduction

Modern controller design methods such as \mathcal{H}_∞ and μ -synthesis produce controllers of order at least equal to that of the plant and usually higher because of the inclusion of weighting functions and the scaling functions (for μ -synthesis). However, these control laws may be too complex for practical implementation because of their high computational cost. Hence, simpler designs with low-order controllers are preferred by control engineers. In general, there are three approaches to obtaining a low-order controller for a relatively high-order plant [17]:

1. Plant model reduction followed by controller design.
2. Controller design followed by controller-order reduction.
3. Direct design of low-order controllers.

For the specific problem of the μ -synthesis, the high order of the resulting controller is unavoidable, even though the order of the plant is relatively low (equal to six). Considering the implemented method for the controller design, it is decided that the most suitable and simplest approach to obtain a low-order controller is the second one. The main goal of this approach is to find a low-order approximation K_a of the given a high-order LTI stable model K , such that the infinity norm \mathcal{H}_∞ of the error $\|K - K_a\|_\infty$ is sufficiently small. Note that by model order, we mean the dimension of the state vector in a minimal realization, i.e. the McMillan degree (see Definition 4.4). To tackle the problem of controller-order reduction, different methods exist. Each of the existing methods gives a stable approximation and a guaranteed bound on the error in the approximation. This study uses the *balanced truncation* method that is found in [44], which is introduced briefly next.

Balanced realization

Firstly, let (A, B, C, D) be a minimal realization of the stable and rational transfer function of the controller $K(s)$. Then (A, B, C, D) is called *balanced* if the solutions to the following Lyapunov equations

$$\begin{aligned} AP + PA^T &= -BB^T \\ A^T Q + QA &= -C^T C \end{aligned}$$

satisfy $P = Q = \text{diag}(\sigma_1, \sigma_2, \dots, \sigma_n) \triangleq \Sigma$, where $\sigma_1 \geq \sigma_2 \geq \dots \geq \sigma_n > 0$. Note that P and Q define the observability and controllability Gramians of the controller. Henceforth, Σ is simply referred to as the Gramian of $K(s)$. The σ_i 's are the ordered Hankel singular values of $K(s)$, and they are generally defined as:

$$\sigma_i = \sqrt{\lambda_i(PQ)}$$

In a balanced realization, the value of each σ_i is associated with a state x_i of the balanced system. The size of σ_i is a relative measure of the contribution that x_i makes to the input-output behaviour of the system. Therefore if $\sigma_1 \geq \sigma_2$, then the state x_1 affects the input-output behaviour more than x_2 , or any other state because of the ordering of the σ_i . This property is fundamental to the model reduction methods which work by removing states having negligible effect on the input-output behaviour of the system. It is worth noting that after balancing a system, each state is both controllable and observable.

Balanced truncation

Let the balanced realization (A, B, C, D) of $K(s)$ and the corresponding Σ be partitioned compatibly as

$$A = \begin{bmatrix} A_{11} & A_{12} \\ A_{21} & A_{22} \end{bmatrix}, \quad B = \begin{bmatrix} B_1 \\ B_2 \end{bmatrix}, \quad C = [C_1 \quad C_2], \quad \Sigma = \begin{bmatrix} \Sigma_1 & 0 \\ 0 & \Sigma_2 \end{bmatrix},$$

where $\Sigma_1 = \text{diag}(\sigma_1, \sigma_2, \dots, \sigma_k)$, $\Sigma_2 = \text{diag}(\sigma_{k+1}, \sigma_{k+2}, \dots, \sigma_n)$ and $\sigma_k \geq \sigma_{k+1}$.

Hence, the reduced order model of the controller K_a is given by (A_{11}, B_1, C_1, D) which is called a *balanced truncation* of the full-order system $K(s)$. This method discards the least controllable and observable states corresponding to Σ_2 . Assume that the selected order of the controller is equal to k and the order of the high-order controller K is equal to n . Then, the error in \mathcal{H}_∞ norm caused by deleting states in $K(s)$ is bounded by twice the sum of the discarded Hankel singular values, i.e.

$$\|K(s) - K_a^k(s)\|_\infty \leq 2 \sum_{k+1}^n \sigma_i \quad (4-32)$$

where $K_a(s)$ denotes a truncated balanced realization with k states.

The magnitude of the Hankel singular values can be used to determine the appropriate order size of the controller. To do so, the Matlab function `balreal`(\cdot) [33] is used firstly to obtain the balanced realization of the controller K and then the Matlab function `hankelsv`(\cdot) [33] is used to obtain the Hankel singular value plot. The resulting plot is illustrated in Figure 4-12a, and based on its results, the desired order of the controller k is selected as 40. Above this value, the magnitude of the Hankel singular values remains less than 10^{-2} ; thus, the approximation error remains sufficiently small.

Next, using the Matlab function `balancmr`(\cdot) [33], the balanced truncation of the controller with order 40 is obtained. The singular values of the resulting approximation error (see Eq. (4-32)) is shown in Figure 4-12b and the \mathcal{H}_∞ norm of the error equals to $\|K(s) - K_a^{40}(s)\|_\infty = 0.042$. From these results, it is deduced that the chosen method gives a quite accurate approximation of the controller with only 40 states instead of the 199 states of the initially designed controller (see Table 4-4). This definitely reduces the controller's complexity and computational cost when implemented on the HEARP. Note that the resulting reduced-order controller K_a^{40} for the μ -synthesis problem is used in Section 4-7 for the evaluation of the control design and in Chapter 5 for the time-domain simulations.

4-7 Evaluation of Control Designs

In this section, the designed controllers are evaluated with respect to their stability, performance and robustness using different measures and useful plots in the frequency domain. Initially, the standard conditions for evaluating stability and performance for the nominal and the perturbed systems are presented. Next, using different closed-loop transfer functions, the performance and the level of satisfaction of the design specifications of the designed controllers are compared in the frequency domain [44].

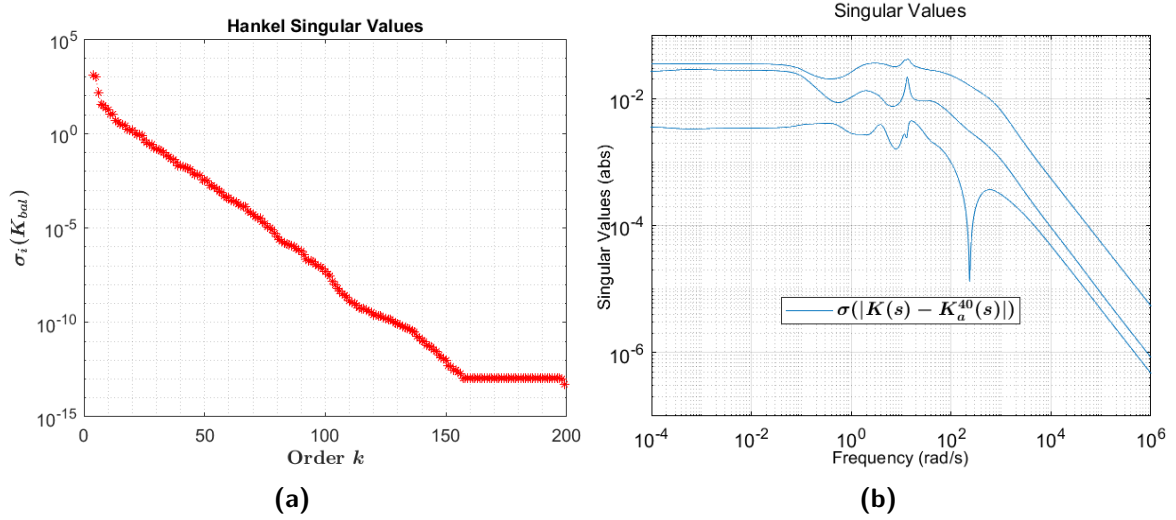


Figure 4-12: (a) Hankel singular values of the balanced realization of the μ -synthesis controller K_{bal} and (b) Singular values of the approximation error of the reduced-order controller

4-7-1 Stability and Performance Evaluation

To evaluate the stability and performance of different control designs, the following terms are commonly used:

- **Nominal Stability (NS):** The nominal system is stable.
- **Nominal Performance (NP):** The nominal system satisfies the performance specifications.
- **Robust Stability (RS):** The perturbed system is stable for the worst-case model uncertainty.
- **Robust Performance (RP):** The perturbed system satisfies the performance specifications for the worst-case model uncertainty.

The evaluation of the control designs requires to rearrange the uncertain system into an $N\Delta$ -structure (see Figure 4-11), where the block-diagonal perturbations satisfy $\|\Delta\|_\infty \leq 1$. Therefore, the extended generalized plant configuration (see Eq. (4-29)) that includes the weighting functions for the design specifications and the uncertainty representation is used to obtain the corresponding closed-loop transfer matrix N (see Eq. (4-17)) for each designed controller. Then the performance requirement (RP) is defined as $\|F\|_\infty \leq 1$ (see Eq. (4-31)). Recall that the structured singular value μ (see Definition 4.5) is a useful tool for evaluating the robustness of a designed controller. Then, for the evaluation of the stability and the performance of different control designs, the following conditions are used:

$$\text{NS} \implies N \text{ internally stable (see Definition 4.6)}$$

$$\text{NP} \implies \bar{\sigma}(N_{22}(j\omega)) < 1, \forall \omega, \quad \text{and NS}$$

$$\text{RS} \implies \mu_\Delta(N_{11}(j\omega)) < 1, \forall \omega, \quad \text{and NS}$$

$$\text{RP} \implies \mu_{\hat{\Delta}}(N(j\omega)) < 1, \forall \omega, \quad \hat{\Delta} = \begin{bmatrix} \Delta & 0 \\ 0 & \Delta_P \end{bmatrix} \quad \text{and NS}$$

where Δ is the block-diagonal matrix of uncertainty (see Eq. (4-28)) and Δ_P is a full complex perturbation matrix (of class `ultidyn`(·) [33]) representing the \mathcal{H}_∞ performance specification with the same dimensions as F^T (9×6). Note that NS must be tested independently for all the components of the closed-loop transfer matrix N .

Using the appropriate part of the closed-loop system N , NS is tested using the Matlab function `isstable`(·), NP is tested using the Matlab function `sigma`(·), and RS and RP are tested using the Matlab function `mussv`(·) [33]. Finally, the characteristics of the designed controllers about their stability and performance are reported in Table 4-5, while the same characteristics as a function of frequency are illustrated by Figure 4-13.

Table 4-5: Stability and performance characteristics of the designed controllers

Check	Criterion	Maximum value for \mathcal{H}_∞ controller	Maximum value for μ -synthesis controller
NS	N internally stable	Stable	Stable
NP	$\bar{\sigma}(N_{22}(j\omega)) < 1, \forall \omega,$	0.35	1.10
RS	$\mu_\Delta(N_{11}(j\omega)) < 1, \forall \omega,$	9.08	0.70
RP	$\mu_\Delta(N_{22}(j\omega)) < 1, \forall \omega,$	98.96	1.13

From the results of Table 4-5, it is seen that both controllers are internally stable, so they satisfy the condition for NS. Considering the NP condition, it is deduced that both controllers almost satisfy the criterion, while the \mathcal{H}_∞ controller achieves lower $\bar{\sigma}(N_{22}(j\omega))$ than the μ -synthesis controller. However, regarding the RS and RP conditions, it is seen that only the μ -synthesis controller almost satisfies the criteria. Especially for the RP criterion, the \mathcal{H}_∞ controller has a quite large value for $\mu_\Delta(N_{22}(j\omega))$, which means that the controller cannot maintain its high performance in the presence of model uncertainties.

Similar observations are done by looking to Figure 4-13. It is important to mention that the RS and RP conditions for the \mathcal{H}_∞ controller deteriorate in very low frequencies. Hence, in order to compare the controllers more "fairly," we have to look at the frequency range which we want to control. Based on the expected frequency content of the wave disturbances, this range is defined roughly between $1.5 \text{ rad/s} \leq \omega \leq 33 \text{ rad/s}$ (see Table 4-2). For most of this range, it is seen that the μ -synthesis controller has lower values for the conditions of the RS and RP, while the \mathcal{H}_∞ controller has lower values for the NP condition. Overall, based on these results, it is concluded that the μ -synthesis controller achieves better robustness to model uncertainties. In contrast, the \mathcal{H}_∞ controller performs better when considering the nominal system. It is worth noting that these conclusions rely on the accuracy of the approximation of the parametric uncertainties by the complex perturbations (see Section 4-5).

4-7-2 Comparison of designed controllers using different frequency responses

In this section, the performance and the level of satisfaction of the design specifications of the designed controllers are compared in the frequency domain using singular value plots. The closed-loop transfer functions of the sensitivity and the complementary sensitivity (see Eq. (4-6)) are used. They are calculated for each controller using the Matlab function `loopsens`(·) of [33]. Note that in Eq. (4-6), G is replaced by the series connection of the actuators model and the plant model of the system, i.e. GG_{sm} . Despite the expensive computations, most

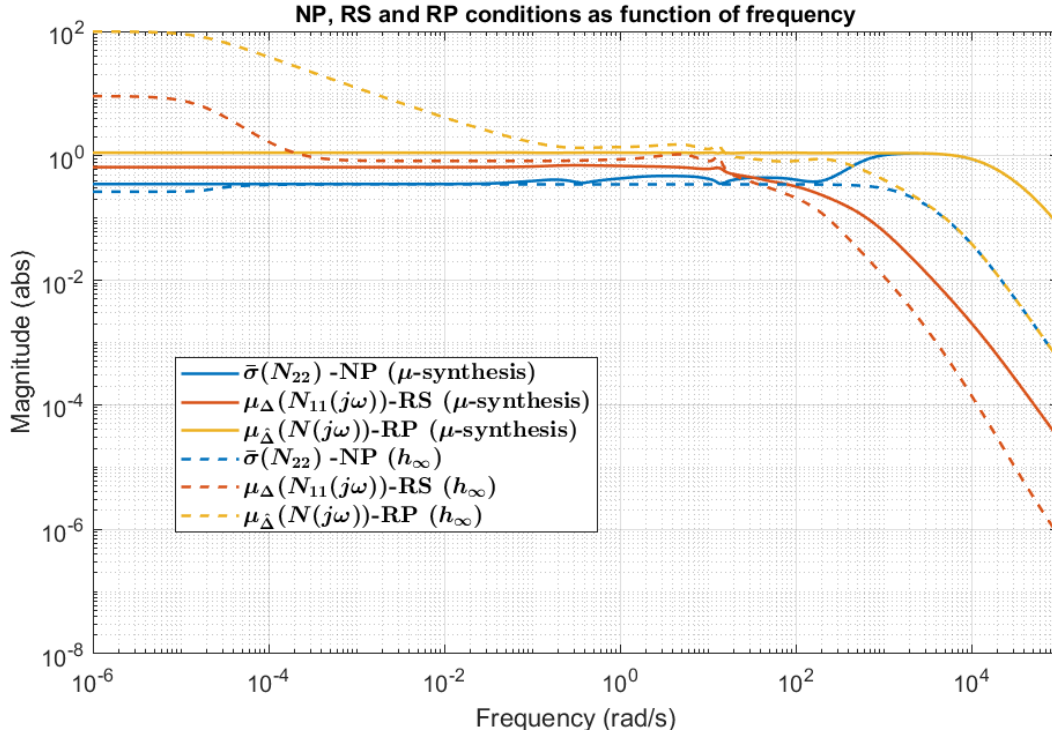


Figure 4-13: NP, RS and RP conditions as a function of frequency for the designed controllers

of the plots presented in this section are obtained using the perturbed systems with the real parametric uncertainty, i.e. the systems G_p , $G_{d,p}$ and $G_{sm,p}$. This choice is made to obtain more accurate frequency responses of the closed-loop systems.

To evaluate the contribution of the reference signal r to the error signal e (see Eq. (4-7), and to show the level of performance specification satisfaction, the frequency responses of the sensitivity function S and the inverse of the performance weight W_P (see Eq. (4-11)) are used. The resulting singular value plots are obtained using the perturbed systems with the real parametric uncertainty, and they are illustrated by Figure 4-14a.

From Figure 4-14a it can be seen that the peak for \mathcal{H}_{∞} controller is $\bar{\sigma}(S) \approx 1.8$, while the corresponding peak of the μ -synthesis controller is $\bar{\sigma}(S) \approx 2.5$. The resulting bandwidth of \mathcal{H}_{∞} controller is $\omega_B \approx 2.1$ rad/s, while the bandwidth of the μ -synthesis controller is $\omega_B \approx 1.8$ rad/s. Considering the observations mentioned above, the level of satisfaction of the design specifications for the peak of S and the bandwidth is satisfactory. It is worth noting that both controllers show relatively small variations of their corresponding $\bar{\sigma}(S)$ in the presence of the perturbations for $\omega > 10^{-2}$ rad/s, which implies that in this frequency range they are quite robust. For low frequencies ($\omega \leq 10^{-2}$ rad/s) it is observed that the $\bar{\sigma}(S)$ for the μ -synthesis controller remains less than 10^{-3} for all possible perturbations, however the corresponding $\bar{\sigma}(S)$ for the \mathcal{H}_{∞} controller has large variations and reaches values more than 10^{-1} . These large variations of the $\bar{\sigma}(S)$ for the \mathcal{H}_{∞} controller implies that the steady-state error is non-zero. Overall, it is deduced that the μ -synthesis controller is more robust, especially in low frequencies, while the \mathcal{H}_{∞} provides slightly better performance.

With the aim to evaluate the accuracy of the approximation of the real parametric uncer-

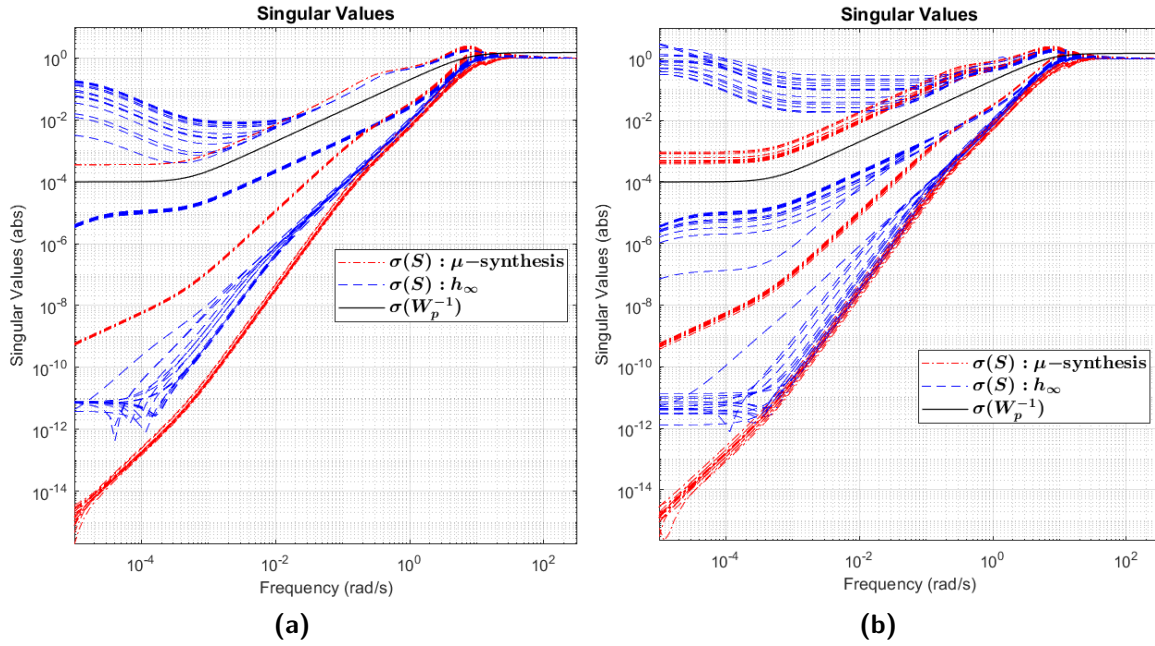


Figure 4-14: Singular values of sensitivity S and the inverse of the performance weight W_P for (a) perturbed systems with real parametric uncertainties and (b) approximated perturbed systems with multiplicative input uncertainties

tainties with the multiplicative input uncertainties, the sensitivities S of both controllers are calculated again using the approximated perturbed systems (G_p^a and $G_{sm,p}^a$). The corresponding frequency responses are illustrated by Figure 4-14b. By comparing the plots of Figure 4-14, it is deduced that for the whole frequency range, the singular values of the sensitivity of μ -synthesis controller for both perturbed systems are pretty similar with minor differences. Nevertheless, for the \mathcal{H}_∞ controller the singular values of the sensitivity for the two perturbed systems show significant variations (especially for $\bar{\sigma}(S)$). Thus, from these results, it is concluded that the approximation of the parametric uncertainties has relatively poor accuracy for low frequencies. Additionally, by considering the singular values of the sensitivity for perturbed systems with multiplicative uncertainties (see Figure 4-14b), it is deduced that the μ -synthesis controller achieves much better robustness compared to the \mathcal{H}_∞ controller.

To quantify the sensitivity of the closed-loop systems to measurement noise n , the complementary sensitivity T is used (see Eq. (4-7)). The frequency responses of T for both controllers are calculated using the perturbed systems with the real parametric uncertainty, and they are shown in Figure 4-15. From Figure 4-15 it is observed that the peak for the \mathcal{H}_∞ controller is $\bar{\sigma}(T) \approx 1.8$, while the corresponding peak for the μ -synthesis controller equals to $\bar{\sigma}(T) \approx 2.5$. Moreover, for $\omega \leq 3$ rad/s the $\bar{\sigma}(T)$ of the μ -synthesis controller is slightly lower than the corresponding one of the \mathcal{H}_∞ controller. For the rest of the frequency range ($\omega > 3$ rad/s) the \mathcal{H}_∞ controller achieves lower $\bar{\sigma}(T)$. Moreover, the variations of the singular values of the T due to the uncertainties are pretty small for both controllers. Considering the results of Figure 4-15, it is deduced that both controllers show satisfactory robustness to the high-frequency measurement noise.

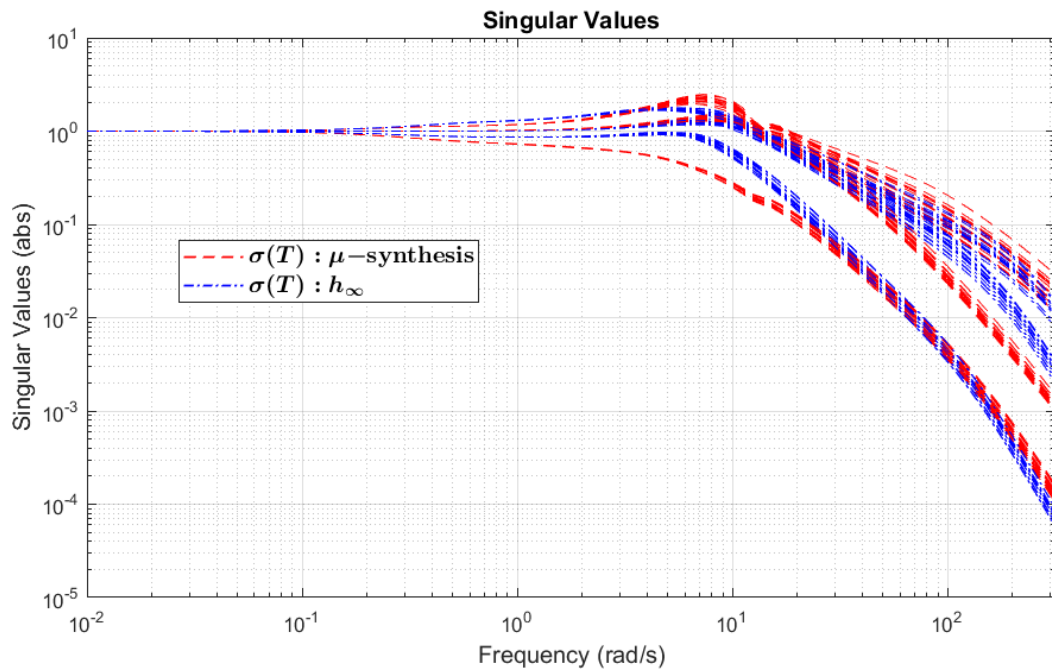


Figure 4-15: Singular values of complementary sensitivity T

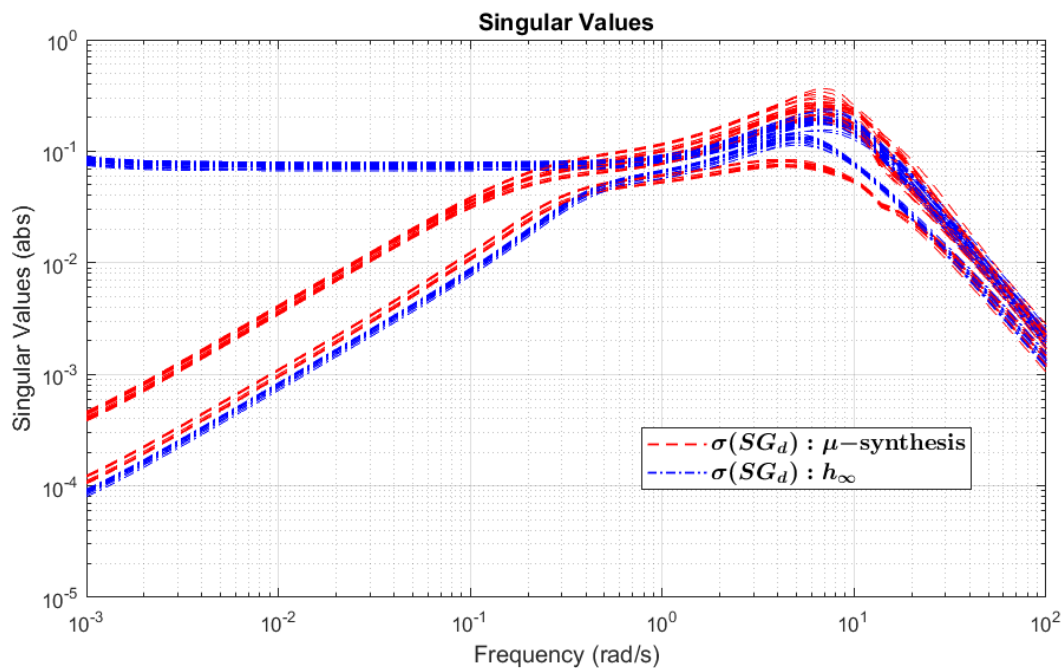


Figure 4-16: Singular values of SG_d (contribution of disturbance to the error signal)

Next, the performance of disturbance rejection for the designed controllers in the frequency domain is evaluated using the singular value plot of SG_d , which expresses the "contribution" of the disturbance d to the error signal e (see Eq. (4-7)). The resulting singular value plots are calculated using the perturbed systems with the real parametric uncertainty, and they

are illustrated by Figure 4-16. By considering the selected frequency range of the wave disturbances (see Table 4-2), it is observed from Figure 4-16 that the $\bar{\sigma}(SG_d)$ for the \mathcal{H}_∞ controller and the μ -synthesis controller are equal to 0.25 and 0.35 respectively (occur at $\omega \approx 7$ rad/s). This implies that the \mathcal{H}_∞ controller achieves slightly better suppression of the wave disturbances compared to the μ -synthesis controller. Comparing the frequency responses within the expected frequency range for both controllers, it is stated that the variations of their singular values due to the uncertainties are relatively small, which means that their performance in disturbance rejection is quite robust.

To analyse the contribution of the reference signal r and disturbance d to the input signal u (see Eq. (4-8)), and to show the level of satisfaction of the control input specification, the frequency responses of KS and KSG_d , and the inverse of the control input weight W_u (see Eq. (4-13)) are used. The resulting singular value plots are obtained using the perturbed systems with the real parametric uncertainty, and they are illustrated by Figure 4-17. From Figure 4-17 it is seen that the control input specification is satisfied only for the case of KSG_d (see Figure 4-17b), while for the case of KS (see Figure 4-17a) is not satisfied at high frequencies ($\omega \geq 10$ rad/s). These results are justified by the selection of the weights for the frequency content of reference signals W_r and the disturbance W_d . More precisely, they were selected to focus on disturbance rejection by setting higher penalties for the disturbance signals. Considering these results, we note that the reference signals must be limited to have low-frequency content to avoid the saturation of the actuators, which may lead to instability or poor performance of the system.

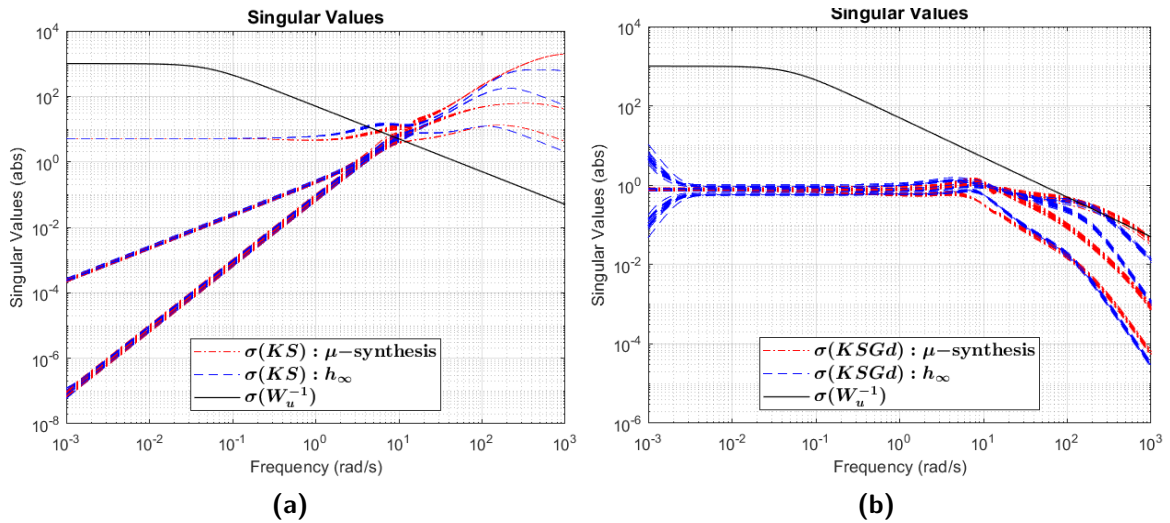


Figure 4-17: Singular values of (a) KS and (b) KSG_d and the inverse of the control input weight W_u

Finally, the frequency responses of the controllers are illustrated by Figure 4-18. From Figure 4-18 it is deduced that both controllers have similar singular values around the selected frequency range of the wave disturbances (see Table 4-2), which gives the reasoning for the similar performance for the disturbance rejection. On the other hand, for low frequencies ($\omega \leq 0.1$ rad/s), the singular values of the μ -synthesis controller are pretty close to each other compared to \mathcal{H}_∞ controller. This result gives reasoning for the better disturbance rejection and the fewer variations of the $\bar{\sigma}(S)$ for the μ -synthesis controller in low frequencies.

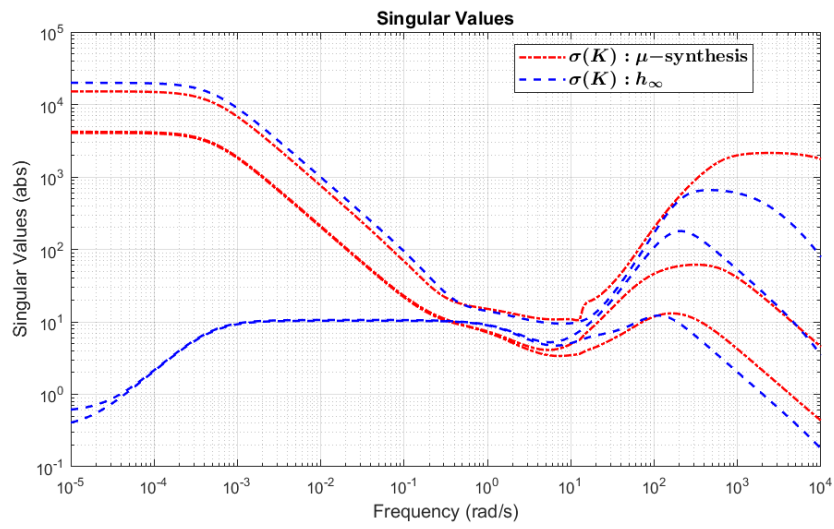


Figure 4-18: Controller Singular Value Plot

Simulation Results

This chapter presents the simulation results in the time domain for the linearized dynamical model of HEARP (see Chapter 3) using the two designed controllers (see Chapter 4). The simulations are focused on the problems of reference tracking and disturbance rejection with the aim of evaluating the performance and robustness of the designed controllers. All the simulation results are obtained by simulating the appropriate systems using the Matlab function `lsim` [33] and the following initial conditions:

$$x_0 = [z_{n0}, \phi_0, \theta_0, \dot{z}_{n0}, \dot{\phi}_0, \dot{\theta}_0]^T = [-0.25, 0, 0, 0, 0, 0]^T$$

Note that these conditions correspond to the equilibrium conditions that were presented previously in Section 3-3-1.

5-1 Reference Tracking

The tracking of reference signals is important mainly for the heave motion when the craft needs to change its altitude. For example, this may be needed when the wave amplitude changes or when the craft has to perform landing or take-off. To evaluate the performance of the designed controllers for the reference tracking problem, it is decided to perform simulations with a nonzero reference signal only for the heave motion and with zero disturbances. In order to achieve a smooth response of the system, the reference signal for heave motion is chosen as a ramping step signal with a magnitude of 0.1 m. This reference acts for 1 s like a ramp signal and settles to its final value after that time. This signal is described by:

$$z_n^{ref}(t) = \begin{cases} 0.1t & \text{for } 0 \text{ s} \leq t \leq 1 \text{ s} \\ 0.1 & \text{for } t > 1 \text{ s} \end{cases} \quad (5-1)$$

The reference signal $r(t)$ that includes all the outputs is defined by:

$$r(t) = [z_n^{ref}(t), \phi^{ref}(t), \theta^{ref}(t)]^T = [z_n^{ref}(t), 0, 0]^T \quad (5-2)$$

where $z_n^{ref}(t)$ is defined in Eq. (5-1).

The responses of the system's outputs y for the reference tracking problem are calculated by simulating the closed-loop system which has as input the reference signal. This closed-loop system correspond to the complementary sensitivity T (see Eq. (4-6)). Additionally, the corresponding actual control input signals u_{in} are calculated by simulating the following system which again has as input the reference signal:

$$\begin{aligned} u_c &= K S r \\ u_{in} &= G_{sm} u_c \\ \implies u_{in} &= G_{sm} K S r \end{aligned}$$

where r is obtained from Eq. (5-2). Note that we derive this equation using Eq. (4-8) and Eq. (4-4).

The system responses and the corresponding control signals of the perturbed systems are calculated using the systems with real parametric uncertainty. The resulting responses and control signals for the nominal and perturbed systems with both controllers are shown in Figure 5-1 and Figure 5-2.

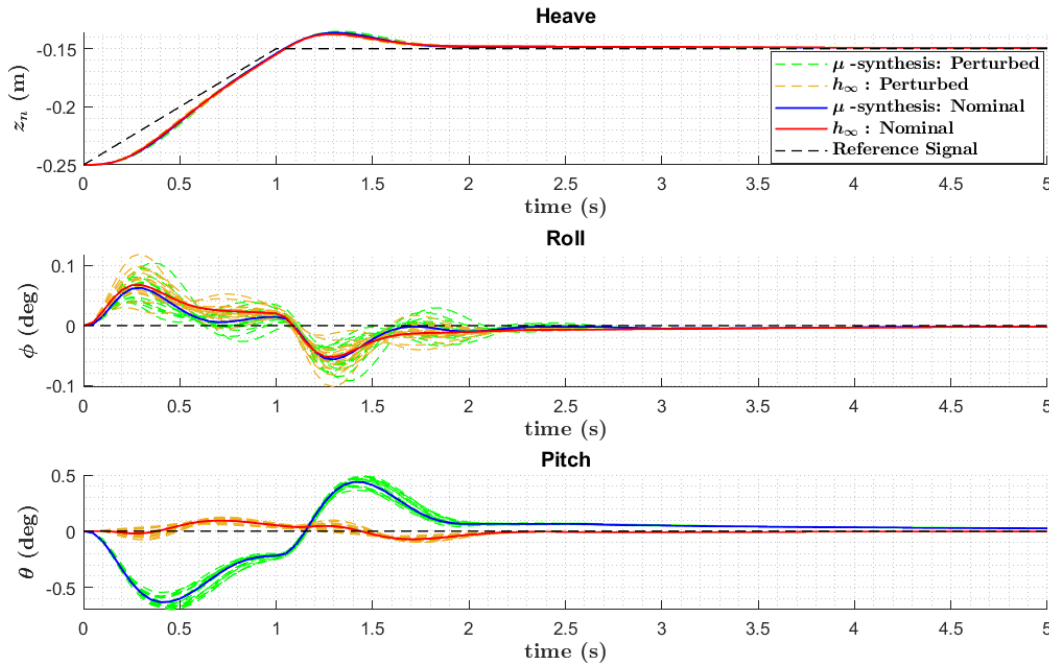


Figure 5-1: System responses for reference tracking

From Figure 5-1, it is seen that the responses for the heave motion are pretty similar with both controllers, while the responses of the roll and pitch motions have some different characteristics. More precisely, the overshoot for the heave motion with both controllers is approximately 12%. Additionally, the responses of heave motion with both controllers have a settling time of less than 2 s. Regarding the roll motion, it is observed that the responses with both controllers have deviations less than 0.1 deg from the equilibrium point (origin) and a settling time of around 2.5 s. From the responses of the pitch motion, it is seen that the \mathcal{H}_∞ controller

has a much lower deviation (around 0.1 deg) from the equilibrium point (origin) compared to the corresponding deviation with the μ -synthesis controller (around 0.6 deg). Moreover, the settling time of the \mathcal{H}_∞ controller is less than 2.5 sec, while for the μ -synthesis controller is around 4 sec.

From these results, it is seen that the \mathcal{H}_∞ controller shows superiority in terms of performance compared to the μ -synthesis controller for the pitch motion. It is a fact that both of the designed controllers show excellent robustness. This is justified by the pretty small deviations from the nominal responses for all output channels and especially for the heave and pitch motions of both controllers. Considering all the above, it is concluded that the performance and the robustness of both controllers for the reference tracking are quite satisfactory.

By looking at the results of Figure 5-2 it is observed that the control signals for both controllers remain relatively far away from the saturation limits of the servo motors even in the presence of the uncertainties ($-69.72^\circ \leq \delta_s^i \leq 29.67^\circ$, see Section 2-8-2). Furthermore, it is deduced that the control signals for the \mathcal{H}_∞ controller are slightly larger than the corresponding signals of the μ -synthesis controller. So this observation can justify the superior performance of the \mathcal{H}_∞ controller regarding the pitch motion. This result originates from the resulting synthesis of the μ -synthesis controller, which "sacrifices" some performance of the system aiming to achieve robustness with respect to the model uncertainties.

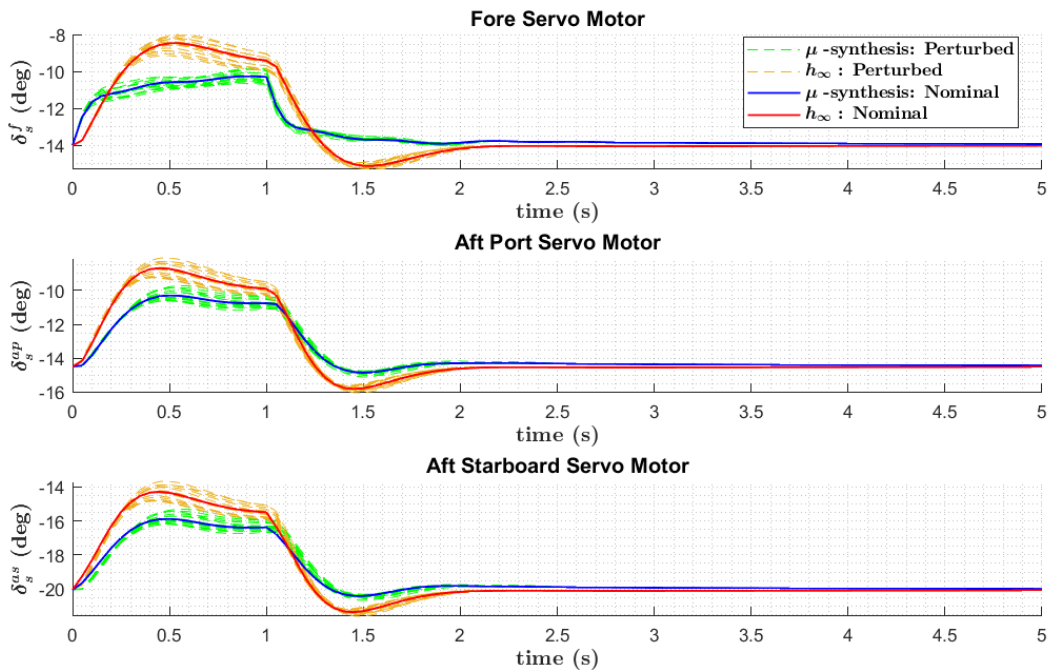


Figure 5-2: Control signals for reference tracking

The system responses are also calculated using the approximated perturbed systems to evaluate the accuracy of the approximation of the real parametric uncertainties with the multiplicative input uncertainties in the time domain. The corresponding system responses are illustrated by Figure 5-3. It is seen from Figure 5-3 that the responses of the heave motion for both controllers are approximated relatively well using the multiplicative input uncertainties. Conversely, by comparing the responses of the roll and pitch motions for the perturbed

systems with the multiplicative and the parametric uncertainty, it is deduced that the approximation of the uncertainties has low accuracy as the responses have large deviations (especially for \mathcal{H}_∞ controller). Considering the perturbed systems with the multiplicative uncertainty, it is observed that the μ -synthesis controller shows superior robustness in its performance compared to the \mathcal{H}_∞ controller as the deviations from the nominal responses are lower for all output channels.

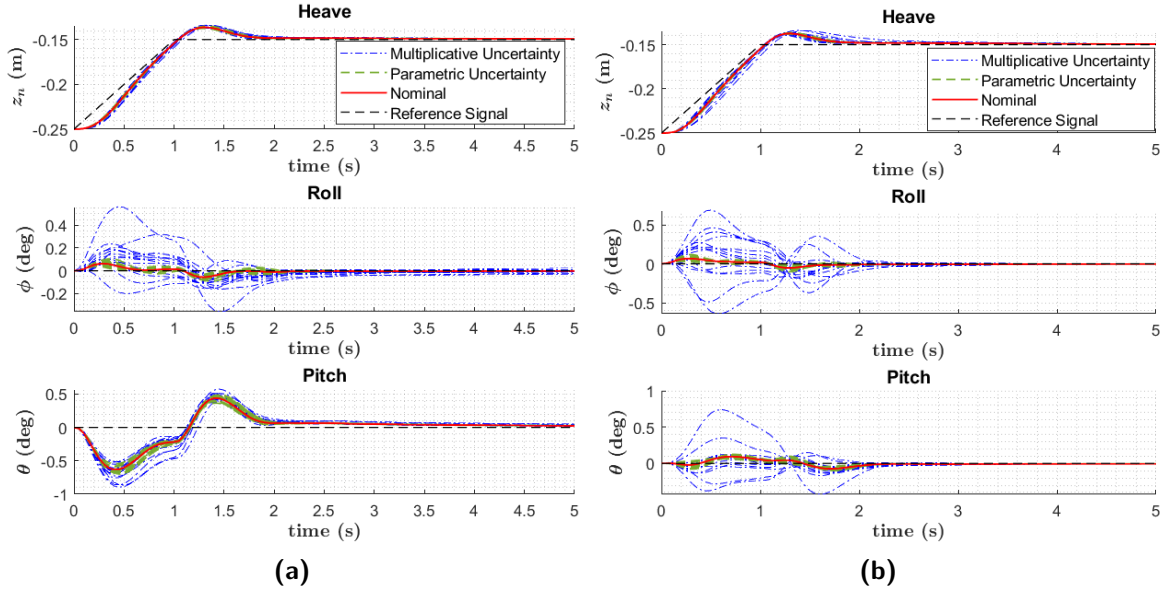


Figure 5-3: Comparison of system responses for reference tracking with the parametric and multiplicative uncertainties for (a) μ -synthesis controller and (b) \mathcal{H}_∞ controller

5-2 Disturbance Rejection

The general goal of the control system is to perform a stable level steady flight (see Section 3-3-1) and decouple the motions of the craft from the incident waves. Recall that the influence of the incident waves on the dynamics of the HEARP is modelled by considering a linear model with regular waves (see Section 2-7). To evaluate the performance of the designed controllers for the disturbance rejection problem, it is decided to perform simulations for various wave frequencies ω , wave amplitudes ζ_0 and encounter angles β . Note that all the simulations are performed using zero reference signals. Based on the selected conditions of the regular waves (see Section 2-7-2), ω , ζ_0 and β in are selected as:

- $\omega = [3.51, 3.92, 4.83, 5.55, 7.85]$ rad/s
- $\zeta_0 = [0.02, 0.04, 0.06, 0.08, 0.1]$ m
- $\beta = [0, 180]$ degrees (0 for heading waves and 180 for following waves)

Note that the values of wave frequencies ω are related to the wave length λ by Eq. (2-10), so they are calculated by using the selected values of $\lambda = [1, 2, 3, 4, 5]$ m (see Section 2-7-2). Considering the selected frequency range, the simulation time for each case is set to 20 sec with a time step of 0.05 sec.

The responses of the system's outputs y for the disturbance rejection problem are calculated by simulating the system SG_d which has as input the disturbance signal (see Eq. (4-6)). Moreover, the corresponding actual control input signals u_{in} are calculated by simulating the following system which again has as input the reference signal (see Eq. (4-8) and Figure 4-3):

$$\begin{aligned} u_c &= -KSG_d d_w \\ u_{in} &= G_{sm} u_c \\ \implies u_{in} &= -G_{sm} KSG_d d_w \end{aligned}$$

where d_w is obtained from Eq. (3-9). Note that we derive this equation using Eq. (4-8) and Eq. (4-4).

To show the performance and the robustness of the designed controllers for specific wave conditions, the system responses and the corresponding control signals are calculated as a function of time using the following conditions:

- $\omega = 4.83$ rad/s (Wave frequency)
- $\lambda = 3$ m (Wave length)
- $\zeta = 0.06$ m (Wave amplitude)
- $\beta = 0^\circ$ (Wave encounter angle - Following waves)

The system responses and the corresponding control signals of the perturbed systems are again calculated using the systems with real parametric uncertainty. The results are shown in Figure 5-4 and Figure 5-5. From Figure 5-4 it is observed that the responses of all outputs have a sinusoidal shape with a frequency equal to the absolute value of corresponding encounter frequency $|\omega_e| = 3.84$ rad/s (calculated by using $\omega = 4.83$ rad/s and Eq. (2-13)). The amplitudes of the sinusoidal responses (deviations from equilibrium) of heave motion are approximately 0.04 m and 0.03 m for the μ -synthesis controller and the \mathcal{H}_∞ controller respectively. In addition, the amplitudes of the sinusoidal responses of roll and pitch motions for both controllers are less than approximately 0.3 deg and 2.5 deg respectively. It is worth noting that the amplitudes for the roll motion are around 10 times less than the corresponding amplitudes of the pitch motion. This result is due to the fact that the wave direction is perpendicular to the axis of rotation of the pitch motion, while the axis of rotation of roll motion is parallel to the wave direction.

Additionally, it is deduced that the responses of the two controllers have different phases, even though they start from the same initial conditions. This result arises from differences in the phase of the frequency responses of the designed controllers. The robustness of both controllers is quite satisfactory as the deviations of the perturbed responses from the nominal responses for all outputs are very small.

It is seen from Figure 5-5 that the deviations of the control signals from their equilibrium for all input channels are limited to less than 10 deg, so they are kept far away from the saturation limits (see Section 2-8-2). By comparing the resulting control signals of the two controllers, it is seen that they have minor differences. The resulting robustness of both controllers is excellent as the variations of the control signals for the perturbed systems from their nominal values are negligible.

With the aim to evaluate the performance and the robustness of the designed controllers for the different conditions of the regular waves, we use the root mean square (RMS) values of

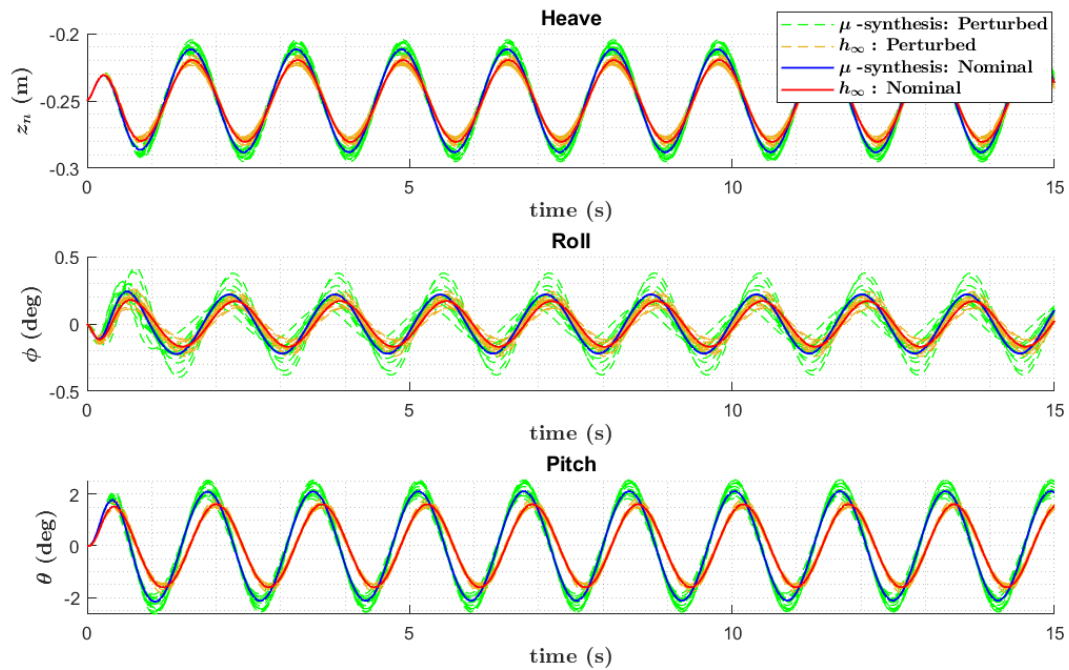


Figure 5-4: System responses for disturbance rejection.

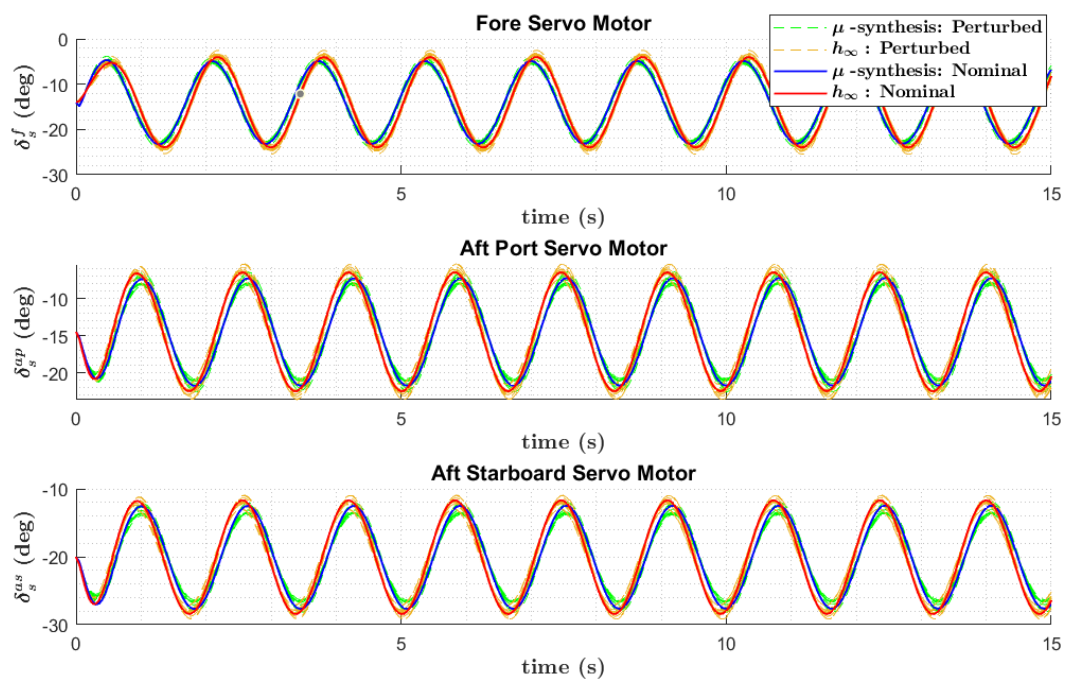


Figure 5-5: Control signals for reference tracking

the error signals. The use of the RMS values for the performance evaluation of controllers is

also found in [4] and [20]. The RMS of each error signal is defined by:

$$RMS = \sqrt{\frac{\sum_{i=1}^N e^2(t)}{N}}$$

where the error signal e is calculated by Eq. (4-7) and N denotes the number of time steps that are included in the time window of the simulation.

The simulations are performed by keeping one of the three parameters constant (ω , ζ_0 and β) and by changing the remaining one. The constant parameters for ω and ζ_0 are selected to lie around the middle of their range. Therefore, two plots of the RMS values are obtained using varying values of ω , ζ_0 and β . Note that each of the aforementioned plots illustrates the RMS values for both wave encounter angles. The resulting plots of RMS for the error signals with different wave conditions are shown in Figure 5-6 and Figure 5-7.

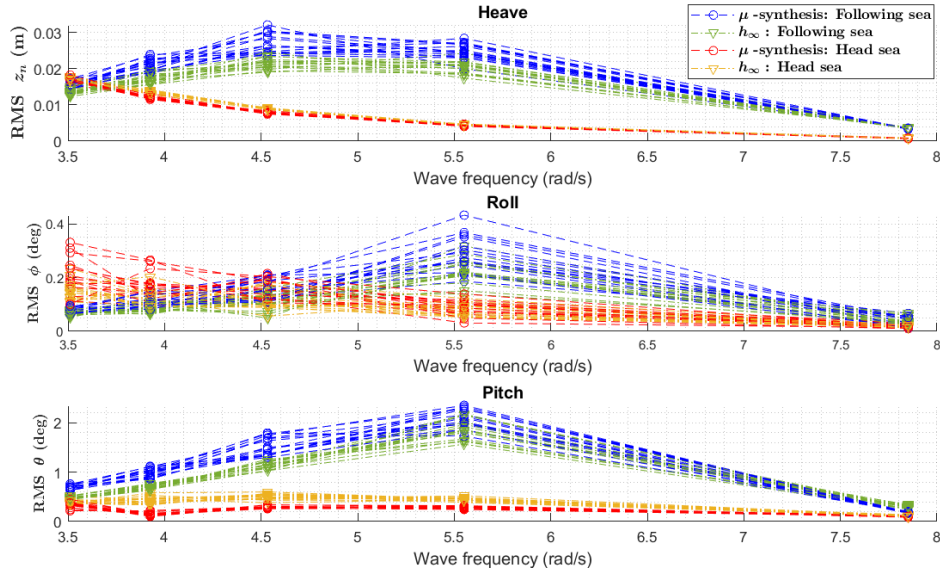


Figure 5-6: RMS of the error signals for varying wave frequency and with $\zeta_0 = 0.06$ m.

By looking to Figure 5-6 and Figure 5-7, the following observations are made:

- The following waves lead to larger RMS values than the head waves for most cases. These results confirm that the performance of a hydrofoil craft in the presence of following waves is worse than under head waves [26], [4].
- The RMS values with the following waves for all outputs of the \mathcal{H}_∞ controller are slightly lower than the corresponding ones of the μ -synthesis controller. Conversely, the RMS values with head waves for heave and pitch motions of the μ -synthesis controller are slightly lower than the corresponding ones of the \mathcal{H}_∞ controller.
- In general, both controllers achieve satisfactory robustness as the variations of their RMS values are pretty small.
- For increasing ζ_0 , the RMS values for all cases also increase monotonically, which is expected as the resulting wave velocity components are proportional to the ζ_0 values (see Eq. (3-9)).
- The peak of the RMS values for following waves and head waves occurs at the wave frequencies that correspond to encounter frequencies close to $\omega_e \approx 7$ rad/s. More

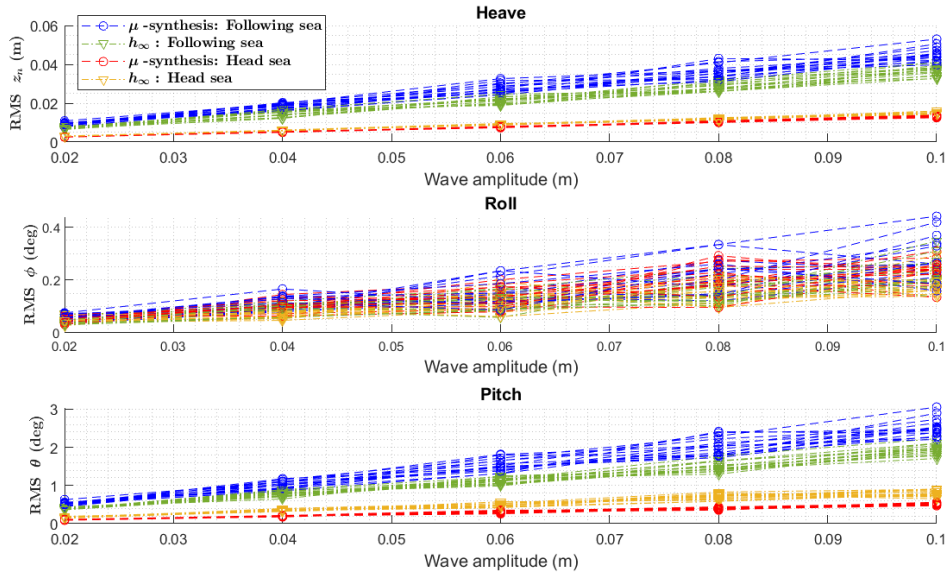


Figure 5-7: RMS of the error signals for varying wave amplitude and with $\omega = 4.53$ rad/s

precisely, for following waves occurs at $\omega = 4.5$ rad/s ($|\omega_e| = 4.68$ rad/s) and for head waves occurs at $\omega = 4.5$ rad/s ($|\omega_e| = 8.53$ rad/s). This observation is connected to the results of Figure 4-16, where the peak of the σSG_d occurs around $\omega \approx 7$ rad/s.

- It is observed that the RMS values for heave and pitch motions are relatively large, especially for following waves. For example, the RMS values for the heave motion are around half of the corresponding wave amplitude, which indicates that the capability to decouple the craft from the wave disturbances is relatively limited. This result may be reasoned by the fact that for the selected wave frequencies, the resulting encounter frequencies (1.52 rad/s $\leq |\omega_e| \leq 32.98$ rad/s) lie outside the bandwidth of both controllers ($\omega_B \approx 2$ rad/s).

Conclusions and Recommendations

This chapter makes some conclusions about the findings and the results of this thesis project. Next, some recommendations are given for future research to further develop the HEARP project.

6-1 Conclusions

This thesis project presents the development a dynamical model for an experimental hydrofoil craft (HEARP) and the design of motion control systems using multivariable feedback control theory. Considering the content and results of all chapters of this thesis project, various conclusions are made, which are summarized in this section.

A linearized state-space model with three DOF has been developed using the theory of the hydrodynamics of marine crafts and aircraft dynamics. Because of the neglected dynamics, the linearization, and the parametric uncertainties, the accuracy of the developed model is unknown as it is not validated with any experiments. Nevertheless, the results obtained in this study are reasonable by considering the results of other similar studies, which implies that the proposed model is a good start for future development.

The different parameters of the dynamical model are estimated using the available information. However, any mismatch of these estimations from the actual values may deteriorate the accuracy of the proposed dynamical model. This is why different parametric uncertainties have been assigned based on the available information, aiming to design a robust control system for HEARP. It has to be emphasized that these uncertainties have to be defined more accurately, to design a less conservative robust controller.

It is deduced that the problem of controller synthesis using the defined parametric uncertainties is not solvable with an ordinary computer because of the enormous size of the required computations. Therefore, the real parametric uncertainties were approximated by multiplicative input uncertainties (dynamic uncertainties), leading to a much simpler representation of uncertainty in the frequency domain. After different analyses and simulations in the frequency

and time domains using the proposed control systems, it is shown that this approach gives a relatively accurate representation of the parametric uncertainties. Nevertheless, some noticeable differences between some responses in the frequency and time domains were observed. These results indicate that the method followed to represent the parametric uncertainties by complex perturbations should be modified appropriately, aiming to improve the accuracy of the approximation.

Using the derived linear dynamical model of HEARP, two different control approaches were implemented based on multivariable feedback control theory, namely the \mathcal{H}_∞ synthesis and the μ -synthesis. From different analyses in the frequency and time domains, it is concluded that for the modelled uncertainty (dynamic uncertainty), the μ -synthesis controller shows superiority in terms of performance and robustness compared to the \mathcal{H}_∞ synthesis controller. This result is expected as the design of this controller incorporates the uncertainties of the dynamical model. Conversely, from results obtained from the perturbed systems with the real parametric uncertainty, it is observed that the \mathcal{H}_∞ synthesis controller has slightly better performance and similar robustness with respect to the μ -synthesis controller. These results are justified by the fact that the resulting inaccuracies of the approximation of the parametric uncertainties by the complex perturbations perhaps have led to a relatively conservative design of the μ -synthesis controller.

Considering the simulation results presented in this thesis, it is concluded that the designed controllers can offer the HEARP system a high performance and robust operation for the objectives of reference tracking and disturbance rejection. However, because the developed dynamical model and the proposed controllers are not validated experimentally, it is not possible to compare the results with the current control system that is delivered by Flying Fish. Thus, the results can be compared only with those found in different studies. Nevertheless, most studies found in the literature regarding hydrofoil crafts have different dynamical models, which usually do not include actuator dynamics, and perform simulations with different wave conditions. So a comparison with these studies is avoided. Hence, researchers that will be involved with the HEARP system are prompted to evaluate the performance of the proposed control systems experimentally and compare them with the performance of controllers that are designed using different methods.

6-2 Recommendations

Future researchers are encouraged to consider the following suggestions in their research for the development of a high-performance and robust control system for HEARP:

1. Validate the accuracy of the proposed dynamical model via experiments, using the closed-loop system with one of the proposed controllers, as the system is marginally stable. This can be performed using the same input signals for both simulations and the experimental setup and comparing the resulting outputs of the proposed dynamical model and the measured outputs from the sensors of HEARP. To quantify the accuracy of the model, the metric of variance accounted for (VAF) can be used [46]. The VAF has a value between 0% and 100%, i.e. for high values of the VAF, the prediction error is low, so the proposed model is accurate.
2. Use the Linear Grey-Box system identification method aiming to improve the validation rate of the proposed dynamical model [33]. It is suggested to implement this

method using the closed-loop system and a simple state-space controller such as a Linear Quadratic Regulator (LQR). In addition, persistently exciting input signals have to be chosen, such as pseudo-random binary sequence [46].

3. Consider the development of a more complete dynamical model that may include, among others: the 6 DOF of the craft, the effect of surface proximity, the influence of irregular waves on the hydrofoils and the hydrodynamic forces acting on the struts of the hydrofoils, the rudder and the propeller.
4. Perform experiments to estimate more accurately the mass properties of HEARP (CG and moments of inertia).
5. Implement the designed controllers on the experimental setup of HEARP by developing the necessary software in PX4 codes. The transfer function matrices of each controller have to be transformed to the corresponding continuous-time state-space model. Then these should be discretized using the appropriate sampling time [2]. Note that the resulting discrete-time state-space model of the controller will have as input the error signals and as output the commanded control inputs (see Eq. (4-5))
6. Validate the performance of the proposed control designs for reference tracking and disturbance rejection via experiments in the towing tank and in outside water (lake, canal). If needed, re-tune the designed controllers iteratively by using the experimental results as a reference instead of the simulation results.
7. By performing various experiments, try to characterize the dynamic uncertainty included in the proposed linear dynamical model. In that way, any missing or neglected dynamics, mostly at high frequencies, can be quantified by complex perturbations. This idea can lead to a more accurate and straightforward description of the model uncertainty using dynamic perturbations. Therefore using these uncertainties, the robust control design can provide a controller with higher performance and robustness.
8. Design automatic control algorithms for the propulsion system (propeller) and the system's steering (rudder), aiming to provide a repetitive response during tests of various control algorithms of HEARP. In that way, the system's performance will be independent of the control skills of the operator.

Appendix A

Equations of the Linear State-Space Model

This Appendix presents all the equations of the linearized state-space model and its corresponding numerical values, based on the theory and the results of Chapter 3.

First, the inverse of the rigid-body inertia matrix is independent of states and control inputs, thus it is already linear. It can be defined as:

$$M_{RB_3}^{-1} = \begin{bmatrix} \frac{1}{m} & 0 & 0 \\ 0 & -\frac{I_y}{I_{xy}^2 - I_x I_y} & -\frac{I_{xy}}{I_{xy}^2 - I_x I_y} \\ 0 & -\frac{I_{xy}}{I_{xy}^2 - I_x I_y} & -\frac{I_x}{I_{xy}^2 - I_x I_y} \end{bmatrix} \quad (\text{A-1})$$

The Jacobians matrices of the vectors $-C_{RB_3}(x)x$ and $-g_3(x)$ with respect to the states x evaluated at equilibrium states $x = x^*$ are defined as:

$$\left. \frac{\partial (-C_{RB_3}(x)x)}{\partial x} \right|_{x=x^*} = C_{RB_3}^x = \begin{bmatrix} 0 & 0 & 0 & 0 & 0 & U_0 m \\ 0 & 0 & 0 & 0 & 0 & 0 \\ 0 & 0 & 0 & 0 & 0 & 0 \end{bmatrix} \quad (\text{A-2})$$

$$\left. \frac{\partial (-g_3(x))}{\partial x} \right|_{x=x^*} = g_3^x = \begin{bmatrix} 0 & 0 & 0 & 0 & 0 & 0 \\ 0 & 0 & 0 & 0 & 0 & 0 \\ 0 & 0 & 0 & 0 & 0 & 0 \end{bmatrix} \quad (\text{A-3})$$

Note that these vectors are independent from the control inputs u_{in} and the disturbances d_w , thus the Jacobian matrices with respect to u_{in} and d_w are equal to zero.

The Jacobian matrix of the vector $\tau_{i_3}(x, u_{in}, d_w)$ with respect to the states x evaluated at equilibrium conditions is defined as:

$$\left. \frac{\partial (\tau_{i_3}(x, u_{in}, d_w))}{\partial x} \right|_{\substack{x=x^* \\ u_{in}=u_{in}^* \\ d_w=d_w^*}} = \tau_i^x = \begin{bmatrix} 0 & 0 & \tau_{i,13}^x & \tau_{i,14}^x & \tau_{i,15}^x & \tau_{i,16}^x \\ 0 & 0 & \tau_{i,23}^x & \tau_{i,24}^x & \tau_{i,25}^x & \tau_{i,26}^x \\ 0 & 0 & \tau_{i,33}^x & \tau_{i,34}^x & \tau_{i,35}^x & \tau_{i,36}^x \end{bmatrix} \quad (\text{A-4})$$

Each element of matrix in Eq. (A-4) is defined by:

$$\tau_{i,13}^x = -\frac{1}{2}\rho U_0^2 A_h (C_{L_\alpha} + Q_1) \quad (\text{A-5a})$$

$$\tau_{i,14}^x = -\frac{1}{2}\rho U_0 A_h (C_{L_\alpha} + Q_1) \quad (\text{A-5b})$$

$$\tau_{i,15}^x = -\frac{1}{2}\rho U_0 A_h (C_{L_\alpha} + Q_1) l_y^i \quad (\text{A-5c})$$

$$\tau_{i,16}^x = \frac{1}{2}\rho U_0 A_h \left((C_{L_\alpha} + Q_1) l_x^{i*} - Q_2 l_z^{i*} \right) \quad (\text{A-5d})$$

$$\tau_{i,23}^x = -\frac{1}{2}\rho U_0^2 A_h (C_{L_\alpha} + Q_1) l_y^i \quad (\text{A-5e})$$

$$\tau_{i,24}^x = -\frac{1}{2}\rho U_0 A_h (C_{L_\alpha} + Q_1) l_y^i \quad (\text{A-5f})$$

$$\tau_{i,25}^x = -\frac{1}{2}\rho U_0 A_h (C_{L_\alpha} + Q_1) l_y^{i2} \quad (\text{A-5g})$$

$$\tau_{i,26}^x = \frac{1}{2}\rho U_0 A_h \left((C_{L_\alpha} + Q_1) l_x^{i*} - Q_2 l_z^{i*} \right) l_y^i \quad (\text{A-5h})$$

$$\tau_{i,33}^x = \frac{1}{2}\rho U_0^2 A_h \left((C_{L_\alpha} + Q_1) l_x^{i*} + (C_{D_\alpha} - Q_2) l_z^{i*} \right) \quad (\text{A-5i})$$

$$\tau_{i,34}^x = \frac{1}{2}\rho U_0 A_h \left((C_{L_\alpha} + Q_1) l_x^{i*} + (C_{D_\alpha} - Q_2) l_z^{i*} \right) \quad (\text{A-5j})$$

$$\tau_{i,35}^x = \frac{1}{2}\rho U_0 A_h \left((C_{L_\alpha} + Q_1) l_x^{i*} + (C_{D_\alpha} - Q_2) l_z^{i*} \right) l_y^i \quad (\text{A-5k})$$

$$\tau_{i,36}^x = -\frac{1}{2}\rho U_0 A_h \left(\left((C_{L_\alpha} + Q_1) l_x^{i*} - Q_2 l_z^{i*} \right) l_x^{i*} + \left((C_{D_\alpha} + Q_2) l_x^{i*} + Q_1 l_z^{i*} \right) l_z^{i*} \right) \quad (\text{A-5l})$$

where,

$$l_x^{i*} = l_{x_j}^i + l_c \sin \left(\gamma_0 - \frac{l_s}{h_h} \delta_s^{i*} \right) \quad l_z^{i*} = l_{z_j}^i + l_c \cos \left(\gamma_0 - \frac{l_s}{h_h} \delta_s^{i*} \right) \quad (\text{A-6a})$$

$$Q_1 = C_{D_0} - \frac{l_s}{h_h} \delta_s^{i*} C_{D_\alpha} \quad Q_2 = C_{L_0} - \frac{l_s}{h_h} \delta_s^{i*} C_{L_\alpha} \quad (\text{A-6b})$$

The Jacobian matrix of the vector $\tau_{i_3}(x, u_{in}, d_w)$ with respect to the control inputs u_{in} evaluated at equilibrium conditions is defined as:

$$\frac{\partial (\tau_{i_3}(x, u_{in}, d_w))}{\partial u_{in}} \bigg|_{\substack{x=x^* \\ u_{in}=u_{in}^* \\ d_w=d_w^*}} = \tau_i^{u_{in}} = \begin{bmatrix} \tau_{i,11}^{u_{in}} \\ \tau_{i,21}^{u_{in}} \\ \tau_{i,31}^{u_{in}} \end{bmatrix} \quad (\text{A-7})$$

Each element of vector in Eq. (A-7) is defined by:

$$\tau_{i,11}^{u_{in}} = \frac{1}{2} \frac{l_s}{h_h} \rho A_h U_0^2 C_{L_\alpha} \quad (\text{A-8a})$$

$$\tau_{i,21}^{u_{in}} = \frac{1}{2} \frac{l_s}{h_h} \rho A_h U_0^2 C_{L_\alpha} l_y^i \quad (\text{A-8b})$$

$$\tau_{i,31}^{u_{in}} = \frac{1}{2} \frac{l_s}{h_h} \rho A_h U_0^2 \left(C_{D_\alpha} l_z^{i*} - C_{L_\alpha} l_x^{i*} - Q_2 l_c \cos \left(\gamma_0 - \frac{l_s}{h_h} \delta_s^{i*} \right) - Q_1 l_c \sin \left(\gamma_0 - \frac{l_s}{h_h} \delta_s^{i*} \right) \right) \quad (\text{A-8c})$$

The Jacobian matrix of the vector $\tau_{i_3}(x, u_{in}, d_w)$ with respect to the wave disturbances d_w evaluated at equilibrium conditions is defined as:

$$\left. \frac{\partial (\tau_{i_3}(x, u_{in}, d_w))}{\partial d_w} \right|_{\substack{x=x^* \\ u_{in}=u_{in}^* \\ d_w=d_w^*}} = \tau^{d_w} = \begin{bmatrix} \tau_f^{d_w} & \tau_{ap}^{d_w} & \tau_{as}^{d_w} \end{bmatrix} \quad (\text{A-9})$$

where each vector $\tau_i^{d_w}$ is described as:

$$\tau_i^{d_w} = \begin{bmatrix} -\rho A_h U_0 \left(C_{L_0} - \frac{l_s}{h_h} \delta_s^{i*} C_{L_\alpha} \right) & -\frac{1}{2} \rho A_h U_0 \left(C_{D_0} - \frac{l_s}{h_h} \delta_s^{i*} C_{D_\alpha} + C_{L_\alpha} \right) \\ -\rho A_h U_0 \left(C_{L_0} - \frac{l_s}{h_h} \delta_s^{i*} C_{L_\alpha} \right) l_y^i & -\frac{1}{2} \rho A_h U_0 \left(C_{D_0} - \frac{l_s}{h_h} \delta_s^{i*} C_{D_\alpha} + C_{L_\alpha} \right) l_y^i \\ \rho A_h U_0 \left(Q_2 l_x^{i*} - Q_1 l_z^{i*} \right) & \frac{1}{2} \rho A_h U_0 \left((Q_2 - C_{D_\alpha}) l_x^{i*} + (Q_1 + C_{D_\alpha}) l_z^{i*} \right) \end{bmatrix} \quad (\text{A-10})$$

Using all the results of this Appendix and Eq. (3-4), the linear state-space model of HEARP is defined as follows:

$$\begin{aligned} \delta \dot{x}(t) &= A \delta x(t) + B \delta u_{in}(t) + B_d \delta d_w(t) \\ \delta y(t) &= C \delta x(t) \end{aligned}$$

where

$$A = \begin{bmatrix} I_3 & O_{3 \times 3} \\ M_{RB_3}^{-1} \left(C_{RB_3}^x + \tau_f^x + \tau_{ap}^x + \tau_{as}^x \right) & \end{bmatrix} \quad (\text{A-12a})$$

$$B = \begin{bmatrix} O_{3 \times 1} & O_{3 \times 1} & O_{3 \times 1} \\ M_{RB_3}^{-1} \tau_f^u & M_{RB_3}^{-1} \tau_{ap}^u & M_{RB_3}^{-1} \tau_{as}^u \end{bmatrix} \quad (\text{A-12b})$$

$$B_d = \begin{bmatrix} O_{3 \times 2} & O_{3 \times 2} & O_{3 \times 2} \\ M_{RB_3}^{-1} \tau_f^{d_w} & M_{RB_3}^{-1} \tau_{ap}^{d_w} & M_{RB_3}^{-1} \tau_{as}^{d_w} \end{bmatrix} \quad (\text{A-12c})$$

$$C = I_3 \quad (\text{A-12d})$$

Note that I_3 denotes an identity matrix of dimension 3 and $O_{i \times j}$ denotes a matrix of zeros with appropriate dimensions.

The numerical values for the matrices A , B , B_d and C are calculated using the nominal values

of all the parameters that are introduced in Section 3-5, and they are given as follows:

$$\mathbf{A} = \begin{bmatrix} 0 & 0 & 0 & 1 & 0 & 0 \\ 0 & 0 & 0 & 0 & 1 & 0 \\ 0 & 0 & 0 & 0 & 0 & 1 \\ 0 & 0 & -104.25 & -26.06 & 0.64 & 3.86 \\ 0 & 0 & 16.33 & 4.08 & -6.40 & 0.83 \\ 0 & 0 & 42.82 & 10.71 & 0.23 & -11.49 \end{bmatrix} \quad (\text{A-13})$$

$$\mathbf{B} = \begin{bmatrix} 0 & 0 & 0 \\ 0 & 0 & 0 \\ 0 & 0 & 0 \\ 11.59 & 11.59 & 11.59 \\ -0.02 & -22.26 & 16.83 \\ -25.28 & 6.90 & 3.90 \end{bmatrix} \quad (\text{A-14})$$

$$\mathbf{B}_d = \begin{bmatrix} 0 & 0 & 0 & 0 & 0 & 0 \\ 0 & 0 & 0 & 0 & 0 & 0 \\ 0 & 0 & 0 & 0 & 0 & 0 \\ -1.41 & -8.68 & -1.46 & -8.68 & -2.03 & -8.69 \\ 0.04 & 0.02 & 2.85 & 16.68 & -2.89 & -12.62 \\ 2.65 & 18.90 & -1.32 & -5.22 & -1.33 & -2.98 \end{bmatrix} \quad (\text{A-15})$$

$$\mathbf{C} = \begin{bmatrix} 1 & 0 & 0 & 0 & 0 & 0 \\ 0 & 1 & 0 & 0 & 0 & 0 \\ 0 & 0 & 1 & 0 & 0 & 0 \end{bmatrix} \quad (\text{A-16})$$

Appendix B

Transfer Function Matrices of the Control Design

The transfer function matrix of the plant model \mathbf{G} in Eq. (4-1) is given by:

$$\mathbf{G}(s) = \begin{bmatrix} \frac{11.59(s+6.32)(s^2+3.16s+182.9)}{s^2(s+30.55)(s+7.85)(s+5.54)} & \frac{11.59(s+19.09)(s+5.40)(s-5.53)}{s^2(s+30.55)(s+7.85)(s+5.54)} & \frac{11.59(s-4.52)(s+7.36)(s+17.27)}{s^2(s+30.55)(s+7.85)(s+5.54)} \\ \frac{-0.02(s-28.56)(s-1125)}{s(s+30.55)(s+7.85)(s+5.54)} & \frac{-22.26(s+29.4)(s+5.77)}{s(s+30.55)(s+7.85)(s+5.54)} & \frac{16.83(s+32.32)(s+8.23)}{s(s+30.55)(s+7.85)(s+5.54)} \\ \frac{-25.28(s+6.2)(s+21.36)}{s(s+30.55)(s+7.85)(s+5.54)} & \frac{6.90(s+44.28)(s+5.41)}{s(s+30.55)(s+7.85)(s+5.54)} & \frac{3.90(s+57.88)(s+7.36)}{s(s+30.55)(s+7.85)(s+5.54)} \end{bmatrix} \quad (\text{B-1})$$

The transfer function matrix of the disturbance model \mathbf{G}_d in Eq. (4-1) is given by:

$$\mathbf{G}_d(s) = \begin{bmatrix} \frac{-1.42(s+6.32)(s^2+4.32s+151.2)}{s^2(s+30.55)(s+7.85)(s+5.54)} & \frac{-8.69(s+6.32)(s^2+3.18s+182.4)}{s^2(s+30.55)(s+7.85)(s+5.54)} & \frac{-1.46(s+21.08)(s+5.58)(s-6.54)}{s^2(s+30.55)(s+7.85)(s+5.54)} \\ \frac{0.04(s^2-53.44s+1823)}{s(s+30.55)(s+7.85)(s+5.54)} & \frac{0.02(s-28.78)(s-931.2)}{s(s+30.55)(s+7.85)(s+5.54)} & \frac{2.85(s+29.6)(s+5.47)}{s(s+30.55)(s+7.85)(s+5.54)} \\ \frac{2.65(s+6.20)(s+20.57)}{s(s+30.55)(s+7.85)(s+5.54)} & \frac{18.90(s+6.2)(s+21.35)}{s(s+30.55)(s+7.85)(s+5.54)} & \frac{-1.32(s+38.26)(s+5.58)}{s(s+30.55)(s+7.85)(s+5.54)} \\ \frac{-8.68(s+19.12)(s+5.40)(s-5.55)}{s^2(s+30.55)(s+7.85)(s+5.54)} & \frac{-2.03(s+19.84)(s+7.09)(s-5.58)}{s^2(s+30.55)(s+7.85)(s+5.54)} & \frac{-8.69(s-4.54)(s+7.35)(s+17.33)}{s^2(s+30.55)(s+7.85)(s+5.54)} \\ \frac{16.68(s+29.4)(s+5.77)}{s(s+30.55)(s+7.85)(s+5.54)} & \frac{-2.89(s+32.1)(s+8.70)}{s(s+30.55)(s+7.85)(s+5.54)} & \frac{-12.62(s+32.31)(s+8.24)}{s(s+30.55)(s+7.85)(s+5.54)} \\ \frac{-5.21(s+44.15)(s+5.41)}{s(s+30.55)(s+7.85)(s+5.54)} & \frac{-1.33(s+42.17)(s+7.06)}{s(s+30.55)(s+7.85)(s+5.54)} & \frac{-2.98(s+57.32)(s+7.35)}{s(s+30.55)(s+7.85)(s+5.54)} \end{bmatrix} \quad (\text{B-2})$$

The transfer function matrix of the actuator model \mathbf{G}_{sm} in Eq. (4-4) is given by:

$$\mathbf{G}(s) = \begin{bmatrix} \frac{20}{s+20} & 0 & 0 \\ 0 & \frac{20}{s+20} & 0 \\ 0 & 0 & \frac{20}{s+20} \end{bmatrix} \quad (\text{B-3})$$

The weighting transfer function matrix $\mathbf{W}_{I,G}(s)$ in Eq. (4-25) is given by:

$$\mathbf{W}_{I,G}(s) = \begin{bmatrix} \frac{0.30(s+20.13)(s^2+16.67s+488.9)}{(s+48.65)(s^2+2.578s+176.7)} & \frac{0.28(s+64.53)(s^2+8.65s+47.29)}{(s+70.8)(s^2+8.52s+28.75)} & \frac{0.28(s+34.39)(s^2+6.06s+13.97)}{(s+42.36)(s^2+4.74s+8.32)} \\ \frac{27.29(s+44.47)(s+19.16)(s+3.02)}{(s+1105)(s+26.97)(s+2.12)} & \frac{0.29(s+4.35)(s^2+2.71s+17.24)}{(s+7.88)(s^2+3.03s+18.21)} & \frac{0.46(s+4.85)(s^2+2.67s+12.85)}{(s+10.93)(s^2+3.51s+13.88)} \\ \frac{0.33(s+29.58)(s^2+3.25s+16.34)}{(s+38.85)(s^2+3.82s+16.09)} & \frac{0.43(s+48.73)(s^2+8.12s+48.74)}{(s+59.42)(s^2+9.94s+42.32)} & \frac{0.68(s+27.95)(s^2+4.23s+19.41)}{(s+57.55)(s^2+5.22s+23.32)} \end{bmatrix} \quad (\text{B-4})$$

The weighting transfer function matrix $\mathbf{W}_{I,G_d}(s)$ in Eq. (4-26) is given by:

$$\mathbf{W}_{I,G_d}(s) = \begin{bmatrix} \frac{0.20(s+12.4)(s^2+23.14s+591.2)}{(s+39.76)(s^2+3.94s+144.1)} & \frac{0.18(s+23.4)(s^2+22.56s+541.8)}{(s+44.63)(s^2+2.64s+180)} & \frac{0.18(s+4.74)(s^2+15.03s+397.8)}{(s+2.39)(s^2+14.93s+334.1)} \\ \frac{1.75(s+46.02)(s^2+13.26s+48.99)}{(s+2.78)(s^2+61.7s+1303)} & \frac{24.76(s+134.6)(s+40.46)(s+2.31)}{(s+706.7)(s+236.7)(s+1.49)} & \frac{0.28(s+4.6)(s^2+1.93s+5.97)}{(s+7.60)(s^2+2.59s+6.43)} \\ \frac{0.24(s+35.41)(s+3.55)(s+1.96)}{(s+44.77)(s+3.51)(s+1.71)} & \frac{0.21(s+56.35)(s^2+5.98s+19.19)}{(s+59.67)(s^2+5.65s+14.09)} & \frac{0.34(s+17.61)(s^2+11.66s+65.26)}{(s+28.15)(s^2+11.54s+40.51)} \\ \frac{0.17(s+3.17)(s^2+16.57s+354.5)}{(s+1.99)(s^2+16.63s+276.5)} & \frac{0.18(s+3.08)(s^2+17.08s+324.7)}{(s+1.99)(s^2+19.11s+269.1)} & \frac{0.18(s+1.65)(s^2+19.39s+301.3)}{(s+1.4)(s^2+22.68s+228.3)} \\ \frac{0.28(s+2.67)(s^2+1.30s+3.72)}{(s+6.29)(s^2+1.60s+3.85)} & \frac{0.28(s+2.28)(s^2+5.49s+12.17)}{(s+3.69)(s^2+6.60s+16.5)} & \frac{0.27(s+2.35)(s^2+2.88s+5.06)}{(s+4.64)(s^2+3.54s+6.73)} \\ \frac{0.36(s+40.92)(s^2+6.23s+30.97)}{(s+55.96)(s^2+6.98s+29.41)} & \frac{0.42(s+20.22)(s^2+5.49s+14.35)}{(s+37.81)(s^2+4.54s+9.50)} & \frac{0.55(s+25.5)(s^2+2.72s+5.35)}{(s+57.07)(s^2+2.62s+4.87)} \end{bmatrix} \quad (\text{B-5})$$

The weighting transfer function matrix $\mathbf{W}_{I,G_{sm}}(s)$ in Eq. (4-27) is given by:

$$\mathbf{W}_{I,G}(s) = \begin{bmatrix} \frac{0.33(s+8.650e-04)}{(s+26.62)} & 0 & 0 \\ 0 & \frac{0.33(s+8.650e-04)}{(s+26.62)} & 0 \\ 0 & 0 & \frac{0.33(s+8.650e-04)}{(s+26.62)} \end{bmatrix} \quad (\text{B-6})$$

Bibliography

- [1] J. Anderson, *Fundamentals of Aerodynamics (SI units)*. McGraw hill, 2011.
- [2] K. J. Åström and B. Wittenmark, *Computer-controlled systems: theory and design*. Courier Corporation, 2013.
- [3] K. Åström and R. Murray, *Feedback Systems: An Introduction for Scientists and Engineers, Second Edition*. Princeton University Press, 2021.
- [4] J. Bai and Y. Kim, “Control of the vertical motion of a hydrofoil vessel,” *Ships and Offshore Structures*, vol. 5, no. 3, pp. 189–198, 2010.
- [5] R. W. Beard and T. W. McLain, *Small unmanned aircraft*. Princeton university press, 2012.
- [6] R. Bencatel, S. Keerthivarman, I. Kolmanovsky, and A. R. Girard, “Full state feedback foiling control for america’s cup catamarans,” *IEEE Transactions on Control Systems Technology*, vol. 29, no. 1, pp. 1–17, 2021.
- [7] C. S. Chin and M. Lau, “Modeling and testing of hydrodynamic damping model for a complex-shaped remotely-operated vehicle for control,” *Journal of Marine Science and Application*, vol. 11, 06 2012.
- [8] M. Daskovsky, “The hydrofoil in surface proximity, theory and experiment,” *Ocean engineering*, vol. 27, no. 10, pp. 1129–1159, 2000.
- [9] J. de la Cruz, J. Almansa, J. Giron-Sierra, F. Velasco, S. Esteban, J. Díaz Martínez, and B. Andres-Toro, “Improving the comfort of a fast ferry,” *Control Systems, IEEE*, vol. 24, pp. 47 – 60, 05 2004.
- [10] R. Dorf and R. Bishop, *Modern Control Systems, 13th Edition*. Pearson Prentice Hall, 2017.
- [11] S. Esteban, J. Giron-Sierra, B. Andres-Toro, J. de la Cruz, and J. Riola, “Fast ships models for seakeeping improvement studies using flaps and t-foil,” *Mathematical and Computer Modelling*, vol. 41, pp. 1–24, 01 2005.

- [12] O. M. Faltinsen, *Hydrodynamics of High-Speed Marine Vehicles*. Cambridge University Press, 2006.
- [13] FlyingFish, “Technical documentation for hydrofoil education and research platform,” 2021, unpublished documentation.
- [14] T. I. Fossen, *Handbook of marine craft hydrodynamics and motion control*. John Wiley & Sons, 2011.
- [15] —, *Lecture Notes: TTK 4190 Guidance, Navigation and Control of Vehicles*. Norwegian University of Science and Technology, 2021.
- [16] B. Friedland, *Control system design: an introduction to state-space methods*. Courier Corporation, 2012.
- [17] D.-W. Gu, P. Petkov, and M. M. Konstantinov, *Robust control design with MATLAB®*. Springer Science & Business Media, 2013.
- [18] V. Hassani, S. A. Alterskjær, D. Fathi, O. Selvik, and L. O. Sæther, “Experimental results on motion regulation in high speed marine vessels,” in *22nd Mediterranean Conference on Control and Automation*. IEEE, 2014, pp. 487–492.
- [19] I. Hatzakis, “Motion control of high-speed hydrofoil vessels using state-space methods,” Ph.D. dissertation, Massachusetts Institute of Technology, 2004.
- [20] I. Hatzakis and P. Sclavounos, “Active motion control of high-speed hydrofoil vessels by state-space methods,” *Journal of Ship Research*, vol. 50, pp. 49–62, 03 2006.
- [21] L. H. Holthuijsen, *Waves in Oceanic and Coastal Waters*. Cambridge University Press, 2007.
- [22] K. Hu, Y. Ding, and H. Wang, “High-speed catamaran’s longitudinal motion attenuation with active hydrofoils,” *Polish Maritime Research*, vol. 25, pp. 56–61, 08 2018.
- [23] S. Hydromechanics, *Maritime and Transport Technology of TU Delft, Towing Tank No. 1*, TU Delft, 2022. [Online]. Available: <https://www.tudelft.nl/3me/over/afdelingen/maritime-and-transport-technology/research/ship-hydromechanics/facilities/towing-tank-no-1>
- [24] Kawasaki, *Passenger Hydrofoil with Fully-Submerged Foils: Kawasaki’s JETFOIL*, 2020. [Online]. Available: <https://answers.khi.co.jp/en/mobility/20200731e-02/>
- [25] J.-H. Kim and Y.-H. Kim, “Motion control of a cruise ship by using active stabilizing fins,” *Proceedings of the Institution of Mechanical Engineers, Part M: Journal of Engineering for the Maritime Environment*, vol. 225, no. 4, pp. 311–324, 2011.
- [26] S.-H. Kim and H. Yamato, “An experimental study of the longitudinal motion control of a fully submerged hydrofoil model in following seas,” *Ocean Engineering*, vol. 31, no. 5, pp. 523–537, 2004.
- [27] —, “On the design of a longitudinal motion control system of a fully-submerged hydrofoil craft based on the optimal preview servo system,” *Ocean Engineering*, vol. 31, pp. 1637–1653, 09 2004.

-
- [28] S. Y. Lee and K. P. Rhee, "Design of ship-motion regulators for foil catamarans in irregular sea waves," *IEEE Journal of Oceanic Engineering*, vol. 27, no. 3, pp. 738–752, 2002.
- [29] S. Liu, H. Niu, L. Zhang, and C. Xu, "Modified adaptive complementary sliding mode control for the longitudinal motion stabilization of the fully-submerged hydrofoil craft," *International Journal of Naval Architecture and Ocean Engineering*, vol. 11, no. 1, pp. 584–596, 2019.
- [30] S. Liu, C. Xu, and Y. Wang, "Disturbance rejection control for the course keeping of the fully-submerged hydrofoil craft," in *2016 35th Chinese Control Conference (CCC)*. IEEE, 2016, pp. 747–751.
- [31] S. Liu, C. Xu, and L. Zhang, "Hierarchical robust path following control of fully submerged hydrofoil vessels," *IEEE Access*, vol. 5, pp. 21 472–21 487, 2017.
- [32] A. Lloyd, *Seakeeping: Ship Behaviour in Rough Weather*. A.R.J.M. Lloyd, 1998.
- [33] MathWorks, *Matlab Documentation*, 2022. [Online]. Available: www.mathworks.com/help/
- [34] K. Matveev and R. Duncan, "Development of the tool for predicting hydrofoil system performance and simulating motion of hydrofoil-assisted boats," in *High Speed and High Performance Ship and Craft Symposium, Everett/WA: ASNE, USA*. Citeseer, 2005.
- [35] J. R. Meyer and J. R. Wilkings, "Hydrofoil development and applications," *High Performance Marine Vehicles Conference and Exhibit*, 1992.
- [36] J. Mulder and F. o. A. E. TU Delft, *Flight DynamicsI: Lecture Notes AE3202*. TU Delft, 2013.
- [37] NASA, *Wing Geometry Definitions*, 2021. [Online]. Available: <https://www.grc.nasa.gov/www/k-12/airplane/geom.html>
- [38] K. Ogata *et al.*, *Modern control engineering*. Prentice hall Upper Saddle River, NJ, 2010, vol. 5.
- [39] A. Packard, K. Poolla, and R. Horowitz, *Dynamic Systems and Feedback, Class Notes for ME 132*. Department of Mechanical Engineering, University of California, 2002.
- [40] E. B. Piene, "Disturbance rejection of a high speed hydrofoil craft using a frequency weighted h2-optimal controller," Master's thesis, NTNU, 2018.
- [41] Pixhawk4, *PX4 User Guide*, 2022. [Online]. Available: https://docs.px4.io/master/en/flight_controller/pixhawk4.html
- [42] J. Ren and Y. Yang, "Fuzzy gain scheduling attitude control for hydrofoil catamaran," *Proceedings of the 2004 American Control Conference*, vol. 2, pp. 1103–1108 vol.2, 2004.
- [43] C. Scherer, "Theory of robust control," *Delft University of Technology*, pp. 1–160, 2001.
- [44] S. Skogestad and I. Postlethwaite, *Multivariable feedback control: analysis and design*. John Wiley & Sons, Inc., 2006, vol. 2.

-
- [45] E. ToolBox, *Water - Density, Specific Weight and Thermal Expansion Coefficients.*, 2003. [Online]. Available: https://www.engineeringtoolbox.com/water-density-specific-weight-d_595.html
- [46] M. Verhaegen and V. Verdult, *Filtering and system identification: a least squares approach*. Cambridge university press, 2007.
- [47] K. L. Wadlin, C. L. Shuford Jr, and J. R. McGehee, "A theoretical and experimental investigation of the lift and drag characteristics of a hydrofoil at subcritical and supercritical speeds," National Advisory Committee for Aeronautics, Tech. Rep., 1952.
- [48] Y. Wang, L. Bai, and S. Liu, "Nonlinear control of hydrofoil catamaran course in three dof," in *2014 IEEE Conference and Expo Transportation Electrification Asia-Pacific (ITEC Asia-Pacific)*. IEEE, 2014, pp. 1–6.
- [49] L. Yun and A. Bliault, *High Performance Marine Vessels*. Springer, 2012.
- [50] K. Zhou and J. C. Doyle, *Essentials of robust control*. Prentice hall Upper Saddle River, NJ, 1998, vol. 104.
- [51] H. Zumbahlen, "Phase response in active filters," in *Volume 43, Number 3, 2009 A forum for the exchange of circuits, systems, and software for real-world signal processing*, 2016, p. 18.

Glossary

List of Acronyms

TU Delft	Delft University of Technology
HEARP	Hydrofoil Education and Research Platform
IMU	Inertial measurement unit
GPS	Global positioning system
ESC	electronic speed controller
ECL	Estimation and Control Library
EKF	Extended Kalman Filter
SISO	single-input single-output
MIMO	multi-input multi-output
PWM	pulse-width modulation
EOM	equations of motion
DOF	degrees of freedom
SNAME	Society of Naval Architects and Marine Engineers
ECI	Earth-centered inertial
ECEF	Earth-centered Earth-fixed
NED	North-East-Down
CAD	computer-aided design
ROV	remotely operated vehicle
CG	centre of gravity
CB	centre of buoyancy
CP	centre of pressure
PID	Proportional-Integral-Derivative
LQR	Linear Quadratic Regulator
RMS	root mean square

LTI	linear time-invariant
LHP	left-half plane
RHP	right-half plane
NS	Nominal Stability
NP	Nominal Performance
RS	Robust Stability
RP	Robust Performance
SVD	singular value decomposition
LFT	linear fractional transformation
VAF	variance accounted for